NAVAL POSTGRADUATE SCHOOL
Monterey, California

THESIS

**OPTIMIZATION OF LOW THRUST TRAJECTORIES
WITH TERMINAL AEROCAPTURE**

by

Scott B. Josselyn

June 2003

Thesis Advisor:	I. Michael Ross
Second Reader:	Steve Matousek

THIS PAGE INTENTIONALLY LEFT BLANK

REPORT DOCUMENTATION PAGE		*Form Approved OMB No. 0704-0188*

1. AGENCY USE ONLY *(Leave blank)*	2. REPORT DATE June 2003	3. REPORT TYPE AND DATES COVERED Engineer's Thesis

4. TITLE AND SUBTITLE: Optimization of Low Thrust Trajectories with Terminal Aerocapture	5. FUNDING NUMBERS
6. AUTHOR(S) Josselyn, Scott B.	

7. PERFORMING ORGANIZATION NAME(S) AND ADDRESS(ES) Naval Postgraduate School Monterey, CA 93943-5000	8. PERFORMING ORGANIZATION REPORT NUMBER

9. SPONSORING /MONITORING AGENCY NAME(S) AND ADDRESS(ES) National Aeronautics and Space Administration Jet Propulsion Laboratory 4800 Oak Grove Drive Pasadena, CA 91109-8099	10. SPONSORING/MONITORING AGENCY REPORT NUMBER

11. SUPPLEMENTARY NOTES The views expressed in this thesis are those of the author and do not reflect the official policy or position of the Department of Defense or the U.S. Government.

12a. DISTRIBUTION / AVAILABILITY STATEMENT Approved for public release; distribution is unlimited.	12b. DISTRIBUTION CODE

13. ABSTRACT *(maximum 200 words)*

This thesis explores using a direct pseudospectral method for the solution of optimal control problems with mixed dynamics. An easy to use MATLAB optimization package known as DIDO is used to obtain the solutions. The modeling of both low thrust interplanetary trajectories as well as aerocapture trajectories is detailed and the solutions for low thrust minimum time and minimum fuel trajectories are explored with particular emphasis on verification of the optimality of the obtained solution. Optimal aerocpature trajectories are solved for rotating atmospheres over a range of arrival V-infinities. Solutions are obtained using various performance indexes including minimum fuel, minimum heat load, and minimum total aerocapture mass. Finally, the problem formulation and solutions for the mixed dynamic problem of low thrust trajectories with a terminal aerocapture maneuver is addressed yielding new trajectories maximizing the total scientific mass at arrival.

14. SUBJECT TERMS Low Thrust, Aerocapture, Trajectory Design.	15. NUMBER OF PAGES 173
	16. PRICE CODE

17. SECURITY CLASSIFICATION OF REPORT Unclassified	18. SECURITY CLASSIFICATION OF THIS PAGE Unclassified	19. SECURITY CLASSIFICATION OF ABSTRACT Unclassified	20. LIMITATION OF ABSTRACT UL

i

THIS PAGE INTENTIONALLY LEFT BLANK

OPTIMIZATION OF LOW THRUST TRAJECTORIES WITH TERMINAL AEROCAPTURE

Scott B. Josselyn
Lieutenant, United States Navy
B.S., United States Naval Academy, 1994

Submitted in partial fulfillment of the
requirements for the degree of

AERONAUTICAL AND ASTRONAUTICAL ENGINEER

from the

**NAVAL POSTGRADUATE SCHOOL
June 2003**

Author: Scott B. Josselyn

Approved by: I. Michael Ross
                Thesis Advisor

                Steve Matousek
                Second Reader

                Max F. Platzer
                Chairman, Department of Aeronautics and Astronautics

THIS PAGE INTENTIONALLY LEFT BLANK

ABSTRACT

This thesis explores using a direct pseudospectral method for the solution of optimal control problems with mixed dynamics. An easy to use MATLAB optimization package known as DIDO is used to obtain the solutions. The modeling of both low thrust interplanetary trajectories as well as aerocapture trajectories is detailed and the solutions for low thrust minimum time and minimum fuel trajectories are explored with particular emphasis on verification of the optimality of the obtained solution. Optimal aerocpature trajectories are solved for rotating atmospheres over a range of arrival V-infinities. Solutions are obtained using various performance indexes including minimum fuel, minimum heat load, and minimum total aerocapture mass. Finally, the problem formulation and solutions for the mixed dynamic problem of low thrust trajectories with a terminal aerocapture maneuver is addressed yielding new trajectories maximizing the total scientific mass at arrival.

THIS PAGE INTENTIONALLY LEFT BLANK

TABLE OF CONTENTS

THIS PAGE INTENTIONALLY LEFT BLANK

LIST OF FIGURES

LIST OF TABLES

THIS PAGE INTENTIONALLY LEFT BLANK

ACKNOWLEDGMENTS

The author would like to thank the following for their contributions:

The Creator for providing the problem, my loving wife and best friend Donna for the encouragement and support, Maxwell for making it all worth while, Professor I. M. Ross for bestowing the tools and knowledge, Steve Matousek (JPL), Jon Sims (JPL), Greg Whiffen (JPL), Jeffrey Hall (JPL) and Gary Allen (NASA Ames) for their invaluable guidance and my colleagues Jon Strizzi, Rob Stevens, Jeff King and Jim Ross for their friendship and assistance.

THIS PAGE INTENTIONALLY LEFT BLANK

LIST OF SYMBOLS AND ACRONYMS

C_3 V-infinity squared

CMT   covector mapping theorem

DOF   degree of freedom

DS1   Deep Space One

NEP   nuclear-electric propulsion

NLP   nonlinear programming problem

PCF   planet centered fixed

PCI   planet centered inertial

REN   radial-east-north (coordinate system)

SEP   solar-electric propulsion

SOI   sphere of influence

TPS   thermal protection system

A_{array} solar array area in m^2

a_s external tangential acceleration

a_n external normal acceleration

a_w external bi-normal acceleration

C Chapman equation heating-rate parameter

cf centrifugal force term

co Coriolis force term

D aerodynamic drag

h altitude (r-r_{planet})

h_0 reference altitude

H   Hamiltonian

$H^{\dagger}$ augmented Hamiltonian

j junction index

J   cost function/performance index

k ratio of TPS mass to heat load

L aerodynamic lift

M   Chapman equation index associated with velocity

m vehicle mass

N   Chapman equation index associated with density

P_{avail} electrical power available to the engines

P_0 reference solar incident power (power incident at 1 AU) in W/m^2

q_d dynamic pressure

r radial position from central body

r_{au} vehicle distance from the sun (in AU)

r_n vehicle nose radius

T thrust magnitude

$V_{atm\text{-}in}$ inertial speed at atmospheric interface (inbound)

$V_{atm\text{-}out}$ inertial speed at atmospheric interface (inbound)

V_{apo} inertial speed at atmospheric interface (inbound)

$V_{\infty arrival}$ inertial V-infinity at arrival

v   vehicle speed

v_e exhaust velocity

v_r radial velocity component

v_t transverse velocity component

X	generic state vector
β	inverse of scale height
d	bank angle
ε	specific energy
$\varepsilon_{arrival}$	specific energy at arrival
$\varepsilon_{atm\text{-}in}$	specific energy at atmospheric interface (inbound)
$\varepsilon_{atm\text{-}out}$	specific energy at atmospheric interface (outbound)
ε_{apo}	specific energy at of transfer orbit
f	planet fixed latitude
γ	flight path angle as measures positive up from E-N plane
Γ	inertial flight path angle
$\Gamma_{atm\text{-}out}$	inertial flight path angle at atmospheric interface (outbound)
Γ_{apo}	inertial flight path angle at of transfer orbit
h	thrust direction angle
h$_{solar}$	power converting efficiency of the solar array
λ_x	Lagrange multiplier associated with state "x" (also referred to as costate)
m	gravitational constant of central body
μ_x	Lagrange multiplier associated with path or control constraint
q	transfer angle
q	planet fixed longitude
r$_0$	reference density
t	integrating variable (time)
w	angular velocity

y heading angle as measured counter-clockwise from easterly

I. INTRODUCTION

In recent years, two developing concepts have been considered by mission designers to reduce the required propellant mass for interplanetary missions, thus allowing for increased mass of scientific payloads. Low thrust propulsion allows for greatly improved fuel efficiency and has the potential to increase payload mass fractions as well as providing trajectories not possible with impulsive thrust. Aerocapture is the careful management of a hypersonic atmospheric pass prior to orbit insertion to remove excess arrival velocity of a spacecraft obviating the need for a large propulsive capture maneuver. While aerocapture greatly reduces the propellant mass required for orbit insertion, the large heat loads generated in the atmospheric portion of the trajectory require the addition of a possibly massive thermal protection system (TPS). Both low thrust and aerocapture trajectories are highly non-linear with no closed-form solutions for their optimal open-loop control histories. This thesis addresses the feasibility of simultaneously optimizing a low thrust interplanetary trajectory with a terminal aerocapture maneuver to maximize the final scientific payload mass. In addition, the characteristics of optimal low thrust and aerocapture trajectories are explored with particular emphasis on techniques for the verification of the optimality of the obtained solutions.

THIS PAGE INTENTIONALLY LEFT BLANK

II.   LOW THRUST MODELING

A.   COORDINATE SYSTEM

Polar coordinates were chosen for the low thrust portion of the trajectory design optimization.   With the exception of the planets Mercury and Pluto, the orbits of the remaining planets all lie within $3.4°$ inclination of the solar ecliptic.   For the purposes of this thesis, the small angle approximation has been used to assume that all planets' orbits lie in the solar ecliptic. Figure 1 depicts the coordinate system used for the low thrust portion.
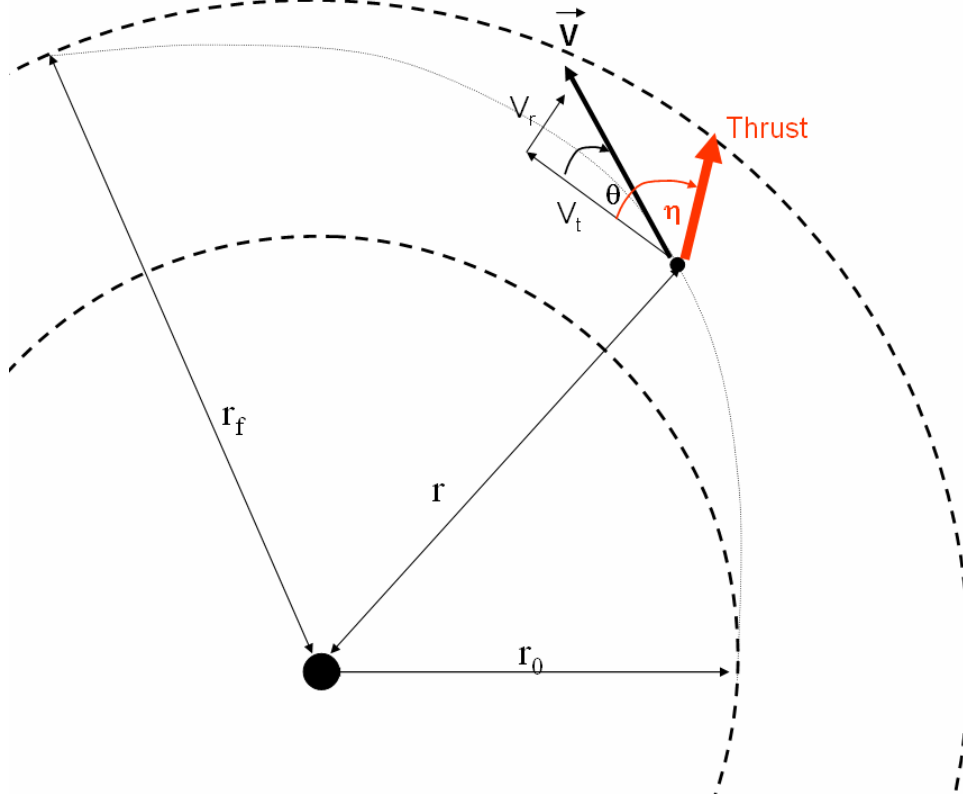
Figure 1: Low Thrust Coordinate System

B.   EQUATIONS OF MOTION

The state vector of a vehicle conducting a generic thrusting orbit transfer can be given as $\mathbf{x} = [r, \boldsymbol{q}, v_r, v_t, m]^{\mathbf{T}}$ where,

r ≡ radial position from central body

$\boldsymbol{q}$ ≡ transfer angle

v_r ≡ radial velocity component

v_t ≡ transverse velocity component

m ≡ vehicle mass

The equations of motion for a constant thrust orbit transfer are given in [Ref. 1] and can be modified for non-continuous thrust as follows:

$$\frac{dr}{dt} = v_r \tag{1}$$

$$\frac{d\boldsymbol{q}}{dt} = \frac{v_t}{r} \tag{2}$$

$$\frac{dv_r}{dt} = \frac{v_t^2}{r} - \frac{\boldsymbol{m}}{r^2} + \frac{T\sin\boldsymbol{h}}{m} \tag{3}$$

$$\frac{dv_t}{dt} = -\frac{v_r v_t}{r} + \frac{T\cos\boldsymbol{h}}{m} \tag{4}$$

$$\frac{dm}{dt} = -\frac{T}{v_e} \tag{5}$$

where

$\boldsymbol{m}$ ≡ gravitational constant of central body

T ≡ thrust magnitude

$\boldsymbol{h}$ ≡ thrust direction angle

v_e ≡ exhaust velocity

4

C.   GRAVITATIONAL MODEL

Only the gravitational effects of the central body are considered in this work. Higher fidelity models include the gravitational effects of other celestial bodies thus enabling the discovery of gravity assist trajectories. For the case of general planet-to-planet orbit transfer, the vehicle is far from other gravitational bodies for the bulk of the trajectory. By assuming that the trajectory begins and ends at the boundary of the sphere of influence (SOI) with an escape velocity greater than or equal to zero, the gravitational effects of the origin and target planet can be neglected completely.

For the inner, less massive planets, the SOI are reasonably small when compared to the orbit radii. Eqn. (6) [Ref. 2] approximates SOI radius as a function of the mean orbit radius and the ratio of masses between the gravitating bodies.

$$r_{SOI} \approx \left(\frac{m_{planet}}{m_{sun}} \right)^{2/5} r_{sun-planet} \tag{6}$$

Note that r_{SOI} approximately scales linearly with the distance to the sun. Despite the fact that the SOI radii of the other planets increase with distance from the sun, this increase is roughly proportional to the increase in trajectory length. Considering this, it is reasonable to assume that the origin and target planet can be thought of as non-gravitating point masses, reducing the problem to a two-body problem. Table 1 gives the approximate SOI radius for selected planets.

Planet	SOI Radius (km)	SOI Radius (AU)
Mercury	1.13×10^5	7.55×10^{-4}
Venus	6.17×10^5	4.12×10^{-3}
Earth	9.24×10^5	6.18×10^{-3}
Mars	5.74×10^5	3.84×10^{-3}
Jupiter	4.83×10^7	0.32
Neptune	8.67×10^7	0.58

Table 1: SOI Radius for Selected Planets (adapted from [Ref. 2])

D.   LAUNCH VEHICLE MODEL

A launch vehicle's performance is generally measured by the amount of mass it can place in a given orbit around the origin planet. For interplanetary trajectories, we are concerned with the trade-off between launch mass and the square of the escape velocity (know cryptically as C_3). [Ref. 2]. The launch performance may be fitted to a curve to be used to estimate launch mass from C_3 and vice versa. For this work, all trajectories will begin at the zero C_3 point (i.e. maximum launch mass with escape energy, equivalent to a parabolic escape).

E.   PROPULSION MODEL

The low thrust propulsion system used for this research is modeled after the NASA Solar electric propulsion Technology Applications Readiness project (NSTAR). This engine, employed in the *Deep Space I (DS1)* mission [Ref. 4], uses a single xenon ion propulsion system. This engine is 30 cm in diameter with a mass of approximately 8 kg. The engine delivers approximately 92 mN of thrust with a specific impulse of 3300 seconds. To achieve higher thrust levels, multiple engines can be used. The engine's specific impulse varies with the output thrust which is itself a function of the electrical power delivered to the engine. This model was simplified to assume a constant specific

impulse over the entire thrust range. Moreover, no limitations were placed on the available power provided to the engine. This assumption is valid provided a "near-limitless" source of power is available such as Nuclear-Electric Propulsion (NEP).

The propulsion model can be modified to account for "limited" power sources such as Solar-Electric Propulsion (SEP) by constraining the power available to the engine using

$$P_{avail} = \frac{h_{solar} P_0 A_{array}}{r_{au}^2} \tag{7}$$

where

P_{avail} ≡ electrical power available to the engines

P_0 ≡ reference solar incident power (power incident at 1 AU) in W/m^2

A_{array} ≡ solar array area in m^2

h_{solar} ≡ power converting efficiency of the solar array

r_{au} ≡ vehicle distance from the sun (in AU)

The power available can then be used to constrain the maximum thrust available at a given distance from the sun.

F.   NON-DIMENSIONALIZATION

Non-dimensionalization (or scaling) is the reformulation of the problem such that all the optimizable parameters as well as the cost function assume values close to unity over most of the domain of interest. When not scaled properly, the problem may become "ill-conditioned" and the effects of numerical artifacts as common as round-off error can begin to impact the solution. Very poorly scaled problems may even behave as though there are singularities when in fact there are none. Problems that have not been scaled are susceptible to various ailments ranging from slow convergence to complete failure to converge. Betts [Ref. 5] gives many tips for the scaling of problems and points out that even when a problem is well scaled at one point, it may be scaled poorly at another point.

A simple non-dimensionalization method is to simply divide a state variable x by a representative reference value for that variable [Ref. 6]. The low thrust problem may be normalized in this way using a modified version of the approach implemented by Bryson [Ref. 1]. Let a distance unit be defined as 1 AU and let a velocity unit be defined as the circular velocity of the earth. Thus we have

$$U_{dist} = R_{\oplus} \tag{8}$$

$$U_{vel} = \sqrt{\frac{m_{\odot}}{R_{\oplus}}} \tag{9}$$

where

$U_{dist} \equiv$ distance unit (1 AU)

$U_{vel} \equiv$ velocity unit (circular velocity at 1 AU)

Using this convention, a given radius r_x could be non-dimensionalized as follows

$$\bar{r}_x = \frac{r_x}{U_{dist}} \tag{10}$$

where an over-bar has been used to denote a non-dimensional variable. Continuing, the natural unit of time is simply

$$U_{time} = \frac{U_{dist}}{U_{vel}} \tag{11}$$

where

$U_{time} \equiv$ time unit

Note that for the above choice of distance and velocity units there are 2π time units per orbit. Now choosing the initial vehicle mass as our mass unit we have

$$U_{mass} = m_0 \tag{12}$$

where

$U_m \equiv$ mass unit

which completes the set of fundamental units. These particular choices of units are known collectively as canonical units. [Ref. 7] One advantage of using canonical units for astrodynamic problems is that the gravitational parameter **m** becomes one, simplifying many equations. A second advantage is that if only the above units (or combinations of the above units) are used to dimensionalize all the states, then the equations of motion take on exactly the same form as their dimensional counterparts provided there are no constant factors in any term which must be corrected (as is the case with the gravitational parameter which fortuitously is "corrected" to one). While it is true that the combinations of the above relations can be used to non-dimensionalize any parameter, there is no guarantee that the result will also be well scaled. In fact, the low thrust problem illustrates this fact nicely for particularly low thrusts.

Consider a 600 kg vehicle with one NSTAR engine producing 92 mN of thrust. Using the units above, it would seem reasonable to assume that

$$U_{thrust} = \frac{U_{mass} U_{dist}}{U_{time}^2} \tag{13}$$

Substituting the values of the canonical we get

$$U_{thrust} = \frac{(600 kg)(1.496 \times 10^{11} m)}{(5.023 \times 10^6)^2} = 3.9 N \tag{14}$$

Thus for this to be a useful unit for non-dimensionalizing thrust, we require our vehicle's thrust output to be on the order of 4 N. For realistic low thrust systems, this value of thrust unit may be too high. A better choice would be to define a thrust unit as the maximum thrust produced by the engine. This guarantees that the normalized thrust magnitude will fall between zero and one but requires the equations of motion to be modified slightly as follows:

$$\frac{d\bar{r}}{d\bar{t}} = \bar{v}_r \tag{15}$$

$$\frac{d\bar{q}}{d\bar{t}} = \frac{\bar{v}_t}{\bar{r}} \tag{16}$$

9

$$\frac{d\overline{v}_r}{d\overline{t}} = \frac{\overline{v}_t^{\,2}}{\overline{r}} - \frac{1}{\overline{r}^{\,2}} + \frac{z\overline{T}\sin\overline{h}}{\overline{m}} \tag{17}$$

$$\frac{d\overline{v}_t}{d\overline{t}} = -\frac{\overline{v}_r\overline{v}_t}{\overline{r}} + \frac{z\overline{T}\cos\overline{h}}{\overline{m}} \tag{18}$$

$$\frac{d\overline{m}}{d\overline{t}} = -\frac{z\overline{T}}{\overline{v}_e} \tag{19}$$

where

$$z = \frac{U_{thrust}U_{time}}{U_{dist}U_{vel}} \tag{20}$$

Clearly multiplying all the non-dimensional thrust terms in the equations of motion by this factor effectively accomplishes the same objective as normalizing thrust with purely canonical units. However, the difference is that domain of the thrust control is now well-scaled, and the conversions are taking place internal to the equations where proper scaling is not as important.

III.   AEROCAPTURE MODELING

A.   COORDINATE SYSTEMS

The coordinate systems chosen for aerocapture are the same as those used in existing developed tools such as ACAPS [Refs. 8,9] such that data could more easily be shared between programs.

1.   Position Vector

The vehicle's position vector is defined in the planet centered fixed (PCF) reference frame. This coordinate system is similar to a planet centered inertial (PCI) coordinate system except that the primary axis is aligned and rotates with a meridian line on the planet's surface [Ref 7]. The angular velocity of the PCF frame with respect to the PCI frame is denoted by Ω. As shown in Figure 2, the position vector is defined as $\mathbf{r} = [r, \mathbf{q}, \mathbf{f}]^{\mathbf{T}}$ where

r $\quad\equiv$ distance between origin and vehicle center of mass

$\mathbf{q}$ $\quad\equiv$ longitude as measured positive in an easterly direction

$\mathbf{f}$ $\quad\equiv$ latitude measured positive up from the equator
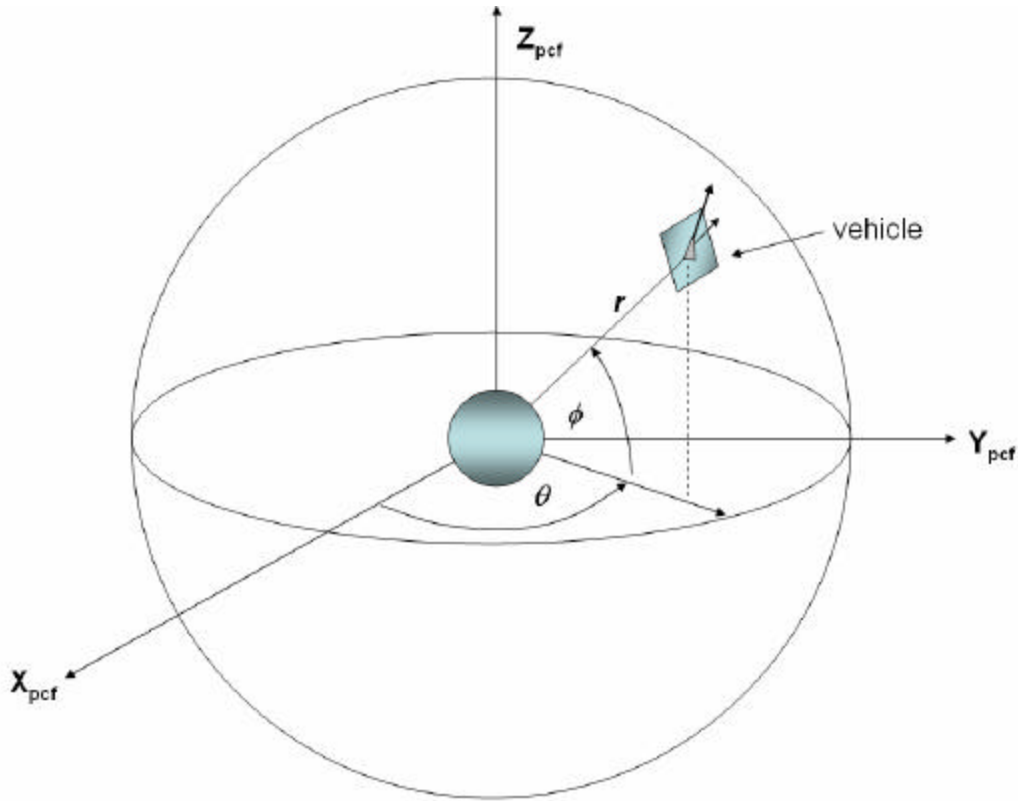
Figure 2: Aerocapture Position Coordinate System

Because the targeting of orbits with specific right ascensions is beyond the scope of this thesis and the equations of motion are invariant in longitude, it is convenient to define the longitude at atmospheric entry to be zero.

2. Velocity Vector

The velocity vector is measured in polar coordinates <u>relative</u> to the REN (Radius-East-North) frame. As shown in Figure 3, the REN frame is centered on the vehicle with the primary axis aligned with the extended radius vector. The tertiary axis is orthogonal and aligned toward the northern pole of the spherical coordinate system and the intermediate axis is mutually orthogonal and oriented easterly, completing the right-handed triad.
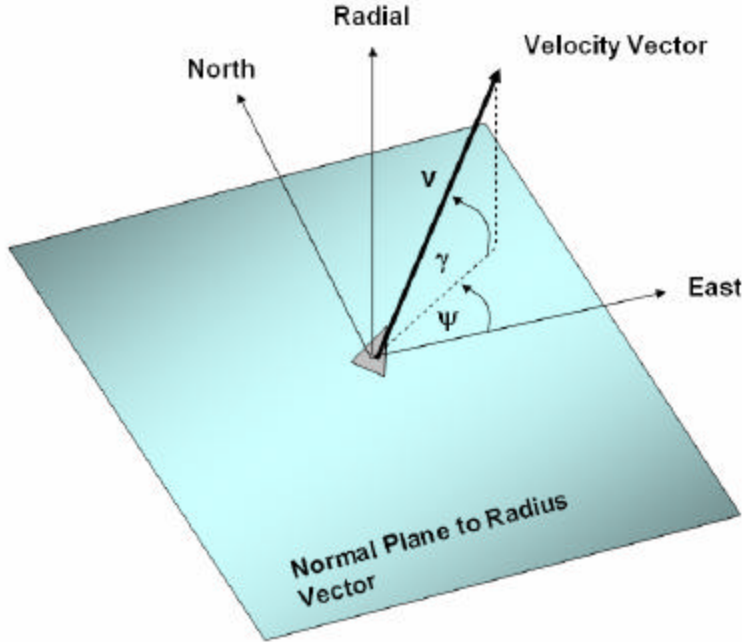
Figure 3: Aerocapture Velocity Coordinate System (REN Frame)

Within this frame, the velocity vector is represented by a magnitude and two angles, $\mathbf{V}_{PCF} = [v, \mathbf{y}, \mathbf{g}]^{\mathrm{T}}$ where

v $\qquad \equiv$ vehicle speed

$\mathbf{y}$ $\qquad \equiv$ heading angle as measured counter-clockwise from easterly

γ $\qquad \equiv$ flight path angle as measures positive up from E-N plane

It is important to note that the velocity vector represented in this frame is non-inertial unless $\Omega = 0$ in which case PCF = PCI. For reasons that will become apparent later, it is sometimes convenient to express the vehicle's <u>inertial</u> velocity in the local REN frame. This will be denoted by $\mathbf{V}_{PCI} = [V, \Psi, \Gamma]^{\mathrm{T}}$ where capital Greek letters have replaced their corresponding lower-cased non-inertial symbols.

3.   Frenet Frame

The Frenet frame (sometimes referred to as the NTW frame [Ref 7]) is useful for resolving vectors into tangent, normal and bi-normal components with respect to the vehicle's path. At a given time, the tangent component is tangent to the vehicle trajectory (alternately parallel to the velocity vector). The normal component lies in the plane of the orbit but perpendicular to the tangent component and the bi-normal component is normal to the orbit completing the right-hand triad. These components are identified by the subscripts **s, n,** and **w** respectively. The Frenet frame is a natural choice for resolving aerodynamic forces on a body as drag always acts in the negative direction tangent to the flight path and the lift vector will always lie in the normal/bi-normal plane. [Ref 7] That is to say that for a rotating atmosphere (fixed to the PCF frame) the Frenet axes are equivalent to wind axes.

B.   EQUATIONS OF MOTION

For the generation of optimal trajectories, a three degree of freedom (DOF) model is sufficient to describe the spacecraft dynamics. The state of the vehicle is represented by the 7-dimensional vector $\mathbf{x} = [r, \boldsymbol{q}, \boldsymbol{f}, v, \boldsymbol{y}, \boldsymbol{g}]^{\mathrm{T}}$ consisting of radial position, longitude, latitude, speed, heading angle, and flight path angle. The equations of motion for a non-rotating atmosphere with a generic gravity model are given by [Ref. 10] as

$$\frac{dr}{dt} = v \sin \boldsymbol{g} \tag{21}$$

$$\frac{d\boldsymbol{q}}{dt} = \frac{v \cos \boldsymbol{g} \cos \boldsymbol{y}}{r \cos \boldsymbol{f}} \tag{22}$$

$$\frac{d\boldsymbol{f}}{dt} = \frac{v \cos \boldsymbol{g} \sin \boldsymbol{y}}{r} \tag{23}$$

$$\frac{dv}{dt} = a_s + g_s \tag{24}$$

$$\frac{d\boldsymbol{y}}{dt} = \frac{a_w + g_w}{v \cos \boldsymbol{g}} - \frac{v}{r} \cos \boldsymbol{g} \cos \boldsymbol{y} \tan \boldsymbol{f} \tag{25}$$

14

$$\frac{d\boldsymbol{g}}{dt} = \frac{a_n + g_n}{v} + \frac{v\cos\boldsymbol{g}}{r} \tag{26}$$

where in the above equations a_s, a_n, and a_w are the external accelerations resolved in the Frenet frame.

1. Rotational Effects

For the higher-fidelity case of a rotating atmosphere, Eqs.(9) through (11) must be modified to account for non-inertial centrifugal and Coriolis forces.

$$\frac{dv}{dt} = a_s + g_s + cf_v \tag{27}$$

$$\frac{d\boldsymbol{y}}{dt} = \frac{a_w + g_w}{v\cos\boldsymbol{g}} - \frac{v}{r}\cos\boldsymbol{g}\cos\boldsymbol{y}\tan\boldsymbol{f} + cf_y + co_y \tag{28}$$

$$\frac{d\boldsymbol{g}}{dt} = \frac{a_n + g_n}{v} + \frac{v\cos\boldsymbol{g}}{r} + cf_g + co_g \tag{29}$$

where the *cf* and *co* terms represent centrifugal and Corilolis contributions respectively as given by

$$cf_v = \Omega^2 r\cos\boldsymbol{f}\left(\sin\boldsymbol{g}\cos\boldsymbol{f} - \cos\boldsymbol{g}\sin\boldsymbol{f}\sin\boldsymbol{y}\right) \tag{30}$$

$$cf_y = -\frac{\Omega^2 r}{v\cos\boldsymbol{g}}\sin\boldsymbol{f}\cos\boldsymbol{f}\cos\boldsymbol{y} \tag{31}$$

$$co_y = 2\Omega\left(\tan\boldsymbol{g}\cos\boldsymbol{f}\sin\boldsymbol{y} - \sin\boldsymbol{f}\right) \tag{32}$$

$$cf_g = \frac{\Omega^2 r}{v}\cos\boldsymbol{f}\left(\cos\boldsymbol{g}\cos\boldsymbol{f} + \sin\boldsymbol{g}\sin\boldsymbol{f}\sin\boldsymbol{y}\right) \tag{33}$$

$$co_g = 2\Omega\cos\boldsymbol{f}\cos\boldsymbol{y} \tag{34}$$

and Ω is the planet's angular rotation rate about its pole.

15

2.   Aerodynamic Forces

The aerodynamic forces of lift and drag are given [Ref. 11] as

$$L = q_d S C_L (a) \tag{35}$$

$$D = q_d S C_D (a) \tag{36}$$

where C_L and C_D are the lift and drag coefficients and are in general a function of angle of attack (a) and S is a reference area associated with the aerodynamic coefficients. The angle of attack is defined as the angle between vehicle's body axis and the velocity vector as shown in Figure 4,
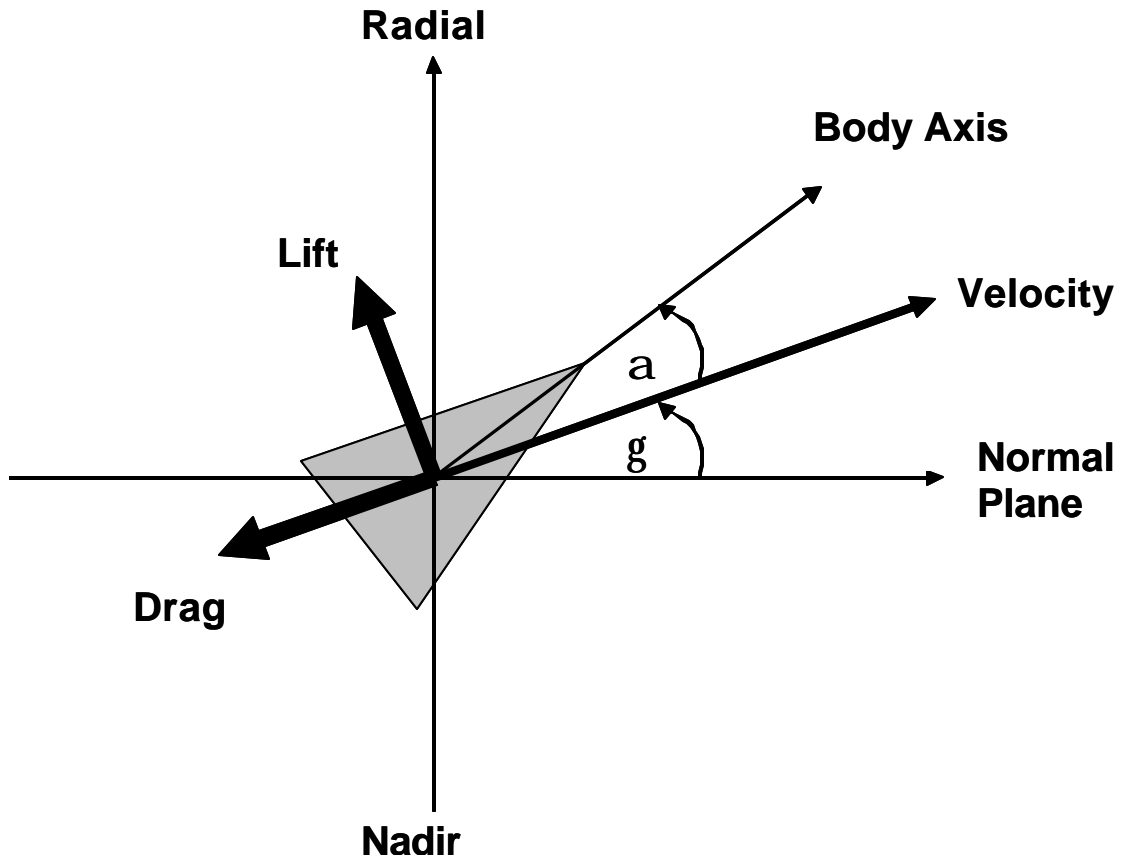
Figure 4: Definition of Angle of Attack and Flight Path Angle

The dynamic pressure, q_d is given by

16

$$q_d = \frac{1}{2} r(r) v^2 \qquad (37)$$

where r is the atmospheric density which is generally a function of altitude as given by the atmospheric model.

3. External Accelerations

The terms a_s, a_n, and a_w represent the external accelerations resolved in the tangential, normal and bi-normal directions. These accelerations are the result of the aerodynamic forces and vary with bank angle, δ which is defined as a body rotation about the vehicle's velocity vector as show in Figure 5.

Figure 5: Definition of Bank Angle

These accelerations can be expressed as function of the controls, mass and aerodynamic forces as

$$a_s = -\frac{D}{m} \tag{38}$$

$$a_n = \frac{L\cos \boldsymbol{d}}{m} \tag{39}$$

$$a_w = \frac{L\sin \boldsymbol{d}}{m} \tag{40}$$

Note that the total acceleration on the vehicle can be determined from these equations by using

$$\|a\| = \sqrt{a_s^{\,2} + a_n^{\,2} + a_w^{\,2}} \tag{41}$$

and the total g-load becomes

$$g-load = \frac{\|a\|}{g_0} \tag{42}$$

C.   GRAVITATIONAL MODEL

For a simple inverse-square gravity model, the gravitational accelerations can be converted from their more familiar spherical form

$$g = g_r = -\frac{\boldsymbol{m}}{r^2} \tag{43}$$

$$g_{\boldsymbol{q}} = 0 \tag{44}$$

$$g_{\boldsymbol{f}} = 0 \tag{45}$$

to the Frenet frame using Eqn. (215) becoming

$$g_n = -g\cos \boldsymbol{g} \tag{46}$$

$$g_s = -g\sin \boldsymbol{g} \tag{47}$$

$$g_w = 0 \tag{48}$$

18

Increased fidelity gravitational models, such as those including zonal harmonics can be incorporated in a similar manner [Ref. 9] but is beyond the scope of this work.

D.   ATMOSPHERIC MODEL

Anderson shows [Ref. 11] that if an atmosphere is assumed to be isothermal with constant temperature equal to the mean temperature, then atmospheric density varies exponentially with altitude. That is,

$$\boldsymbol{r}(r) = \boldsymbol{r}_0 e^{-\frac{(h-h_0)}{H_p}}$$
(49)

where

$\boldsymbol{r}_0$ ≡ reference density

H_p ≡ scale height

h ≡ altitude ($r\text{-}r_{planet}$)

h_0 ≡ reference altitude

The atmosphere is assumed to be fixed to the planet and rotates with the PCF coordinate system about the $\hat{K}_{PCF}$ axis. The following table provides the above data for Mars and Neptune.

Parameter	Mars Value	Neptune Value
$\boldsymbol{r}_0$	$4.7 \times 10^{-4} kg/m^3$	$2.348 \times 10^{-3} kg/m^3$
H_p	1.0×10^4 m	5.331×10^4 m
h_0	4.9×10^4 m	0 m
Atmosphere Limit	125 km	800 km

Table 1: Atmospheric Parameters for Mars and Neptune

E.   HEATING MODEL

The thermal protection system (TPS) for a re-entry vehicle is typically sized to sustain both the heating rate and heat load (integral of heating rate) encountered by the spacecraft [Refs. 12, 13] These quantities take a maximum value at the stagnation point, the point on the surface of the vehicle where the freestream velocity is brought locally to zero. The heating rate at this point can be approximated by the Chapman equation

$$\dot{q} = \frac{C}{\sqrt{r_n}} r^N v^M \qquad (50)$$

where

r_n $\equiv$ vehicle nose radius

C $\equiv$ stagnation point heating coefficient

and N and M are constants for a given atmosphere associated with density and speed respectively. [Ref. 14]

Parameter	Mars [Ref. 15]	Neptune [Ref. 17]
C	3.55×10^{-5}	7.9×10^{-5}
N	0.5	0.5
M	3.15	3.0

Table 2: Heating Rate Parameters for Mars and Neptune

F.   VEHICLE MODEL

The vehicle data used was obtained from [Ref. 9] for consistencies with that author's original work in aerocapture and is based loosely on the Mars Pathfinder shape. Due to the high cost to flight qualify new space flight components, most re-entry heat-shields have deviated very little since the early Viking designs. In light of this fact, the aerodynamic data below will likely be representative of possible future aerocapture vehicles. The aerodynamic coefficients listed below apply to Mars trajectories; lift and

drag coefficients at other planets should vary primarily due to variations in each planets' atmospheric composition. Unfortunately aerodynamic data for a Neptune aerocapture mission is not available; therefore the values for Mars will be used with the understanding that these coefficients do not agree with the vehicle design.

Following the atmospheric pass, the vehicle will require a small impulsive ΔV at apoapsis to place the vehicle in its final circular orbit. To accomplish this, a small conventional chemical engine using a bi-propellant comprised of Hydrazine (N_2H_4) fuel and Nitrogen Tetroxide (N_2O_4) as oxidizer is employed. This combination yields a specific impulse of approximately 330 seconds [Ref. 13] and provides sufficient thrust such that the ΔV may be considered impulsive.

Parameter	Symbol	Value
Vehicle Mass	m	568.5 kg
Nose Radius*	$\underline{r}_n$	1 m
Coefficient of Lift	C_L	0.3024
Coefficient of Drag	C_D	1.6800
Reference Area	S	5.52 m^2
Engine Specific Impulse	I_{sp}	330 sec
Engine Exhaust Velocity	V_e	3234 m/s

Table 3: Aerocapture Vehicle Parameters

G.   NON-DIMENSIONALIZATION

The aerocapture equations of motion have been non-dimensionalized in the same manner used by [Ref. 9] in his original work in aerocapture and are repeated here for completeness.

---

* Note: This value is not the actual measure of the nose radius; rather this value is chosen to be consistent with the stagnation point heating coefficient C in Table 3

$$\bar{r} = \frac{r}{U_{dist}} \tag{51}$$

where $U_{dist} \equiv r_{planet}$, the planet's surface radius.

$$\bar{v} = \frac{v}{U_{vel}} \tag{52}$$

where $U_{vel} \equiv \sqrt{\frac{m}{r_{planet}}}$, the circular velocity at the planet's surface.

$$\bar{t} = \frac{t}{U_{time}} \tag{53}$$

where $U_{time} \equiv \frac{U_{dist}}{U_{vel}}$ and

$$\bar{m} = \frac{m}{U_{mass}} \tag{54}$$

where $U_{mass} \equiv m_0$, the vehicle's initial mass. Noting that the angles measured in radians are already conveniently non-dimensional and well scaled, Eqns. (21)-(23) may be presented in their non-dimensional form

$$\frac{d\bar{r}}{d\bar{t}} = \bar{v} \sin \boldsymbol{g} \tag{55}$$

$$\frac{d\boldsymbol{q}}{d\bar{t}} = \frac{\bar{v} \cos \boldsymbol{g} \cos \boldsymbol{y}}{\bar{r} \cos \boldsymbol{f}} \tag{56}$$

$$\frac{d\boldsymbol{f}}{d\bar{t}} = \frac{\bar{v} \cos \boldsymbol{g} \sin \boldsymbol{y}}{\bar{r}} \tag{57}$$

The aerodynamic forces may be non-dimensionalize by first assuming that

$$\bar{\boldsymbol{r}} = \frac{\boldsymbol{r}}{U_{density}} \tag{58}$$

where $U_{density} \equiv \boldsymbol{r}_0$, the scale density and using a non-dimensional reference area defined as

$$\overline{S} = \frac{S}{\left(\dfrac{U_{mass}}{U_{density}U_{dist}}\right)} \tag{59}$$

Noting that the dynamic pressure non-dimensionalizes as

$$\overline{q}_d = \frac{1}{2}\boldsymbol{r}v^2 \tag{60}$$

the aerodynamic forces may be non-dimensionalized as

$$\overline{L} = \overline{q}_d\overline{S}C_L\left(\boldsymbol{a}\right) \tag{61}$$

$$\overline{D} = \overline{q}_d\overline{S}C_D\left(\boldsymbol{a}\right) \tag{62}$$

The external accelerations may now be written as

$$\overline{a}_s = -\frac{\overline{D}}{\overline{m}} \tag{63}$$

$$\overline{a}_n = \frac{\overline{L}\cos\boldsymbol{d}}{\overline{m}} \tag{64}$$

$$\overline{a}_w = \frac{\overline{L}\sin\boldsymbol{d}}{\overline{m}} \tag{65}$$

The gravitational acceleration becomes

$$\overline{g} = \overline{g}_r = \frac{-\dfrac{\boldsymbol{m}}{r^2}}{U_{grav}} \tag{66}$$

where $U_{grav} \equiv \dfrac{\boldsymbol{m}}{r_{planet}^2}$.

Eqns. (27)-(29) become

$$\frac{d\overline{v}}{d\overline{t}} = \overline{a}_s + \overline{g}_s + \overline{c}f_v \tag{67}$$

23

$$\frac{d\mathbf{y}}{d\bar{t}} = \frac{\bar{a}_w + \bar{g}_w}{\bar{v}\cos\mathbf{g}} - \frac{\bar{v}}{\bar{r}}\cos\mathbf{g}\cos\mathbf{y}\tan\mathbf{f} + \bar{cf}_y + \bar{co}_y \tag{68}$$

$$\frac{d\mathbf{g}}{d\bar{t}} = \frac{\bar{a}_n + \bar{g}_n}{\bar{v}} + \frac{\bar{v}\cos\mathbf{g}}{\bar{r}} + \bar{cf}_g + \bar{co}_g \tag{69}$$

where the centrifugal and Coriolis forces have been non-dimensionalized using

$$\bar{\Omega} = \Omega\, U_{time} \tag{70}$$

such that

$$\bar{cf}_v = \bar{\Omega}^2\bar{r}\cos\mathbf{f}\left(\sin\mathbf{g}\cos\mathbf{f} - \cos\mathbf{g}\sin\mathbf{f}\sin\mathbf{y}\right) \tag{71}$$

$$\bar{cf}_y = -\frac{\bar{\Omega}^2\bar{r}}{\bar{v}\cos\mathbf{g}}\sin\mathbf{f}\cos\mathbf{f}\cos\mathbf{y} \tag{72}$$

$$\bar{co}_y = 2\bar{\Omega}\left(\tan\mathbf{g}\cos\mathbf{f}\sin\mathbf{y} - \sin\mathbf{f}\right) \tag{73}$$

$$\bar{cf}_g = \frac{\bar{\Omega}^2\bar{r}}{\bar{v}}\cos\mathbf{f}\left(\cos\mathbf{g}\cos\mathbf{f} + \sin\mathbf{g}\sin\mathbf{f}\sin\mathbf{y}\right) \tag{74}$$

IV. SOLVING OPTIMAL CONTROL PROBLEMS

A. PRELIMINARIES

An optimal control problem is the task of solving for the state and control histories of a system subject to constraints while minimizing (or maximizing) some performance index. Put mathematically (as presented by [Ref. 18] and repeated here for completeness), given a system with dynamic constraints such that

$$\dot{\mathbf{x}}(t) = \mathbf{f}(\mathbf{x},\mathbf{u},t\,;\mathbf{p}) \tag{75}$$

where

$\mathbf{x}$ $\equiv$ vector of states that completely describe the systems at any τ

$\mathbf{u}$ $\equiv$ vector of controls

τ $\equiv$ independent variable (usually but not necessarily time)

$\mathbf{p}$ $\equiv$ vector of static parameters

$\mathbf{f}$ $\equiv$ vector of dynamic equations

subject to additional path constraints

$$\mathbf{g}_l \leq \mathbf{g}(\mathbf{x},\mathbf{u},t) \leq \mathbf{g}_u \tag{76}$$

$\mathbf{g}$ $\equiv$ vector path constraint equations

$\mathbf{g}_l$ $\equiv$ vector of lower path bounds

$\mathbf{g}_u$ $\equiv$ vector of upper path bounds

and boundary conditions (or point constraints)

$$\mathbf{e}_l \leq \mathbf{e}\left(\mathbf{x}(t_0),\mathbf{x}(t_f),t_0,t_f\right) \leq \mathbf{e}_u \tag{77}$$

$\mathbf{e}$ $\equiv$ vector path event condition equations

$\mathbf{e}_l$ $\equiv$ vector of lower event condition bounds

$\mathbf{e}_u$ $\equiv$ vector of upper event condition bounds

25

as well as bounds on states and controls

$$\mathbf{x}_l \leq \mathbf{x}(t) \leq \mathbf{x}_u \tag{78}$$

$$\mathbf{u}_l \leq \mathbf{u}(t) \leq \mathbf{u}_u \tag{79}$$

in order to minimize a performance index of form

$$J\left(\mathbf{x}(\cdot),\mathbf{u}(\cdot),t_0,t_f\right) = E\left(\mathbf{x}(t_0),\mathbf{x}(t_f),t_0,t_f\right) + \int_{t_0}^{t_f} F\left(\mathbf{x}(t),\mathbf{u}(t),t\right)dt \tag{80}$$

E $\quad\equiv$ scalar cost function evaluated at the boundary times (event cost)

F $\quad\equiv$ scalar cost function evaluated over the entire time history (integral cost)

When $F \in \varnothing$, the cost function is said to be in Mayer form. When $E \in \varnothing$, the cost function is said to be in Lagrange form. When $E, F \not\subset \varnothing$ the cost function is said to be in Bolza form.

A mathematical construct known as the Hamiltonian may be created by adjoining a vector of Lagrange multipliers to the dynamic constraints and adding the integral cost

$$H\left(\mathbf{x},\mathbf{u},l,t;\mathbf{p}\right) = F\left(\mathbf{x}(t),\mathbf{u}(t),t;\mathbf{p}\right) + l^{\mathrm{T}}\cdot\mathbf{f}\left(\mathbf{x}(t),\mathbf{u}(t),t;\mathbf{p}\right) \tag{81}$$

(Note: the Lagrange multipliers associated with the dynamics are also referred to as "costates"). The Pontryagin Minimum Principle (PMP) [Ref. 1] states that the optimal control history satisfies

$$\mathbf{u}^* = \operatorname{argmin} H \quad \text{subject to } \mathbf{u} \subset \mathbf{U} \tag{82}$$

where $\mathbf{u}^*$ is the optimal control and $\mathbf{U}$ is the domain of $\mathbf{u}$.

This should be recognized as a static optimization problem at each instant of time for which the Hamiltonian itself is now the performance index minimized. We can now form an additional construct known as the augmented Hamiltonian (or Lagrangian of the Hamiltonian) defined as

$$H^\dagger\left(\boldsymbol{\mu},l,\mathbf{x},\mathbf{u},t;\mathbf{p}\right) = H\left(\mathbf{x},\mathbf{u},l,t;\mathbf{p}\right) + \boldsymbol{\mu}^{\mathrm{T}}\cdot\mathbf{g}\left(\mathbf{x}(t),\mathbf{u}(t),t;\mathbf{p}\right) \tag{83}$$

The Karush-Kuhn-Tucker conditions state that when evaluated at the extremal controls, the following are true

$$\frac{\partial H^{\dagger}}{\partial \mathbf{u}} = 0 \tag{84}$$

$$\boldsymbol{\mu}^{\mathrm{T}}\mathbf{g} = 0 \tag{85}$$

$$\boldsymbol{m} \begin{cases} \leq 0 & g_l = g \\ \geq 0 & g = g_u \\ = 0 & if & g_l \leq g \leq g_u \\ any & g_l = g_u \end{cases} \tag{86}$$

where Eqns. (84) and (85) are referred to as the gradient normality and complementary conditions respectively. Eqn.(86) will be useful later for verifying the switching structure of the controls.

B.   SOLUTION METHODS

Methods for solving optimal control problems can generally be separated into two groups, indirect and direct methods [Ref. 5 p. 85].

Indirect methods tend to produce greater accuracy and faster solution times. However, the problem formulation for an indirect method is considerably more complex as the user must provide additional information such as the equations for the costate dynamics as well as the gradient of the Hamiltonian with respect to the controls. Moreover, one must provide a reasonably accurate guess for the controls, states and costates. Unfortunately, the abstract nature of the costates makes this guess-work something of an art.

By contrast, direct methods tend to be much more robust and can converge to an optimal solution even when seeded with a poor or infeasible guess. Direct methods require less prior work on the part of the user as the user need only supply the dynamic, path and event constraint functions as well as the cost function. Direct methods work on the premise that a continuous problem may be approximated through careful discretization as a large number of point constraints, thus reducing the problem to a

single large Nonlinear Programming problem (NLP). Unfortunately, to increase the accuracy of the solution, greater resolution is required leading to larger problems that can be very slow to converge.

C.   DISCRETIZATION

Approximation theory tells us that the worst (with regard to minimizing the L_2 error norm) discretization scheme is to sample a function at equal intervals [Ref. 6]. Other methods of discretization include Hermite-Simpson and Sinc methods [Ref. 20]. In fact, discretizing a function at the Legendre-Gauss-Labatto (LGL) points minimizes the L_2 error norm for a given number of nodes. LGL points are characteristic in that they have a higher density distribution at the end points of a function and becoming sparser in the interior regions.   By discretizing the problem in this manner, a direct solution may be obtained with either more accuracy or less computation time.

D.   DIDO

DIDO is an application package [Ref. 18] for solving dynamic optimization problems in a friendly, easy-to-use MATLAB environment. DIDO employs a powerful direct Legendre pseudospectral method that exploits the sparsity pattern of the discrete Jacobian by way of the NLP solver SNOPT" [Ref. 21] and runs in both UNIX and PC environments.

Problem formulation in DIDO is quite simple, with the user creating a set MATLAB functions to evaluate the problem dynamics, cost, path constraints and event conditions. These functions are tied together by an additional script which defines the upper and lower bounds for the states, controls, path constraints and event conditions as well as the initial guess. This guess need not be feasible; in most cases simply providing the estimated initial and final state value is sufficient. The simplicity of DIDO contributes to the rapid prototyping of solutions. An experienced DIDO user can generate optimal trajectories in days that previously would have required weeks or months.

The user defines the number of nodes (discretization points) for the problem and is afforded the option of "cold starting" or "bootstrapping" from a previous solution.

E.   COVECTOR MAPPING THEOREM

Another advantage of the Legendre pseudospectral method is that is provides accurate costate and covector histories despite the fact that the adjoint equation are not supplied. [Refs. 22, 23] This power comes from the realization of the Covector Mapping Theorem (CMT). [Ref. 21] provides the following explanation of the CMT:

> The CMT may be articulated as follows: Given an optimal control problem, P, let P^N denote its Legendre pseudospectral approximation where N is the order of the Legendre polynomial used in the approximation. Let P^1 denote the boundary value problem (BVP) arising from an application of the PMP to problem P, and P^{N1} denote the generalized root-finding problem obtained by applying the Karush-Kuhn-Tucker (KKT) conditions to problem P^N. The CMT asserts that if P^1 is discretized by a Legendre pseudospectral method (i.e. an indirect method), then there exists an order-preserving map between these discretized covectors and the KKT multipliers associated with problem P^{N1}. Hence, from the KKT multipliers, one can find covectors by the direct Legendre pseudospectral method as if one solved the problem by the indirect method. This is the CMT.

The power of the CMT is that it provides the user with excellent tools for ascertaining the optimality of a given solution as we will see in the next section. Additionally, because the CMT provides accurate costate information, a DIDO solution can be uses as an ext remely high quality guess for a more accurate indirect method.

F.   VERIFICATION OF OPTIMALITY

When solving optimal control problems one is often challenged as to how one can prove optimality. [Ref. 21] discusses techniques for verification of optimal trajectories.

1.   Feasibility

Of primal concern is the feasibility of a solution. That is, does the solution satisfy the dynamic constrains of the problem? To ascertain this, the initial conditions are propagated using a Runge-Kutta algorithm (the MATLAB command *ode45* which implements the Dormand-Prince pair) using controls interpolated from the DIDO solution. If the DIDO state history and the propagated state history match (within some tolerance) feasibility is declared.

2.   Accuracy

The next issue addresses the accuracy of the solution. Assuming the trajectory is feasible, the event conditions are evaluated using either the DIDO or propagated solution and examined to verify that all event constrains are satisfied (again, within a tolerance).

3.   Well-behaved

Similarly, the solution is said to be well behaved if the path constraints (including state and control bounds) are obeyed over the entire trajectory. A solution that violates the path constraints may indeed be feasible; however it does not solve the problem at hand.

4.   Optimality

Finally and most importantly, does the solution satisfy the necessary conditions for optimality? Recalling Eqn. (84), analytical expressions can be obtained by taking the partial of the augmented Hamiltonian with respect to each control. In some cases, these expressions can be rearranged into an explicit control law. Regardless, these expressions must hold true for there to be first-order optimality. These expressions can be verified through substitution of the states and CMT obtained costates and covectors. In the case where the necessary conditions can be re-arranged to solve for a control, these controls can be solved (referred to as CMT controls) and compared to DIDO solution controls. When the DIDO and CMT controls are in agreement, first-order optimality is declared.

A second method for determining optimality is by examination of the Hamiltonian which is also constructed by DIDO via the CMT. Recalling again Eqn.(84), the first integral of the necessary condition is required to be constant for Hamiltonians

that are not explicit functions of time. Thus the Hamiltonian can be plotted and its "flatness" used as a measure of optimality.

THIS PAGE INTENTIONALLY LEFT BLANK

V.   OPTIMAL LOW THRUST PROBLEM FORMULATION

A.   EVENT CONDITIONS

For the orbit transfer problem, the vehicle must begin at Earth's orbit distance

$$r(t_0) = r_{Earth} \tag{87}$$

and complete the trajectory at the target planet's orbital distance

$$r(t_f) = r_{target} \tag{88}$$

Assuming circular orbits with no ephemeris, there are an infinite number of equivalent solutions because the Hamiltonian is invariant with the vehicle's angular displacement. Thus it is convenient to tie down the initial angular displacement to some value.

$$q(t_0) = 0 \tag{89}$$

Assuming that the vehicle escapes Earth's SOI with zero C_3, the vehicle's initial velocity must match that of Earth. Again, assuming circular planet orbits, the equation for a body's radial and tangential velocities are

$$v_r(t_0) = 0 \tag{90}$$

$$v_t = \sqrt{\frac{m_{Sun}}{r_{Earth}}} \tag{91}$$

where $m_{Sun} = 1.327 \times 10^{20} \, m^3\!/s^2$ is the Sun's gravitational parameter. Moreover, initial vehicle mass must lie between the maximum capacity for the launch vehicle and some lower design bound.

For the rendezvous case the vehicle's final velocity vector must match that of the target planet thus

$$v_r(t_f) = 0 \tag{92}$$

$$v_t\left(t_f\right)=\sqrt{\frac{m_{Sun}}{r_{\text{target planet}}}} \tag{93}$$

For the case of a fly-by, the final velocity components would be left unconstrained.

B.   COST FUNCTIONS

1.   Minimum Time

To minimize time, the performance index can be constructed in either Mayer or Lagrange form. In Mayer form, the cost function is simply

$$J = t_f \tag{94}$$

Formulated as a Lagrange cost, the performance index becomes

$$J = \int_{t_0}^{t_f} dt \tag{95}$$

2.   Minimum Fuel

For a single-staged vehicle, minimizing fuel is equivalent to maximizing the final vehicle mass. Maximizing a quantity is the same as minimizing the negative of that quantity, thus the Mayer performance index for minimum fuel is simply

$$J = -m_f \tag{96}$$

where m_f is the final vehicle mass. Alternately this performance index may be formulated as a Lagrange cost by recalling that the fuel flow rate for a constant specific impulse propulsion system is given by

$$\dot{m}_{fuel} = \frac{T_{mag}}{v_e} \tag{97}$$

so the performance index can also be expressed as

$$J = \int_{t_0}^{t_f} \frac{T_{mag}}{v_e} \, dt \tag{98}$$

C.   CONTROLS

The natural choices of controls for the low thrust problem are thrust magnitude and thrust angle.   However, for some problems these choices lead to additional difficulties. Bounding the thrust angle as $0 \leq h \leq 2p$ can cause a jump discontinuity when the optimal control history passes through the boundary. Increasing the bounds to $-2p \leq h \leq 2p$ yields multiple values of η that are equivalent, again possibly contributing to numerical instability of the solver algorithm.

To remedy this problem the equations of motion were altered such that the controls are the radial and transverse thrust components as well as thrust magnitude.

Thrust Mag

sin h

cos h

h
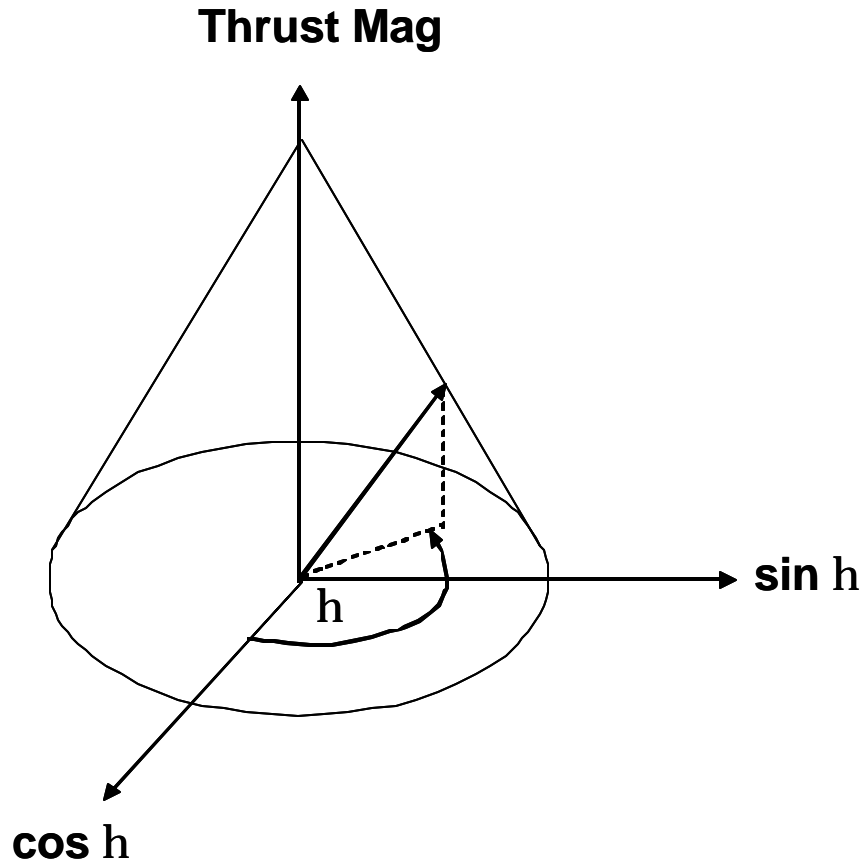
Figure 6: Thrust Cone

From Figure 6 clearly the thrust vector can be described by its radial and transverse components

$$T_r = T_{mag} \sin \boldsymbol{h} \tag{99}$$

$$T_t = T_{mag} \cos \boldsymbol{h} \tag{100}$$

and Eqns. (3),(4) and (5) can be rewritten with our new controls as

$$\frac{dv_r}{dt} = \frac{v_t^2}{r} - \frac{\boldsymbol{m}}{r^2} + \frac{T_r}{m} \tag{101}$$

$$\frac{dv_t}{dt} = -\frac{v_r v_t}{r} + \frac{T_t}{m} \tag{102}$$

36

$$\frac{dm}{dt} = -\frac{T_{mag}}{v_e} \tag{103}$$

Our control vector **u** is now

$$\mathbf{u} = \begin{bmatrix} T_r \\ T_t \\ T_{mag} \end{bmatrix} \tag{104}$$

where our controls are constrained within the following bounds

$$-T_{max} \leq T_r \leq T_{max} \tag{105}$$

$$-T_{max} \leq T_t \leq T_{max} \tag{106}$$

$$0 \leq T_{mag} \leq T_{max} \tag{107}$$

D.   STATE BOUNDS

Each state may be limited to a certain range of values over the trajectory, while others appear unbounded. As an example, the vehicle mass over the duration of the trajectory may not exceed its initial mass. Assuming that the vehicle's only method of shedding mass is via thrust, then the dry mass of the spacecraft serves as a lower bound. Thus over the entire problem, mass is restricted to

$$m_{dry} \leq m \leq m_{initial} \tag{108}$$

which might take a non-dimensional for of something like

$$.1 \leq \bar{m} \leq 1 \tag{109}$$

where the non-dimensional value for the lower bound depends on the vehicle's dry and initial masses.

Other states should be bound for more practical reasons. For example, a logical choice of bounds for heliocentric radius might be

$$0 \leq r \leq \infty \tag{110}$$

However, the dynamics [Eqns. (2)-(4)] become singular at $r = 0$, thus this is a bad choice for lower bound. Similarly, although there is no physical reason to have an upper bound, placing a *realistic* upper bound of, say, 100 reduces the search space for the NLP solver. Thus better state bounds might be

$$.1 \leq \bar{r} \leq 100 \tag{111}$$

where the bounds have been expressed in canonical units. For an orbit transfer to Mars (at only 1.52 AU) this upper bound could be reduced reasonably further.

Following similar reasoning, the remaining states take non-dimensional bounds of

$$-10 \leq v_r \leq 10 \tag{112}$$

$$-10 \leq v_t \leq 10 \tag{113}$$

$$0 \leq q \leq 10p \tag{114}$$

Thus the state bounds can be expressed in vector format as

$$\begin{bmatrix} .1 \\ 0 \\ -10 \\ -10 \\ .1 \end{bmatrix} \leq \begin{bmatrix} \bar{r} \\ \bar{q} \\ \bar{v}_r \\ \bar{v}_t \\ \bar{m} \end{bmatrix} \leq \begin{bmatrix} 100 \\ 10p \\ 10 \\ 10 \\ 1 \end{bmatrix} \tag{115}$$

E.   PATH CONSTRAINTS

As currently bound, the control space incorrectly takes the shape of a rectangular solid. An additional constraint is needed to relate the three controls and correct the control domain.

$$T_r^2 + T_t^2 - T_{mag}^2 = 0 \tag{116}$$

In the control space $\mathbf{u} \subset \mathfrak{R}^3$ this path constraint represents the surface of a cone. Because the interior of the cone is not in the domain of $\mathbf{u}$, the problem is not convex, thus leading to additional difficulties with attaining a rapidly converging solution. Interestingly, this problem can be convexified by restating the path constraint as

$$-T_{mag}{}^2 \le T_r^2 + T_t^2 - T_{mag}{}^2 \le 0 \qquad (117)$$

which represents a *solid* cone. Thus physics must be violated to convexify the problem. Fortunately, Pontryagin's Minimum principle [Ref. 19] ensures that the optimal control lies on the boundary of the constraint surface. In essence, physics is intentionally violated to improve the convergence of the solution with the guarantee that the Minimum Principle will restore continuity of physical reality.

F.   NECESSARY CONDITIONS

Recall from chapter IV that the Hamiltonian is defined

$$H(\mathbf{x},\mathbf{u},\boldsymbol{l},t;\mathbf{p}) = F(\mathbf{x}(t),\mathbf{u}(t),t;\mathbf{p}) + \boldsymbol{l}^{\mathrm{T}} \cdot \mathbf{f}(\mathbf{x}(t),\mathbf{u}(t),t;\mathbf{p}) \qquad (118)$$

Assuming any Mayer cost (that is $\mathbf{F} \in \varnothing$), the Hamiltonian can be constructed as

$$H = \boldsymbol{l}_r(v_r) + \boldsymbol{l}_q\left(\frac{v_t}{r}\right) + \boldsymbol{l}_{v_r}\left(\frac{v_t^2}{r} - \frac{\boldsymbol{m}}{r^2} + \frac{T_r}{m}\right) + \boldsymbol{l}_{v_t}\left(-\frac{v_r v_t}{r} + \frac{T_t}{m}\right) + \boldsymbol{l}_m\left(-\frac{T_{mag}}{v_e}\right) \qquad (119)$$

The augmented Hamiltonian $H^\dagger$ is found by adjoining the path constraints to the above Hamiltonian as follows

$$H^\dagger = \boldsymbol{l}_r(v_r) + \boldsymbol{l}_q\left(\frac{v_t}{r}\right) + \boldsymbol{l}_{v_r}\left(\frac{v_t^2}{r} - \frac{\boldsymbol{m}}{r^2} + \frac{T_r}{m}\right) + \boldsymbol{l}_{v_t}\left(-\frac{v_r v_t}{r} + \frac{T_t}{m}\right) + \boldsymbol{l}_m\left(-\frac{T_{mag}}{v_e}\right) + \dots$$
$$\boldsymbol{m}_{T_r}T_r + \boldsymbol{m}_{T_t}T_t + \boldsymbol{m}_{T_{mag}}T_{mag} + \boldsymbol{m}_{rel}\left(T_r^2 + T_t^2 - T_{mag}{}^2\right) \qquad (120)$$

where $\boldsymbol{m}_{T_r}$, $\boldsymbol{m}_{T_t}$, and $\boldsymbol{m}_{T_{mag}}$ are the Lagrange multiplies associated with the control bounds and $\boldsymbol{m}_{rel}$ is the Lagrange multiplier associated with path constraint relating the three controls [Eqn. (117)].

Applying the necessary condition for optimality by taking the partial derivative of the augmented Hamiltonian with respect to each control we obtain the following three necessary conditions:

$$\frac{\partial H^\dagger}{\partial T_r} = \frac{\boldsymbol{l}_{v_r}}{m} + \boldsymbol{m}_{T_r} + 2\boldsymbol{m}_{rel}T_r = 0 \qquad (121)$$

$$\frac{\partial H^{\dagger}}{\partial T_t} = \frac{\boldsymbol{l}_{v_r}}{m} + \boldsymbol{m}_{T_t} + 2\boldsymbol{m}_{rel}T_t = 0 \tag{122}$$

$$\frac{\partial H^{\dagger}}{\partial T_{mag}} = -\frac{\boldsymbol{l}_m}{v_e} + \boldsymbol{m}_{T_{mag}} - 2\boldsymbol{m}_{rel}T_{mag} = 0 \tag{123}$$

These can be re-arranged to explicitly solve for the controls

$$T_r = -\frac{1}{2\boldsymbol{m}_{rel}}\left(\frac{\boldsymbol{l}_{v_r}}{m} + \boldsymbol{m}_{T_r}\right) \tag{124}$$

$$T_t = -\frac{1}{2\boldsymbol{m}_{rel}}\left(\frac{\boldsymbol{l}_{v_t}}{m} + \boldsymbol{m}_{T_t}\right) \tag{125}$$

$$T_{mag} = \frac{1}{2\boldsymbol{m}_{rel}}\left(-\frac{\boldsymbol{l}_m}{v_e} + \boldsymbol{m}_{T_{mag}}\right) \tag{126}$$

The normalized equations of motion had an additional factor relating the thrust units to the other canonical units. Thus in non-dimensional form Eqns. (124)-(126) become

$$\overline{T}_r = -\frac{1}{2\boldsymbol{m}_{rel}}\left(\frac{z\boldsymbol{l}_{v_r}}{\overline{m}} + \boldsymbol{m}_{T_r}\right) \tag{127}$$

$$\overline{T}_t = -\frac{1}{2\boldsymbol{m}_{rel}}\left(\frac{z\boldsymbol{l}_{v_t}}{\overline{m}} + \boldsymbol{m}_{T_t}\right) \tag{128}$$

$$\overline{T}_{mag} = \frac{1}{2\boldsymbol{m}_{rel}}\left(-\frac{z\boldsymbol{l}_m}{\overline{v}_e} + \boldsymbol{m}_{T_{mag}}\right) \tag{129}$$

where

$$z = \frac{U_{thrust}U_{time}}{U_{dist}U_{vel}} \tag{130}$$

These expressions will prove useful for verification of the DIDO solutions in the next chapter.

40

VI.   OPTIMAL LOW THRUST RESULTS

A.   PROCESS

The code was first validated by solving the well-known minimum time low thrust transfer problem as presented in [Ref. 1]. With this success in hand, the parameters were modified to better represent actual technology. It was at this time that the problems with the original non-dimensionaliztion scheme for thrust became apparent. Although minimum time trajectories were acceptable, feasible minimum fuel trajectories were difficult to obtain.   The problem was reformulated using the improved non-dimensionalization scheme with better results.

In general, low thrust problems took considerably less computation time than their aerocapture counterparts due to the fewer number of state variables and "slower" dynamics. For this reason, solutions were generally not bootstrapped, but instead solved completely each time from an initial guess.

B.   MINIMUM TIME RENDEZVOUS

The minimum time, Mars rendezvous problem was solved for a vehicle powered by six NSTAR ion engines providing a total thrust capacity of 0.55 N. The initial vehicle mass was fixed at the maximum lift mass (C_3 of zero) for the Delta II 7326-9.5 which corresponds to 659.3 kg. If the initial mass is not fixed at some value, initial runs showed that the solution would always choose the smallest initial mass available with the minimum propellant mass necessary to complete the trajectory, essentially minimizing the inertia the thruster must work against. As discussed in Chapter V, a zero C_3 departure trajectory can be modeled as beginning at the origin planet's location, matching the planet's tangential velocity and with zero radial velocity. Sixty nodes were used to solve the problem, requiring only 4.91 minutes on a Pentium IV PC (1.8 Ghz, 512 Mb RAM). This large number of nodes was more than sufficient to capture the details of the trajectory but the increased number of nodes was used to generate more aesthetically pleasing plots. The minimum time for transfer is 182.57 days during which time the vehicle consumes 270.2 kg of propellant for an arrival mass of 389.2 kg. Figure 7 shows

the non-dimensional state histories versus time. The symbols represent the DIDO solutions while the line represents the propagated solution (using the DIDO controls).
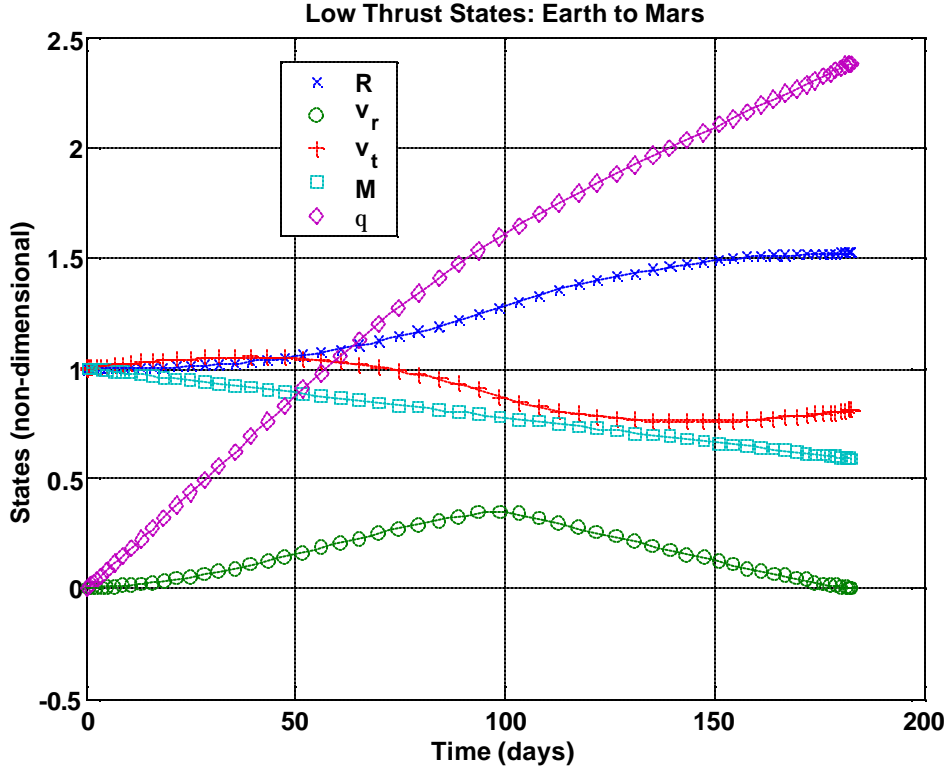
Figure 7: State History (Min Time to Mars Rendezvous)

The radius vector smoothly and asymptotically transitions from 1 AU to 1.52 AU while the transfer angle increases almost linearly to 136.6 deg. Radial velocity increases to a maximum of 0.35 canonical units before symmetrically returning to zero to effect the rendezvous. Transverse velocity first slightly increases before beginning to decay matching Mars' circular velocity of 0.81 canonical units. Mass of course decreases linearly due to the constant specific impulse and constant thrust profile as we shall see shortly.

The heliocentric transfer orbit is shown in Figure 8 with the viewpoint from the solar ecliptic plane north pole. Again, the circles are the DIDO trajectory and the solid line is the propagated trajectory. The arrows are oriented with the thrust direction and scaled to the magnitude of the thrust vector. There is a noticeable switch approximately

half the distance between Earth and Mars where the thrust vector swings through from being predominantly outward to being predominantly inward. It is this change in the radial component of the velocity vector that begins to arrest the vehicles radial velocity to prepare it for a zero relative velocity arrival.
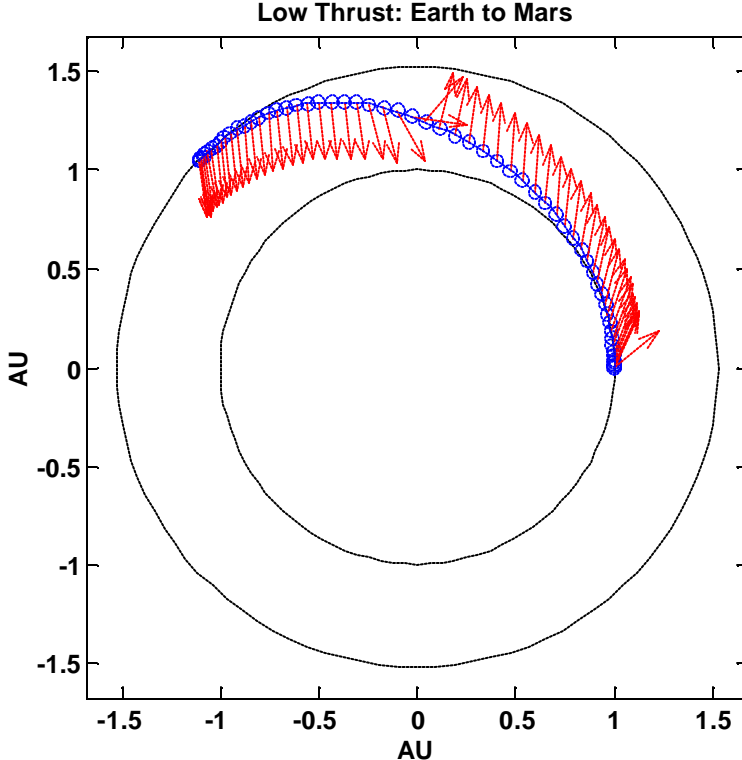
Figure 8: Heliocentric Trajectory (Min Time to Mars Rendezvous)

Figure 9 shows the control history during the trajectory. The DIDO controls are plotted as circles and the CMT derived controls are plotted as dots. The change in radial component of the velocity vector is readily apparent in the thrust angle control history just prior to the 100 day mark. As expected, the DIDO thrust magnitude for the minimum time trajectory employs maximum thrust for the entire trajectory. The DIDO controls and the CMT controls are in excellent agreement for the thrust anglealthough they do not coincide for the thrust magnitude. Despite the CMT controls telling us otherwise, the constant thrust solution is well known for the minimum time problem; thus it seems there may be an error in the way DIDO calculates costates and covectors or an artifact specific to this problem formulation. Figure 10 gives the Hamiltonian for the problem. Note that the variations in the Hamiltonian are on the order of 10^{-2}, that is, the

Hamiltonian is very nearly constant. This fact, combined with the excellent agreement between the thrust angle DIDO and CMT controls suggest that the first order necessary conditions for optimality have been met.
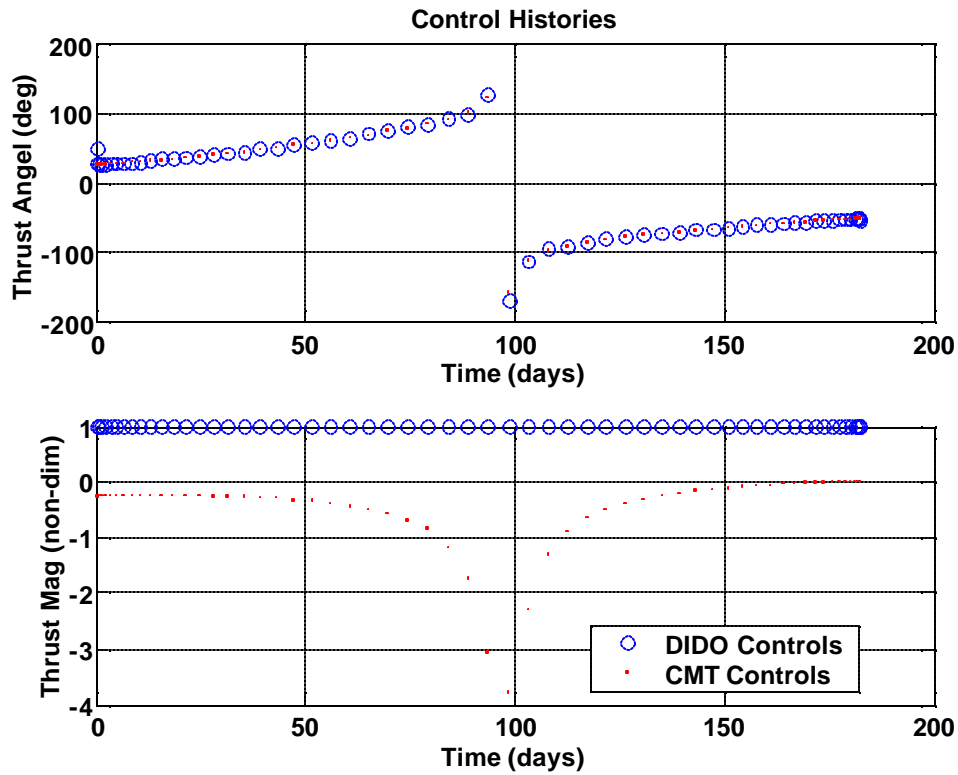
Figure 9: Control History (Min Time to Mars Rendezvous)
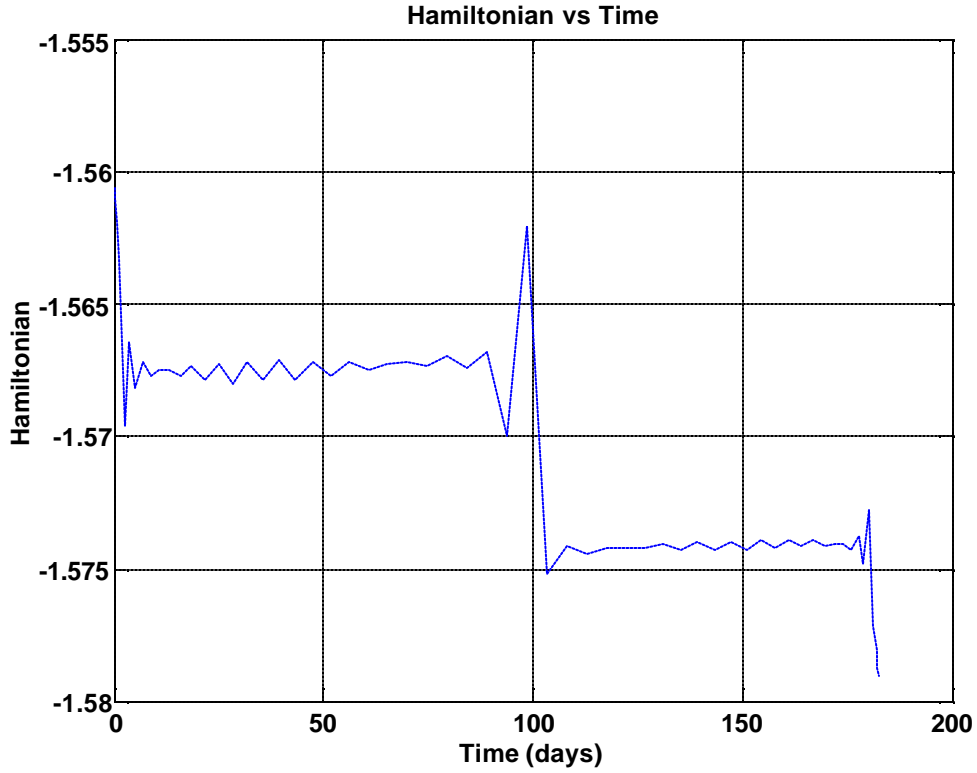
Figure 10: Hamiltonian (Min Time to Mars Rendezvous)

C. MINIMUM FUEL RENDEZVOUS

Next, the minimum fuel rendezvous was solved. The problem was set up identically to the minimum time problem with one notable exception, the initial mass event condition was free. As in the minimum time problem with initial mass free, the solution chose to depart Earth with the minimum amount of mass required to complete the journey. This is hardly in the spirit of planetary exploration, therefore the cost function was modified to instead maximize the final mass as in Eqn. (96). Thus in this case "minimum fuel" is a bit of a misnomer; instead, minimum fuel is implied by the true cost, maximized final mass.

A second difficulty with minimum fuel trajectories is that they tend to gravitate toward extremely long trajectories in both time and path length. If both time and transfer angle are unconstrained, the vehicle will begin the trajectory with a very short duration

45

burn which slightly raises the aphelion of the trajectory. The vehicle then coasts for slightly more than a year before returning to perihelion where it again conducts a short burn, again slightly raising aphelion. This pattern is repeated over many years until the aphelion has finally reached the target planet's orbital radius. These extremely long trajectories are difficult to capture using a direct method such as DIDO due to the comparatively few number of nodes typically used. To prevent this from occurring, the transfer angle was bound such that only type I orbits would be permissible (a type I orbit is an orbit with a total transfer angle between zero and 180 degrees, a type II orbit between 180 and 360 degrees, etc.) That is to say

$$0 \leq \boldsymbol{q}\left(t_f\right) \leq \boldsymbol{p} \tag{131}$$

The optimal solution presented below is comprised of 60 nodes and required 7.85 minutes to converge. The total flight time was 0.695694 years (253.4 days) or 70 days longer than the minimum time trajectory. However only 119.1 kg of propellant are used giving an arrival mass of 540.3 kg. Note also that the final transfer angle is exactly $\boldsymbol{p}$, the maximum allowable. Once again the propagated states (plotted as lines) are in excellent agreement with the DIDO states (plotted as various symbols). Thus the trajectory is at a minimum feasible.
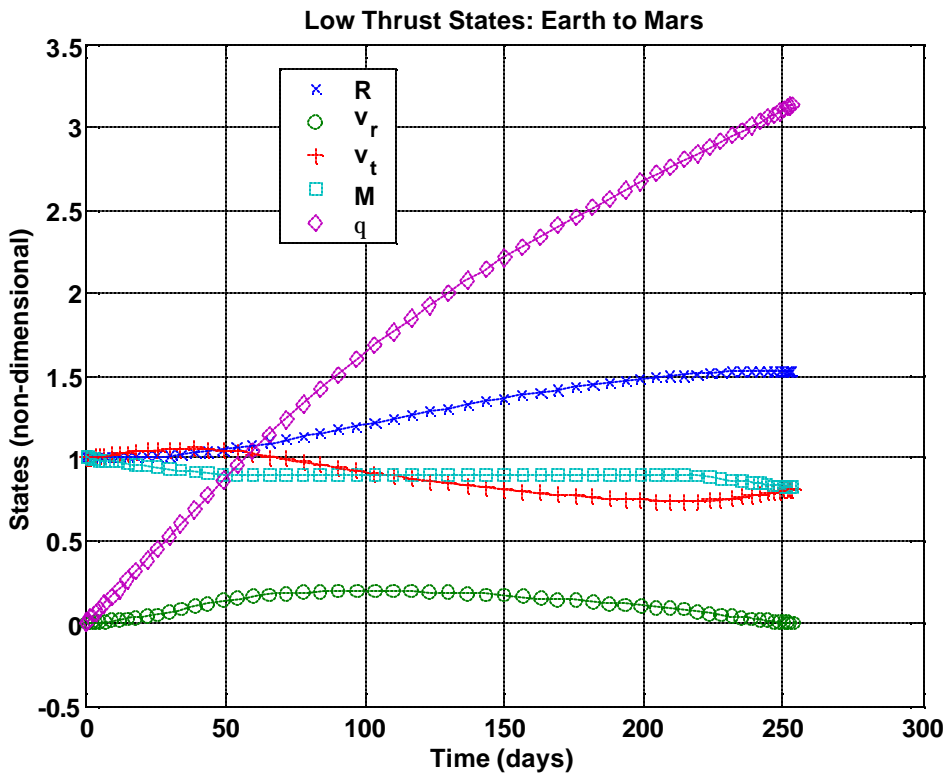
Figure 11: State History (Min Fuel to Mars Rendezvous)

The heliocentric view of the trajectory [Figure 12] shows how this mass savings is attained. The vehicle begins by applying a near-tangential burn for approximately 40 days before shutting off. This long burn places the vehicle in a transfer orbit whose aphelion exactly corresponds with Mars' orbit radius. The vehicle coasts along this trajectory until around the 220th day where it begins a shorter, sustained burn to increase the vehicle's speed to match that of Mars.
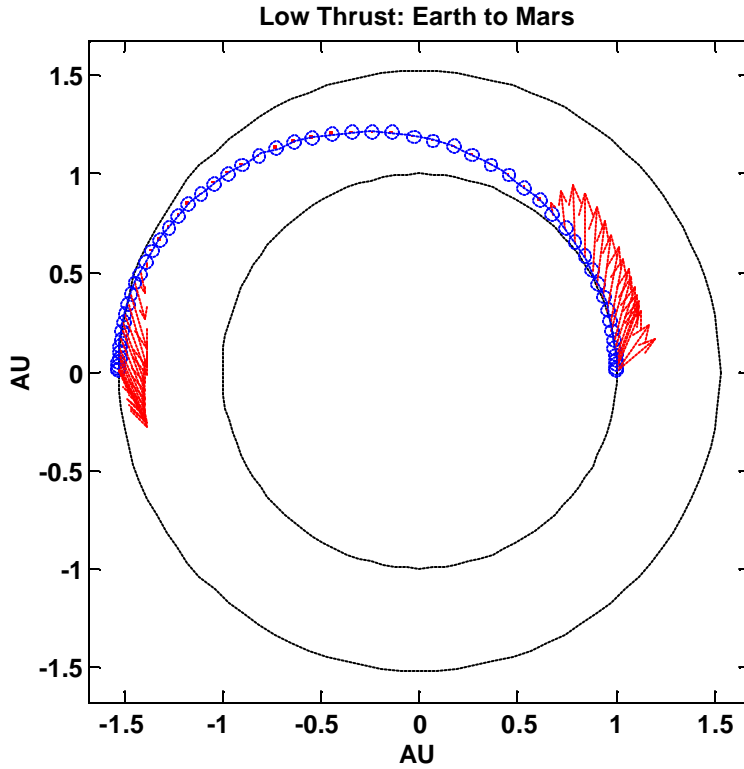
Figure 12: Heliocentric Trajectory (Min Fuel to Mars Rendezvous)

The next plot shows the control history throughout the trajectory. Again the CMT and DIDO controls match extremely well for the thrust angle but diverge for the thrust magnitude control. The DIDO thrust angle control (circles) can be seen to become more irregular in the middle portion of the trajectory when vehicle is not thrusting. This is expected as the thrust angle is not well defined without a thrust magnitude. Much more interestingly is the fact that the CMT thrust angle control history (dots) *does* appear to follow a well-defined, smooth curve even when the thrust magnitude is zero. Also note that although the thrust magnitude CMT and DIDO controls do not agree during the thrusting portion of the trajectory, they do agree during the non-thrusting portion. Thus it seems that the "switch" is only working in one direction.
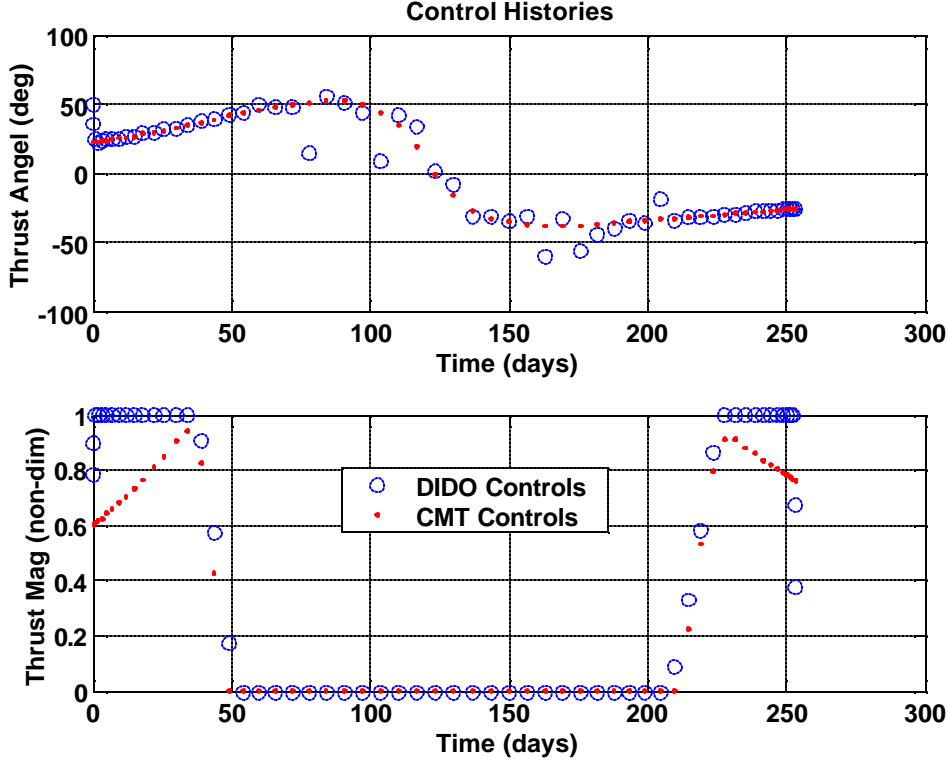
Figure 13: Control Histories (Min Fuel to Mars Rendezvous)

Let us investigate this discrepancy further. Recall that the necessary condition for the thrust magnitude is

$$T_{mag} = \frac{1}{2\boldsymbol{m}_{rel}}\left(-\frac{\boldsymbol{l}_m}{v_e} + \boldsymbol{m}_{T_{mag}}\right) \tag{132}$$

which can be rearranged as

$$\boldsymbol{m}_{T_{mag}} = 2T_{mag}\boldsymbol{m}_{rel} + \frac{\boldsymbol{l}_m}{v_e} \tag{133}$$

Because DIDO returns both the covectors with the solution (via the CMT) we can plug the DIDO solution states, controls and covectors into the right hand side of Eqn. (133) and check that the result matches the thrust magnitude covector as returned by DIDO. As we can see in the following plot, the two do not agree.
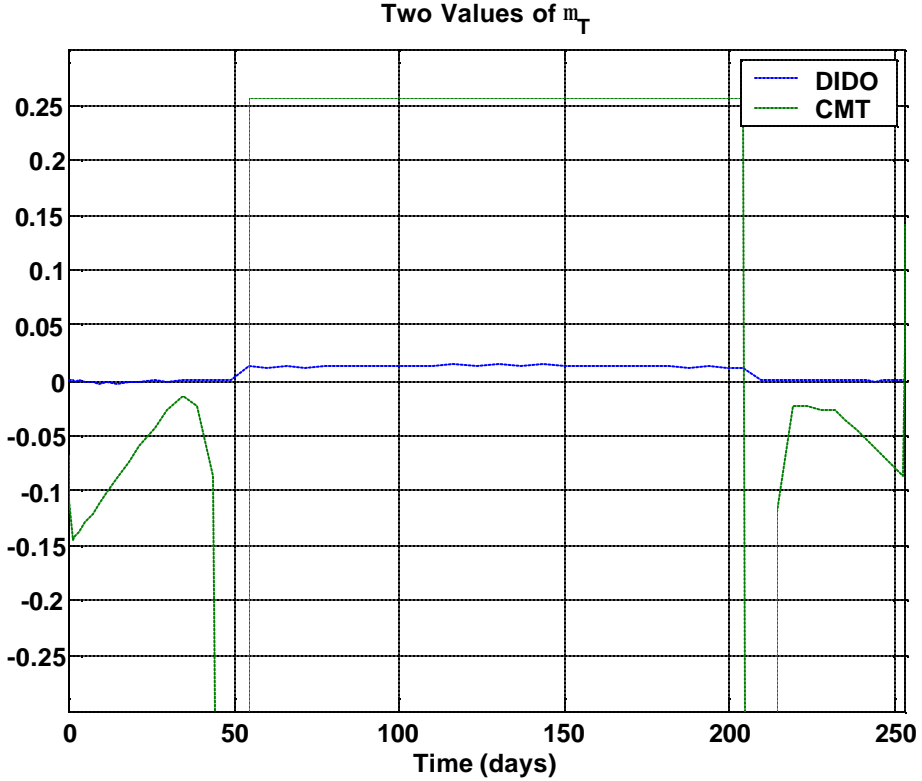
Figure 14: Comparison of DIDO and CMT Thrust Covector

We are left with two possibilities, either Eqn.(133) is incorrect, or the DIDO supplied thrust covector is incorrect.

Despite the fact that we can not verify the DIDO controls by comparison to the CMT, we can still verify the thrust magnitude switches by plotting the switching function. Application of the KKT theorem tells us that

$$\boldsymbol{m}_{T_{mag}} \begin{cases} \leq 0 & T_{mag} = 0 \\ \geq 0 \ if & T_{mag} = T_{max} \\ = 0 & 0 \leq T_{mag} \leq T_{max} \end{cases} \tag{134}$$

This implies that the controls switch between bounds at the zero crossings of the covector history. Figure **15** shows the thrust magnitude profile plotted above the switching function. The lower plot has been cropped to just either side of the x axis to better see the zero crossings. It is clear that the zero crossings of the lower plot coincide with the thrust switches as shown in the upper plot.

50
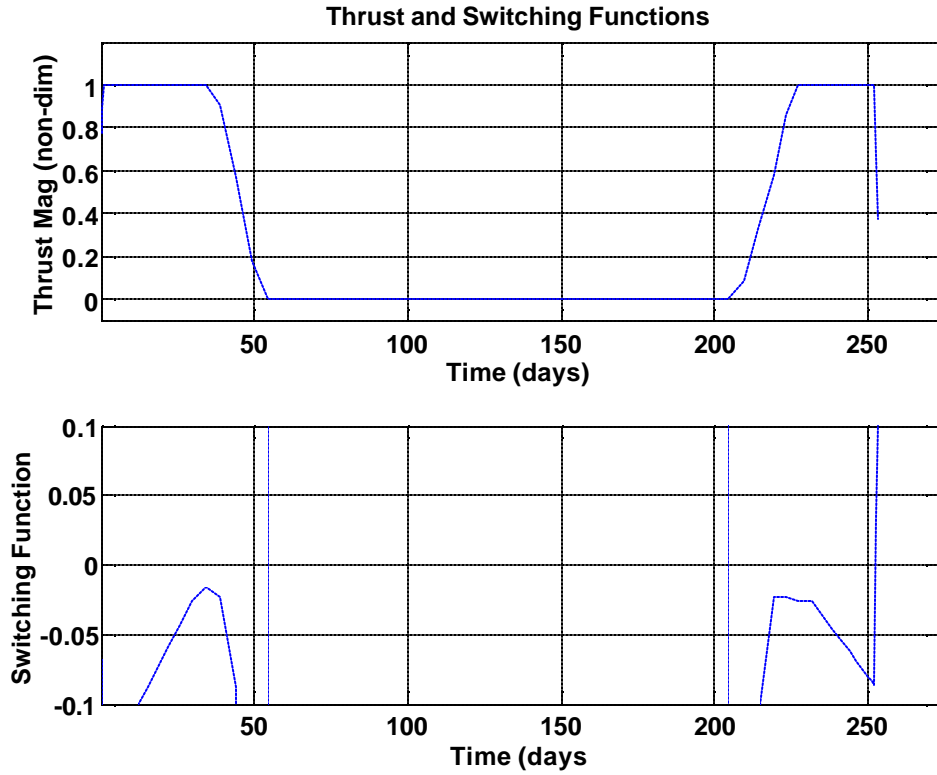
Figure 15: Switching Function (Min Fuel to Mars Rendezvous)

Finally, the Hamiltonian is plotted in Figure 16. Once again the Hamiltonian is approximately constant, verifying the necessary condition (via first integral). Note that in this case the value of the Hamiltonian is constant at zero. This is expected when time is not explicitly present in the cost function.
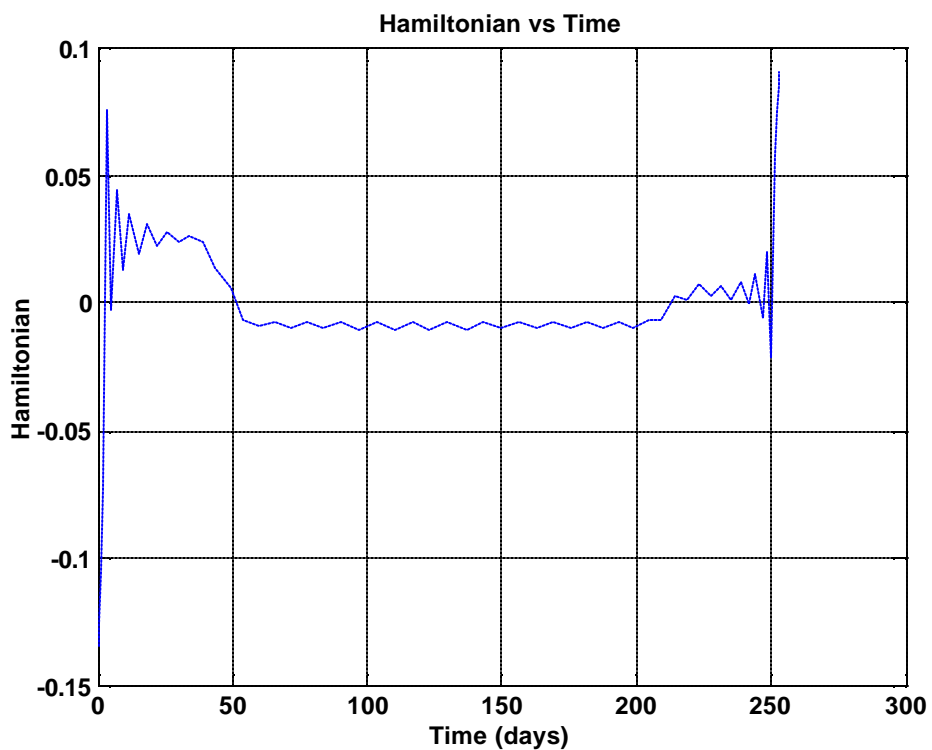
Figure 16: Hamiltonian (Min Fuel to Mars Rendezvous)

VII. OPTIMAL AEROCAPTURE PROPLEM FORMULATION

A. EVENT CONDITIONS

A spacecraft enters a planet's SOI with a known velocity relative to the planet. This velocity, known as arrival V-infinity ($V_{\infty_{arrival}}$) determine the shape of the trajectory in the planet relative frame. When $V_{\infty_{arrival}} > 0$, as in the case of aerocapture, this trajectory will be a hyperbola with the planet at the focus. For trajectories that do not intersect the atmosphere, the vehicle's trajectory is Keplerian and easily solvable at any point. For an aerocapture trajectory, the vehicle will follow such a Keplerian trajectory from the arrival point to the upper limit of the atmosphere, sometimes referred to as the atmospheric interface. The atmospheric limit is defined as the altitude above the planet's surface below which non-conservative forces such as atmospheric drag begin to perturb the trajectory. Thus only the atmospheric portion of the aerocapture trajectory need be optimized for two reasons:

- All portions of the trajectory outside the atmosphere have closed-form solutions that can be determined uniquely from the vehicle's velocity vector evaluated at the atmospheric entry point (working backward to V-infinity of arrival) and atmospheric exit point (working forward to the apoapsis).

- Above the atmospheric limit, the controls have no affect on the trajectory as there are no aerodynamic forces
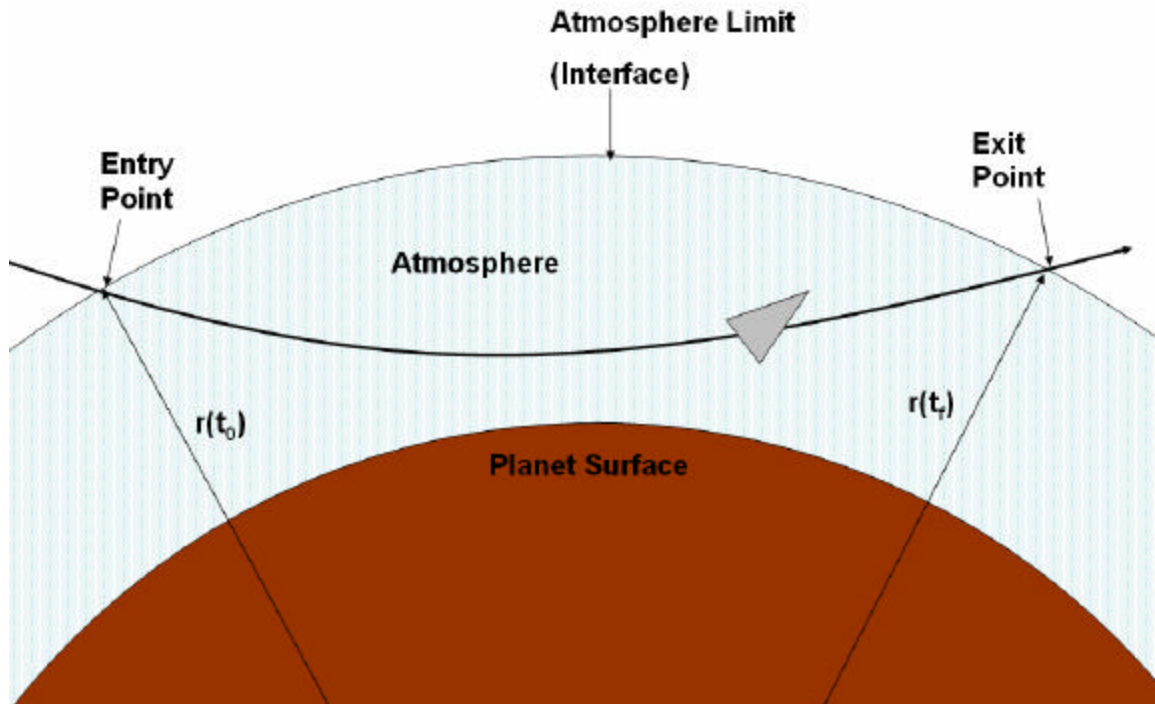
Figure 17: Atmospheric Entry and Exit Points

This being the case we can formulate our initial and final radius event conditions

as

$$r(t_0) = r_{\text{atm limit}} \tag{135}$$

$$r(t_f) = r_{\text{atm limit}} \tag{136}$$

As was the case with initial angular displacement in the low thrust problem, the initial longitude is invariant. Thus it is convenient to define the initial longitude (as defined by atmospheric entry) to be zero.

$$q(t_0) = 0 \tag{137}$$

54

The well know vis-viva equation [Ref. 2] defines the specific energy of a body at any point outside the atmosphere as a function of the vehicle's <u>inertial</u> speed and radial distance from the central body.

$$e = \frac{V^2}{2} - \frac{m}{r} \tag{138}$$

However the arrival point is defined as $r \rightarrow \infty$ so

$$e_{arrival} = \frac{V_{\infty_{arrival}}^2}{2} \tag{139}$$

Due to conservation of energy,

$$e_{arrival} = e_{atm-in} \tag{140}$$

so substituting Eqn. (138) and (139) into Eqn. (140) we get

$$\frac{V_{\infty_{arrival}}^2}{2} = \frac{V_{atm-in}^2}{2} - \frac{m}{r_{atm}} \tag{141}$$

where r_{atm} is the atmospheric limit. This can be rearranged to

$$\frac{V_{\infty_{arrival}}^2 - V_{atm-in}^2}{2} + \frac{m}{r_{atm}} = 0 \tag{142}$$

Eqn. (142) becomes the equality constraint relating the vehicle's inertial velocity at atmospheric entry to $V_{\infty_{arrival}}$. From the calculations in Appendix A, we can further relate the inertial velocity at atmospheric entry to the states as measured in the rotating frame using

$$V_{atm-in}^2 = v_0^2 + r_0^2 \Omega^2 \cos^2 f_0 + 2 r_0 v_0 \Omega \cos f_0 \cos y_0 \cos g_0 \tag{143}$$

where all state variables on the right-hand side are taken at atmospheric entry (initial time, also recall that lower-case velocity state symbols represent non -inertial components).

Similarly, we require an event condition to ensure that the vehicle's state at atmospheric exit is sufficient to target our desired apoapsis as show in Figure 18 below.
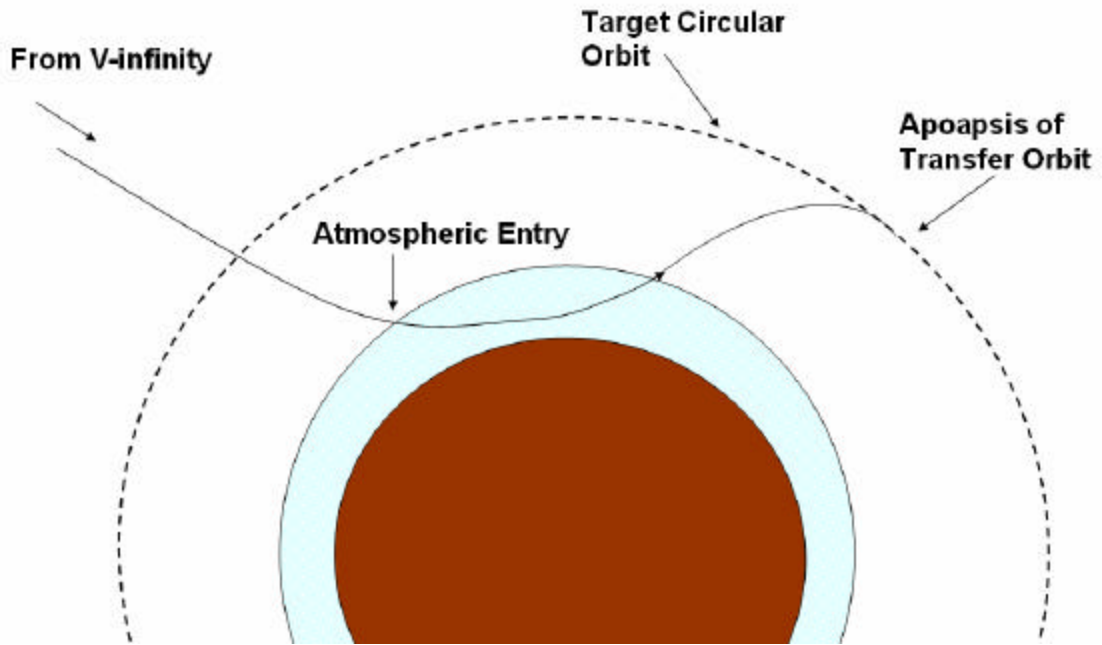
Figure 18: Targeting a Circular Orbit

Again due to conservation of energy we have

$$\boldsymbol{e}_{atm-out} = \boldsymbol{e}_{apo} \tag{144}$$

and using vis-viva we obtain

$$\frac{V_{atm-out}^2}{2} - \frac{\boldsymbol{m}}{r_{atm}} = \frac{V_{apo}^2}{2} - \frac{\boldsymbol{m}}{r_{apo}} \tag{145}$$

so V_{apo} is needed as a function of the state vector at atmospheric exit.

The angular momentum of a point mass is given by

$$\mathbf{h} = \mathbf{r} \times \mathbf{V} = rV\cos(\Gamma) \tag{146}$$

where Γ is the <u>inertial</u> flight path angle. Due to conservation of angular momentum

56

$$\mathbf{h}_{atm-out} = \mathbf{h}_{apo} \qquad (147)$$

substituting Eqn. (146) yields

$$r_{atm} V_{atm-out} \cos\left(\Gamma_{atm-out}\right) = r_{apo} V_{apo} \qquad (148)$$

because $\Gamma = 0$ at the apoapsis of the transfer orbit. This can be rearranged to solve for V_{apo} as

$$V_{apo} = \frac{r_{atm}}{r_{apo}} V_{atm-out} \cos\left(\Gamma_{atm-out}\right) \qquad (149)$$

substituting (149) into (145) we get

$$\frac{V_{atm-out}^2}{2} - \frac{\boldsymbol{m}}{r_{atm}} = \frac{1}{2}\left(\frac{r_{atm}}{r_{apo}} V_{atm-out} \cos\left(\Gamma_{atm-out}\right)\right)^2 - \frac{\boldsymbol{m}}{r_{apo}} \qquad (150)$$

which can be rearranged to

$$V_{atm-out}^2 - \left(\frac{r_{atm}}{r_{apo}} V_{atm-out} \cos\left(\Gamma_{atm-out}\right)\right)^2 - 2\boldsymbol{m}\left(\frac{1}{r_{atm}} - \frac{1}{r_{apo}}\right) = 0 \qquad (151)$$

giving us an equality constraint relating the states at atmospheric exit to our desired apoapsis. Again, using the relations derived in Appendix A we can find $V_{atm-out}$ and $\Gamma_{atm-out}$ as functions of the state variables in the rotating frame using the following relations:

$$V_{atm-out}^2 = v_f^2 + r_f^2 \Omega^2 \cos^2\boldsymbol{f}_f + 2r_f v_f \Omega \cos\boldsymbol{f}_f \cos\boldsymbol{y}_f \cos\boldsymbol{g}_f \qquad (152)$$

$$\Gamma_{atm-out} = \operatorname{atan}\left(\frac{v_f \sin\boldsymbol{g}_f}{\sqrt{\cos^2\boldsymbol{g}_f\left(v_f^2 + \Omega^2 r_f^2\right) + 2v_f r_f \Omega \cos\boldsymbol{g}_f \cos\boldsymbol{y}_f \cos\boldsymbol{f}_f}}\right) \qquad (153)$$

where in this case all the state variables on the right-hand side are again taken at atmospheric exit.

Note that these event conditions require that the apoapsis of the post-atmospheric trajectory exactly intersect the circular target orbit, also known as a Hohmann transfer.

Hohmann showed that a Hohmann transfer is the minimum-fuel transfer orbit between co-planar orbits whose ratio of radii are less than 11.94 [Ref. 7]. [Ref. 24] develops the event conditions necessary for a bi-elliptic transfer orbit where the apoapsis of the post-atmospheric trajectory has insufficient energy to reach the circular target orbit. Using the same approach, one could likewise develop the event conditions for the case where the post-atmospheric trajectory has excess energy and overshoots the target circular orbit. Unfortunately, these three cases (apoapsis undershoot, touching, and overshoot) can not easily be reconciled into one set of conditions because doing so would complicate the ΔV calculations in the next section, necessitating the introduction of an absolute value operator in the rocket equation Eqn. (156). Because the derivative of the absolute value operator is discontinuous when evaluated at zero, singularities are introduced in the Jacobian leading to serious numerical issues in solving the NLP. [Ref. 5]. For these reasons, only the "touching" case is considered in this work.

The event conditions can be summarized in vector form as as

$$
\begin{bmatrix} r_{atm\,limit} \\ 0 \\ 0 \\ r_{atm\,limit} \\ 0 \end{bmatrix} \leq \begin{bmatrix} r(t_0) \\ \boldsymbol{q}(t_0) \\ \dfrac{V_{\infty_{arrival}}^2 - V_{atm-in}^2}{2} + \dfrac{\boldsymbol{m}}{r_{atm}} \\ r(t_f) \\ V_{atm-out}^2 - \left(\dfrac{r_{atm}}{r_{apo}} V_{atm-out} \cos\left(\Gamma_{atm-out}\right) \right)^2 - 2\boldsymbol{m}\left(\dfrac{1}{r_{atm}} - \dfrac{1}{r_{apo}} \right) \end{bmatrix} \leq \begin{bmatrix} r_{atm\,limit} \\ 0 \\ 0 \\ r_{atm\,limit} \\ 0 \end{bmatrix} \quad (154)
$$

where $V_{atm-out}$ and $\Gamma_{atm-out}$ are given by Eqns. (152) and (153).

B.   COST FUNCTIONS

1.   Minimum Fuel to Circularize

The simplest performance index for aerocapture is to minimize the fuel required to circularize the orbit. Since the event conditions require the post-atmospheric trajectory's apoapsis exactly touch the target circular orbit, the delta-V can be obtained by subtracting the apoapsis velocity found using Eqn. (149) from the target circular orbit velocity

$$V_{circ} = \sqrt{\frac{m}{r_{circ}}} \tag{155}$$

such that

$$\Delta V = V_{circ} - V_{apo} \tag{156}$$

With the delta-V known, the rocket equation

$$m_{prop} = m_0 \left(1 - e^{-\frac{\Delta V}{I_{sp}g_0}} \right) \tag{157}$$

can be used to find the propellant mass required to circularize the orbit. Thus our performance index can be expressed in Mayer form as

$$J = m_{prop\ circ} \tag{158}$$

2. Minimum Heat Load

Knowing that there exists some relation between the total heat load and the required TPS mass, another reasonable performance index is to minimize the heat load. As one recalls, heat load is the integrated heating rate over the trajectory (Eqn. (50)) ; thus a natural choice is to use a Lagrange form cost function such as

$$J = \int_{t_0}^{t_f} \dot{q}(r,\ v)\ dt \tag{159}$$

However any Lagrange cost can be re-written as a Mayer cost through the addition of a state in the equations of motion. In this case, we could add heat load as a state, with dynamics given by Eqn. (50).

3. Minimum Aerocapture Mass

A more useful performance index would to minimize the total mass associated with aerocapture. The total aerocapture mass can be broken into three components, heat shield mass (also known as fore-shield mass), back-shell mass, and the propellant mass required to circularize the orbit.

59

$$m_{acap} = m_{heatshield} + m_{back-shell} + m_{prop} \tag{160}$$

The propellant mass to circularize can be found using Eqn. (157). The mass of the back-shell can be assumed to be relatively constant over a large range of heat. Thus a method is needed for determining the mass of the heat shield.

A first-order approximation for heat shield mass can be made by linearly mapping heat load to heat shield mass. Thermal analysis of the heat loads expected to be encountered by Mars Smart Lander require an approximate heat shield mass of 40 kg for every 10,000 Joules of heat load [Ref. 25]. Using this single data point and assuming a 20% margin, a crude mapping between heat load and heat shield mass can be expressed as

$$m_{heatshield} = k \int_{t_0}^{t_f} \dot{q} \, dt \tag{161}$$

where $k = \dfrac{50kg}{10,000J}$.

Since the back-shield mass is assumed to be constant, it can be neglected from the performance index. A minimum aerocapture mass performance index can now be written in Bolza form as

$$J = m_{prop} + k \int_{t_0}^{t_f} \dot{q} \, dt \tag{162}$$

It should be stressed that a much more accurate model could be obtained by mapping the heat shield mass to both heat load and peak heating rate. However, the addition of the peak heating rate term would require the cost function to be formulated as a Chebyshev minimax problem which is beyond the scope of this proof-of-concept.

C. CONTROLS

For non-thrusting, fixed angle-of-attack aerocapture trajectories, the only control during the atmospheric pass is the bank angle of the spacecraft. As in the low thrust case, coding the control as an angle and bounding it as $0 \le d \le 2p$ leads to some difficulties due to the jump discontinuity between 0 and 2π. As shown in later sections, the optimal bank angle history generally switches between π and 2π (or zero). Opening the control bound to $0 \le d \le 3p$ allows for optimal bank angles that are entirely interior. However as in the low thrust case it was eventually realized that using $\sin d$ and $\cos d$ as controls tended to yield faster and more consistently reliable solutions. Thus we have

$$\mathbf{u} = \begin{bmatrix} \sin d \\ \cos d \end{bmatrix} \tag{163}$$

where our controls are bound by

$$-1 \le \sin d \le 1 \tag{164}$$

$$-1 \le \cos d \le 1 \tag{165}$$

As in the low thrust case, this formulation of the controls requires the addition of a path constraint (given in the next section).

An alternate control scheme incorporates the bank angle as a state variable of the vehicle and instead controls the bank angle. This allows for more realistic command response behavior. However, this scheme was not incorporated into this work.

D. STATE BOUNDS

Next suitable choices must be made to bound the states. Since only the atmospheric portion of the trajectory is of concern, there is no point in allowing the radius to be any larger than the atmospheric limit. Similarly, the vehicle has a hard lower bound at the planet's surface. Considering this yields

$$r_{planet} \le r \le r_{atmos\text{-}limit} \tag{166}$$

However, recalling Eqn. (49), the atmospheric model is only valid to the scale height below which the exponential atmosphere incorrectly _decreases_ with decreasing altitude. Thus a better set of bounds is

61

$$r_{planet} + h_0 \leq r \leq r_{atmos\text{-}limit} \qquad (167)$$

Realizing that for a non-thrusting vehicle entering the atmosphere, the maximum speed will be near that at atmospheric interface. To account for the unlikely event of extremely steep entries the upper bound can be set to some arbitrary small multiple of the initial velocity.

$$0 \leq v \leq 5v_{atmos-in} \qquad (168)$$

Note however that Eqns. (25), (26), (31), (33) have singularities at $v = 0$. This can be resoled by constraining the problem as

$$\boldsymbol{e}_v \leq v \leq v_{atmos-in} \qquad (169)$$

where $\boldsymbol{e}_v$ is number slightly larger than zero.

Note that equations Eqns. (22), (25), (31) also have singularities at $\boldsymbol{f} = \pm\boldsymbol{p}$ and $\boldsymbol{g} = \pm\boldsymbol{p}$. We can prevent the singularities from being encountered by bounding these states as

$$-\boldsymbol{p} + \boldsymbol{e}_f \leq \boldsymbol{f} \leq \boldsymbol{p} - \boldsymbol{e}_f \qquad (170)$$

$$-\boldsymbol{p} + \boldsymbol{e}_g \leq \boldsymbol{g} \leq \boldsymbol{p} - \boldsymbol{e}_g \qquad (171)$$

where again $\boldsymbol{e}_f$ and $\boldsymbol{e}_g$ are small numbers greater than zero.

Finally consider longitude and heading angle. Since there are no singularities or physical bounds to contend with we are free to choose any convenient set of bounds sufficiently large to reduce the NLP search space. Note however that in both cases

$$0 \leq \begin{bmatrix} \boldsymbol{q} \\ \boldsymbol{y} \end{bmatrix} \leq 2\boldsymbol{p} \qquad (172)$$

is a poor choice. While we as humans intuitively know that these variables are continuous across these bounds, the dynamics are blind to this fact and instead see this as a discontinuity. This discontinuity can be resolved by simply opening the bounds

$$-2\boldsymbol{p} \leq \begin{bmatrix} \boldsymbol{q} \\ \boldsymbol{y} \end{bmatrix} \leq 2\boldsymbol{p} \tag{173}$$

The bounds for the complete state vector can be summarized as

$$\begin{bmatrix} r_{planet} + h_0 \\ -2\boldsymbol{p} \\ -\boldsymbol{p} + \boldsymbol{e}_f \\ \boldsymbol{e}_v \\ -2\boldsymbol{p} \\ -\boldsymbol{p} + \boldsymbol{e}_g \end{bmatrix} \leq \begin{bmatrix} r \\ \boldsymbol{q} \\ \boldsymbol{f} \\ v \\ \boldsymbol{y} \\ \boldsymbol{g} \end{bmatrix} \leq \begin{bmatrix} r_{atmos\text{-}limit} \\ 2\boldsymbol{p} \\ \boldsymbol{p} - \boldsymbol{e}_f \\ v_{atmos-in} \\ 2\boldsymbol{p} \\ \boldsymbol{p} - \boldsymbol{e}_g \end{bmatrix} \tag{174}$$

E.   PATH CONSTRAINTS

The control space in $\mathbf{u} \subset \mathfrak{R}^2$ defined by Eqns. (164) and (165) is the area of a square. A path constraint is needed to correct this control space to that of a circle. This is accomplished using the trigonometric identity

$$\sin^2 \boldsymbol{d} + \cos^2 \boldsymbol{d} - 1 = 0 \tag{175}$$

However this control surface leads to a convexity problem. Using the same technique employed for the low thrust control, the path constraint is modified to an inequality constraint

$$-1 \leq \sin^2 \boldsymbol{d} + \cos^2 \boldsymbol{d} - 1 \leq 0 \tag{176}$$

This transforms the control space to a circular disc of unit radius which is a convex surface. Again, this temporary violation of physics will be resolved by the Minimum Principle which forces the controls to the boundary of the control space, in this case, onto the unit circle.

Other path constraints of potential importance to the mission designer are limiting maximum dynamic pressure, load-factor or heating-rate as given by Eqns. (37), (42) and (50) respectively.

F.   NECESSARY CONDITIONS

Assuming a Mayer cost ($\mathbf{F} \in \varnothing$), the Hamiltonian for the aerocapture problem is

$$
\begin{aligned}
H = \mathbf{1}_r \left(v \sin \mathbf{g} \right) + \mathbf{1}_q \left(\frac{v \cos \mathbf{g} \cos \mathbf{y}}{r \cos \mathbf{f}} \right) + \mathbf{1}_f \left(\frac{v \cos \mathbf{g} \sin \mathbf{y}}{r} \right) \cdots \\
+ \mathbf{1}_v \left(-\frac{D}{m} - g \sin \mathbf{g} + cf_v \right) \cdots \\
+ \mathbf{1}_y \left(\frac{L \sin \mathbf{d}}{mv \cos \mathbf{g}} - \frac{v}{r} \cos \mathbf{g} \cos \mathbf{y} \tan \mathbf{f} + cf_y + co_y \right) \cdots \\
+ \mathbf{1}_g \left(\frac{L \cos \mathbf{d}}{mv} - \frac{g \cos \mathbf{g}}{v} + \frac{v \cos \mathbf{g}}{r} + cf_g + co_g \right)
\end{aligned}
\tag{177}
$$

Note that all of the aerocapture Lagrange costs are pure state costs meaning that they are not function of the controls. Since the partial of the augmented Hamiltonian will be taken in a moment, the assumption of a Mayer cost does not impact the formulation of the necessary conditions.

The augmented Hamiltonian is

$$
\begin{aligned}
H^{\dagger} = \mathbf{1}_y \left(\frac{L \sin \mathbf{d}}{mv \cos \mathbf{g}} \right) + \mathbf{1}_g \left(\frac{L \cos \mathbf{d}}{mv} \right) + \mathbf{m}_{sd} \sin \mathbf{d} \cdots \\
+ \mathbf{m}_{cd} \cos \mathbf{d} + \mathbf{m}_{rel} \left(\sin^2 \mathbf{d} + \cos^2 \mathbf{d} - 1 \right) + \text{pure state terms}
\end{aligned}
\tag{178}
$$

where all the pure-state terms have been grouped together and where $\mathbf{m}_{sd}, \mathbf{m}_{cd}$ and $\mathbf{m}_{rel}$ are the Lagrange multipliers associated with the two controls and the path constraint relating them respectively [Eqn. (176)].

Applying the necessary condition for optimality by taking the partial derivative of the augmented Hamiltonian with respect to each control we obtain

$$
\frac{\partial H^{\dagger}}{\partial (\sin \mathbf{d})} = \frac{\mathbf{1}_y L}{mv \cos \mathbf{g}} + \mathbf{m}_{sd} + 2\mathbf{m}_{rel} \sin \mathbf{d} = 0
\tag{179}
$$

$$
\frac{\partial H^{\dagger}}{\partial (\cos \mathbf{d})} = \frac{\mathbf{1}_g L}{mv} + \mathbf{m}_{cd} + 2\mathbf{m}_{rel} \cos \mathbf{d} = 0
\tag{180}
$$

which can be re-arranged to solve for the controls

$$\sin \boldsymbol{d} = -\frac{\boldsymbol{l}_y L}{2mv\boldsymbol{m}_{rel} \cos \boldsymbol{g}} - \frac{\boldsymbol{m}_{sd}}{2\boldsymbol{m}_{rel}} \tag{181}$$

$$\cos \boldsymbol{d} = -\frac{\boldsymbol{l}_g L}{2mv\boldsymbol{m}_{rel}} - \frac{\boldsymbol{m}_{cd}}{2\boldsymbol{m}_{rel}} \tag{182}$$

THIS PAGE INTENTIONALLY LEFT BLANK

VIII. OPTIMAL AEROCAPTURE RESULTS

A.   PROCESS

Problems were solved beginning with easier problem formulations before moving on to more challenging cost functions and higher fidelity. Solutions were obtained for non-rotating planets with fixed initial conditions and minimum fuel to circularize as the performance index. Next minimum heat-load trajectories were solved before attempting rotating atmospheres. With these successes in hand, the initial conditions were relaxed such that the velocity at atmospheric entry need only agree with the arrival V-infinity. This allowed for solutions with excess V-infinity at arrival to be obtained. Finally, the solution for minimum total aerocapture mass was obtained.

B.   MINIMUM AEROCAPTURE MASS AT MARS WITH ZERO ARRIVAL V-INFINITY

This case considered a vehicle arriving at a rotating Mars with zero excess velocity with minimum total aerocapture mass as the performance index. This initial arrival condition could occur in the case of a low thrust heliocentric trajectory whereby the interplanetary trajectory is a rendezvous.

Although only 30 nodes were necessary to obtain a solution, using 50 nodes greatly increased the accuracy of the solution. The resulting performance index breakdown is given in Table 4. The total aerocapture mass (minus back-shell mass which is assumed constant) is only 19.14 kg. This low value can be attributed to poor modeling (poor choice for k) in Eqn. (161) as well as the low heat loads experienced due to the zero V-infinity at arrival.

Propellant mass	10.63 kg
Front-shield mass	8.5 kg
Total	19.14 kg

Table 4: Cost Function Breakdown (Zero Arrival V-inf)

Even taking these factors into account, the optimal aerocapture mass is of significant savings when compared to the required mass for a pure propulsive injection maneuver. Using the same main engine and bi-propellant modeled for the post-aerocapture circularization maneuver, the required propellant mass for the pure-propellant capture is 201.44 kg. Figure 19 shows the altitude, latitude and longitude histories during the atmospheric portion of the trajectory. The circles represent the DIDO solutions at the node points, whereas the line represents the Runga-Kutta propagated solution (note the strong agreement between the two indicating feasibility). As constrained, the trajectory begins and ends at the defined atmospheric interface of 125 km. The minimum altitude of 70.14 km occurs at the 2.65 minute mark of the 12.24 minute trajectory. Note that the initial latitude solution for the pass is very nearly zero (0.7 deg) and that the trajectory proceeds easterly.
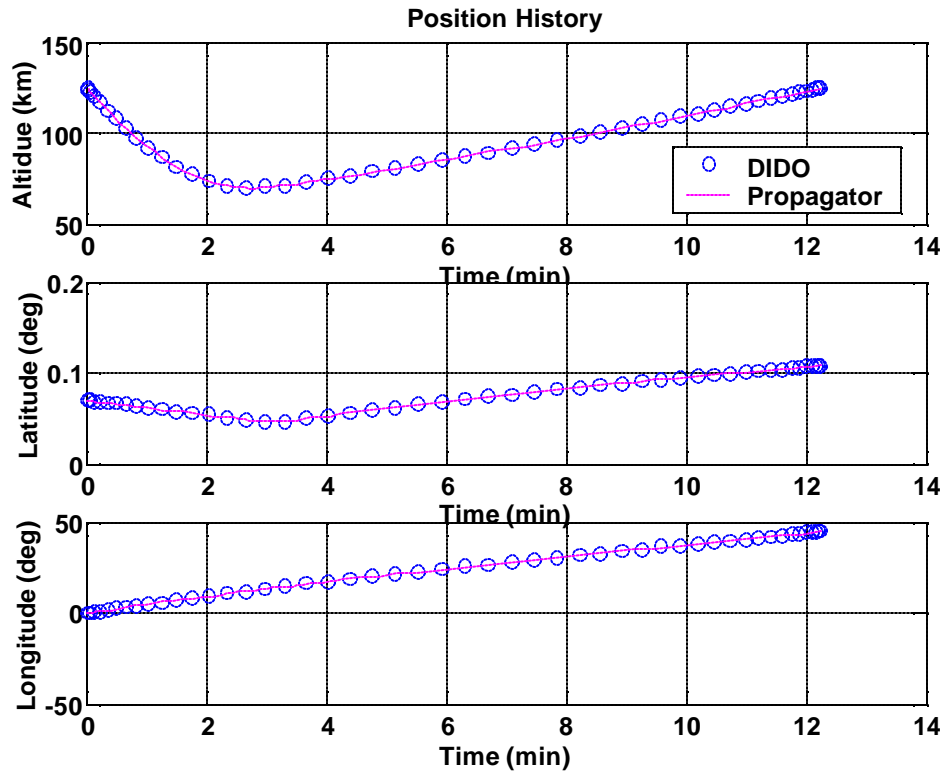

Figure 19: Position History (Zero Arrival V-inf)

Figure 20 shows the result of propagating the trajectory beyond the atmospheric interface. The spacecraft proceeds to an altitude of 295.4 km, only 4.7 km in error of the

targeted altitude. This error is attributed to the error in the final states at atmospheric and will be discussed more fully ahead.
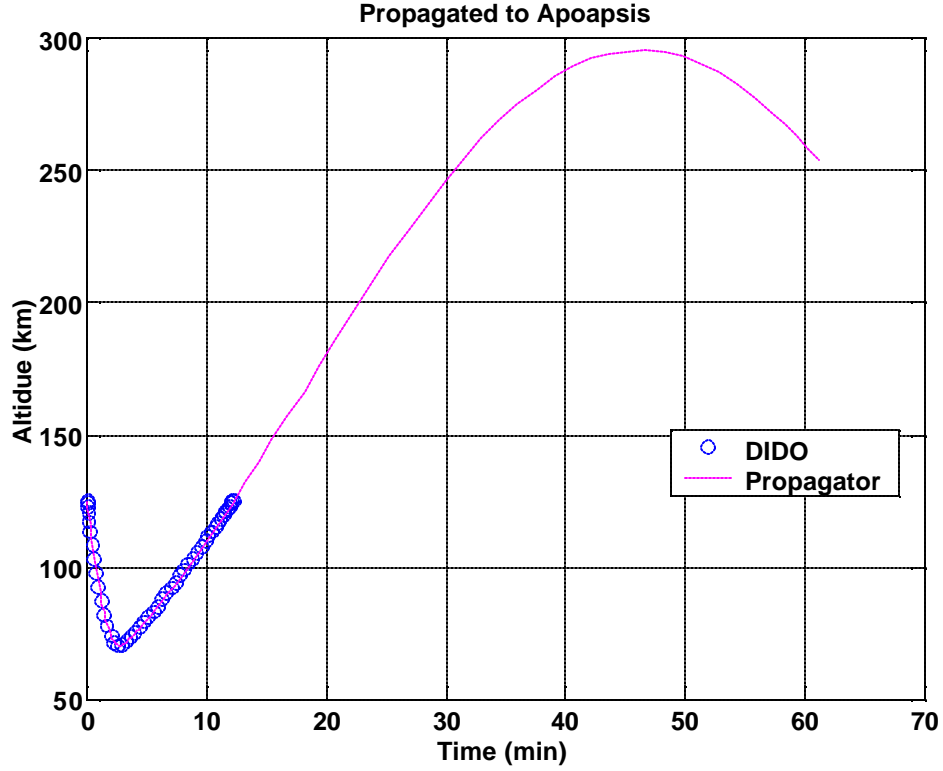
Figure 20: Propagated to Apoapsis (Zero Arrival V-inf)

The velocity state histories are given in Figure 21 and demonstrate the "backwards-S curve" in speed characteristic to aerocapture trajectories. The trajectory begins with an inertial speed of 4949.3 m/s and a relatively shallow flight path angle of -7.4 deg. The initial heading is only -0.09 deg, agreeing with the due easterly track in. Taken together, it is clear that the optimal solution is to fly in the direction of the rotating atmosphere at location of the atmosphere's greatest velocity (the equator). This trajectory gives the minimum relative speed between the atmosphere and the vehicle, thus reducing the heating-rate which is proportional to V^M. It is interesting to note that even when the problem is seeded with a westerly-tracking guess, DIDO still returns an easterly optimal solution. The inertial velocity at atmospheric exit is 3523.5 m/s for a total aerocapture delta-V of 1425.8 m/s.
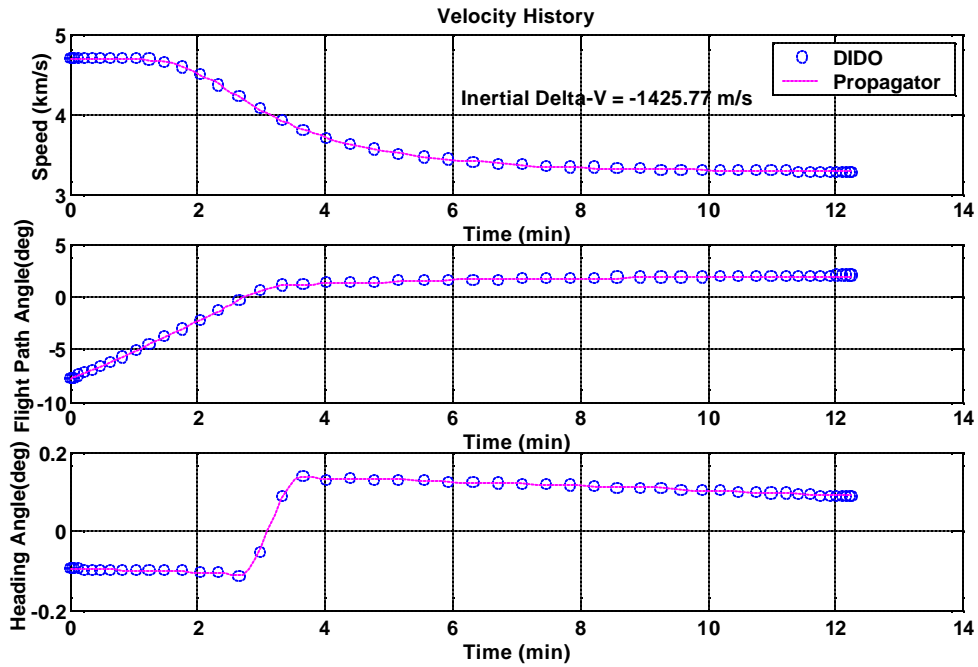
Figure 21: Velocity History (Zero Arrival V-inf)

The accuracy of the solution can be evaluated by comparing the DIDO terminal states with those from the propagator as shown in Table 5. The fact that the altitude indeed hits its target value (the only explicitly constrained final state) demonstrates the accuracy of the solution. The error that remains is likely due to these errors being less than the tolerances set in DIDO, thus causing the solver to exit. Furthermore, radius, not altitude is the actual state vector used in the solution. Redefining the equations of motion to use altitude as a state instead may allow for increased accuracy.

State	DIDO value	Propagator value	Absolute Error	Percent Error
H_f	125 km	124.52 km	-0.4762 km	0.3824 %
θ_f	44.68 deg	44.67 deg	-0.0111 deg	0.0248 %
ϕ_f	0.11 deg	0.11 deg	0.0005 deg	0.4335 %
v_f	3274.5 m/s	3272.7 m/s	-1.8559 m/s	0.0567 %
γ_f	0.09 deg	0.09 deg	0.0011 deg	1.2560 %
σ_f	2.02 deg	1.98 deg	-0.0328 deg	1.6523 %

Table 5: Propagated Accuracy (Zero Arrival V-inf)

Figure 22 shows the optimal bank angle history during the aerocapture pass. The blue circles represent the DIDO solution controls, whereas the red dots represent the CMT derived controls evaluated using Eqns. (181) and (182). For the bulk of the trajectory, the bank angle takes one of two approximate values, 0 deg (lift-up) or 180 deg (lift-down). This choice of extreme controls often occurs in optimal control solutions. At some points, the DIDO control solution actually oscillates between -180 deg and 180 deg which of course are equivalent. The same controls have been shifted to lie between $0 \le \sigma \le 2\pi$ in Figure 23 to reduce this numerical irregularity. Again, note the excellent agreement between the DIDO solution controls and the CMT controls. The only significant divergence between the two occurs late in the problem when the vehicle is near its slowest and highest portion of the trajectory. In this energy state, the performance index is of greatly reduced sensitivity to the control (in other words, these errors are unimportant to the solution.) This agreement verifies that the first-order necessary conditions have been met strengthening the argument that the solution is at least a local minimum. Furthermore, the flatness of the Hamiltonian in Figure 24 proves verification of the first integral further contributing to the claim of optimality.
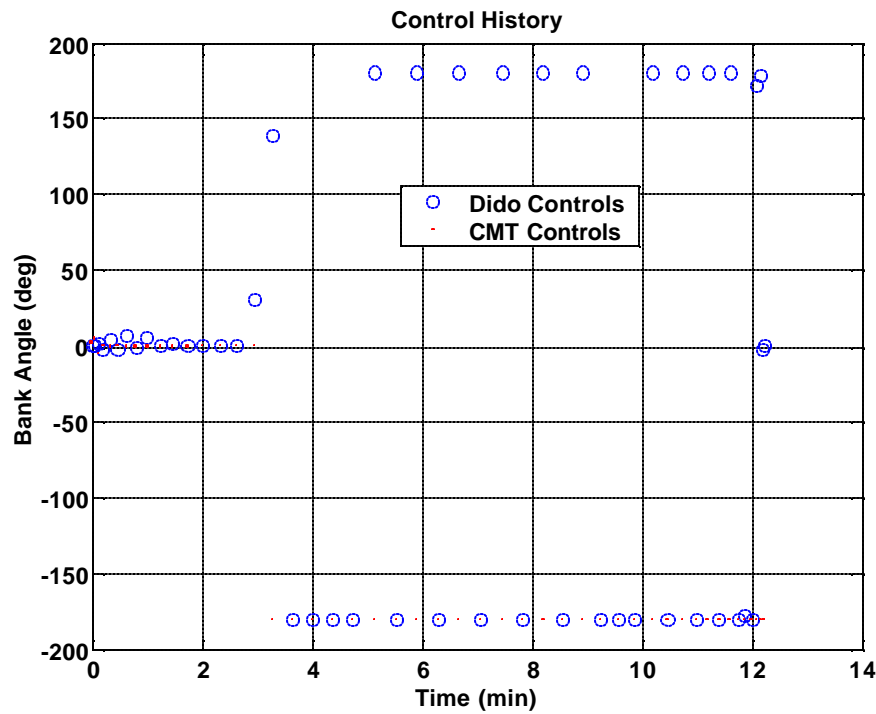
Figure 22: DIDO and CMT Controls (Zero Arrival V-inf)
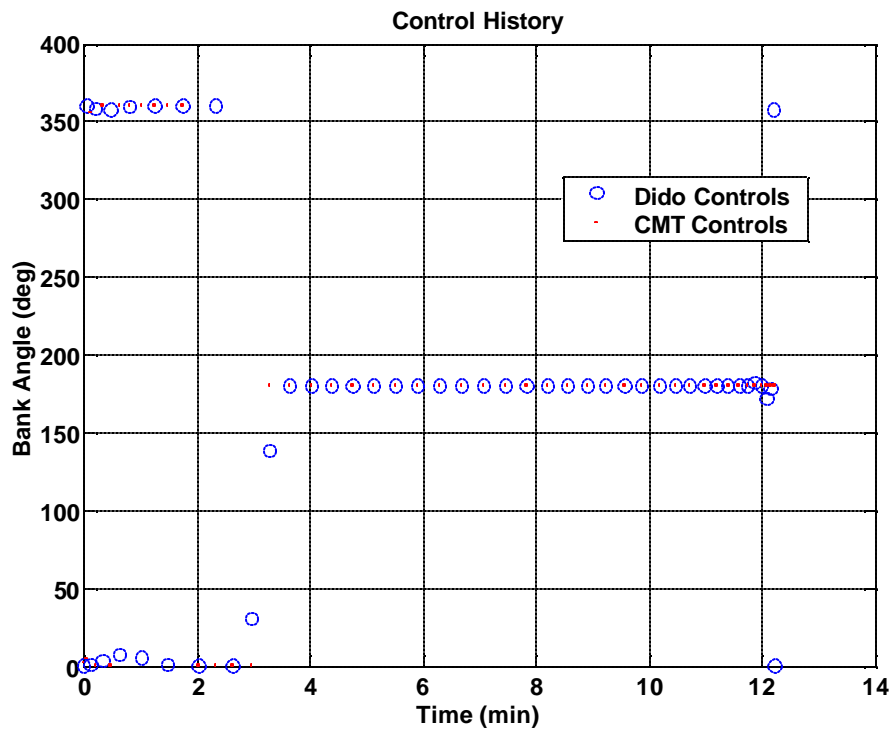
Figure 23: DIDO and CMT Controls (0-2p) (Zero Arrival V-inf)

The bank angle "switch" occurs at approximately 3.2 minutes, fully 30 seconds after minimum altitude passage. A possible explanation for this switching strategy is as follows: a steep, lift-up entry trajectory allows for deep atmospheric penetration with positive curvature. Once the "corner has been turned" at nadir and the velocity state is such that atmospheric exit is guaranteed, the vehicle flips lift-down essentially "clinging" to the atmosphere. This extends the time within the atmosphere but on the slower side of the minimum altitude where the heating rate penalty is less severe.
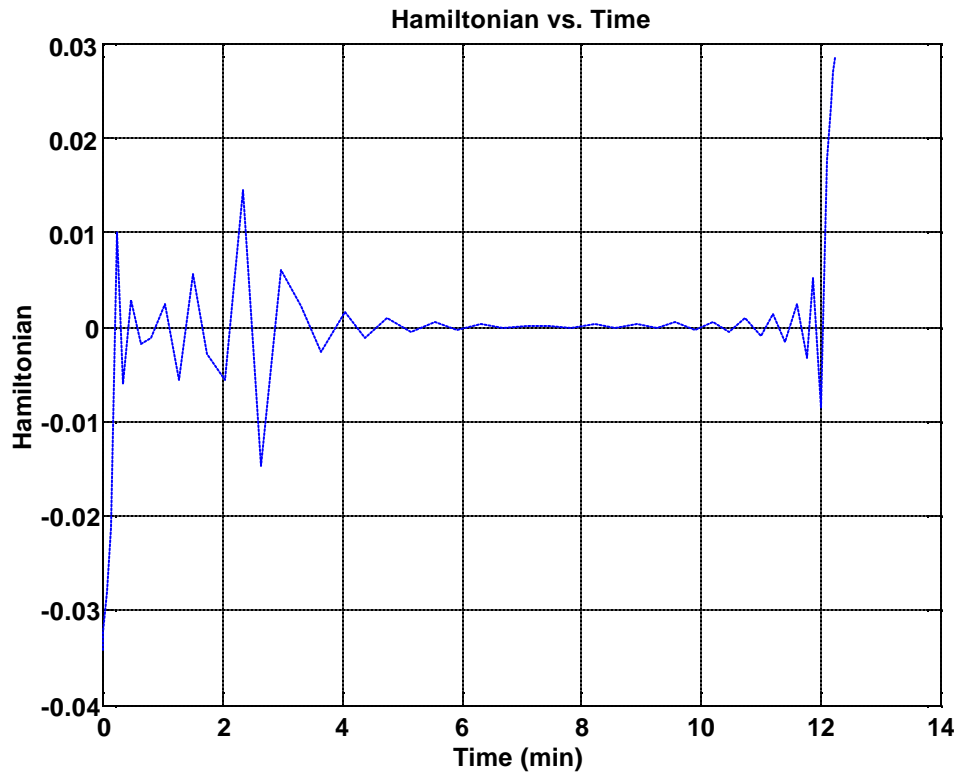
Figure 24: Hamiltonian (Zero Arrival V-inf)

The heating rate over the trajectory is given in Figure 25. The peak heating rate of 7.44 W/cm^2 occurs at 140.18 sec (2.34 min). The total heat load was calculated as 1700.38 J/cm^2 from the heating rate history using a trapezoidal integration scheme (MATLAB's "*trapz*" command).

73
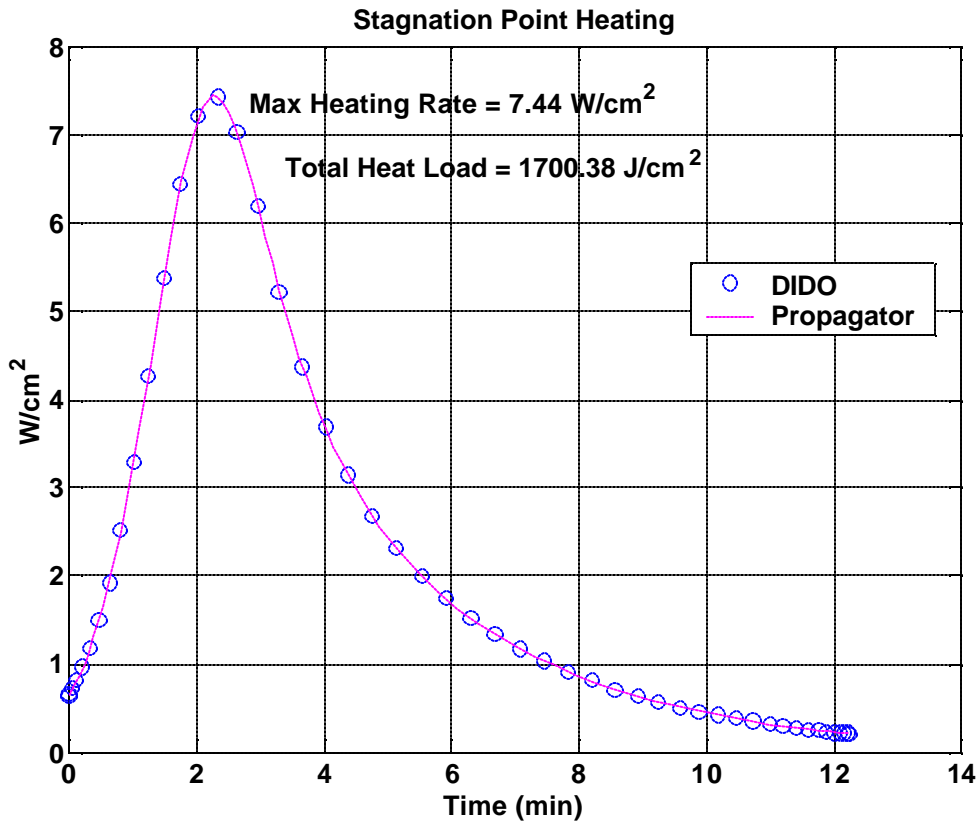
Figure 25: Heating rate (Zero Arrival V-inf)

The following figures show the time history of the body accelerations resolved in the Frenet frame and shows the total acceleration peaking at -0.85 g's at time 158.94 sec (2.65 min), the vast majority of which is in the anti-tangential direction with small normal and bi-normal components. Not surprisingly, the peak dynamic pressure (shown in Figure 28) of 505.71 Pa occurs at the same time (recall from Eqn. (38) that the tangential acceleration is a function of drag and mass only).
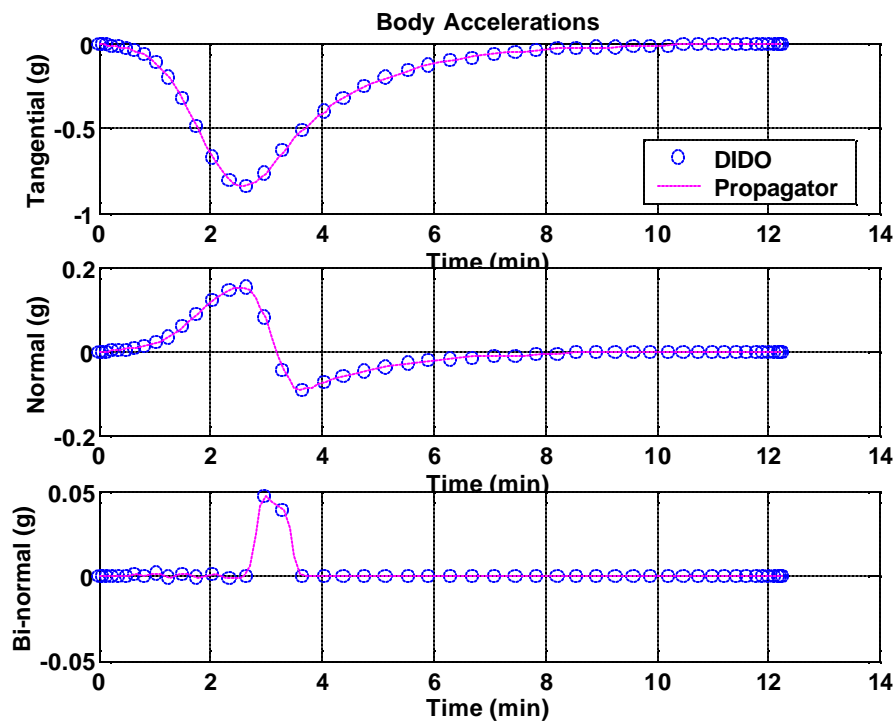
Figure 26: Body Accelerations (Zero Arrival V-inf)
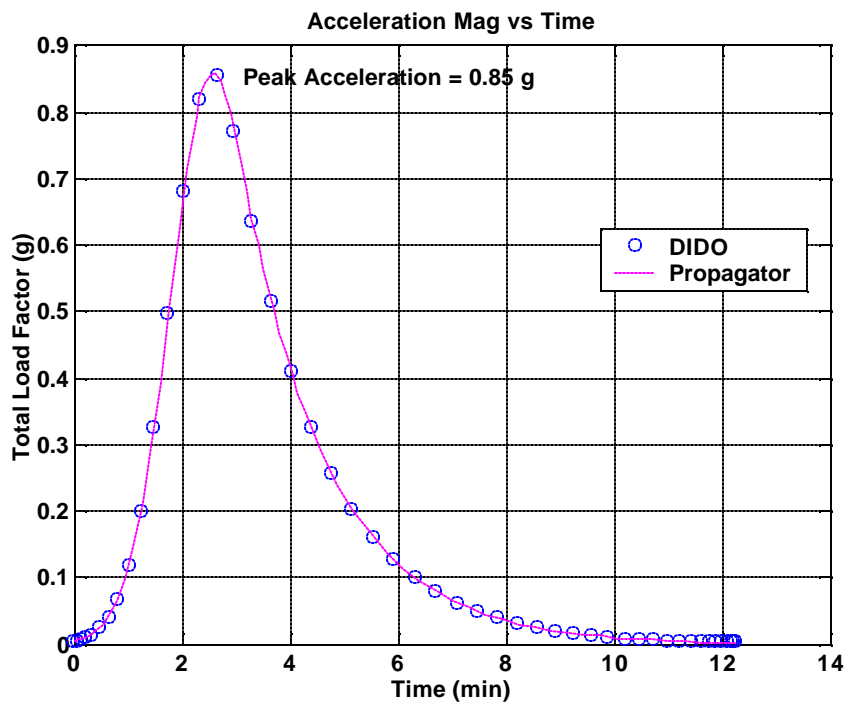
Figure 27: Total Acceleration (Zero Arrival V-inf)
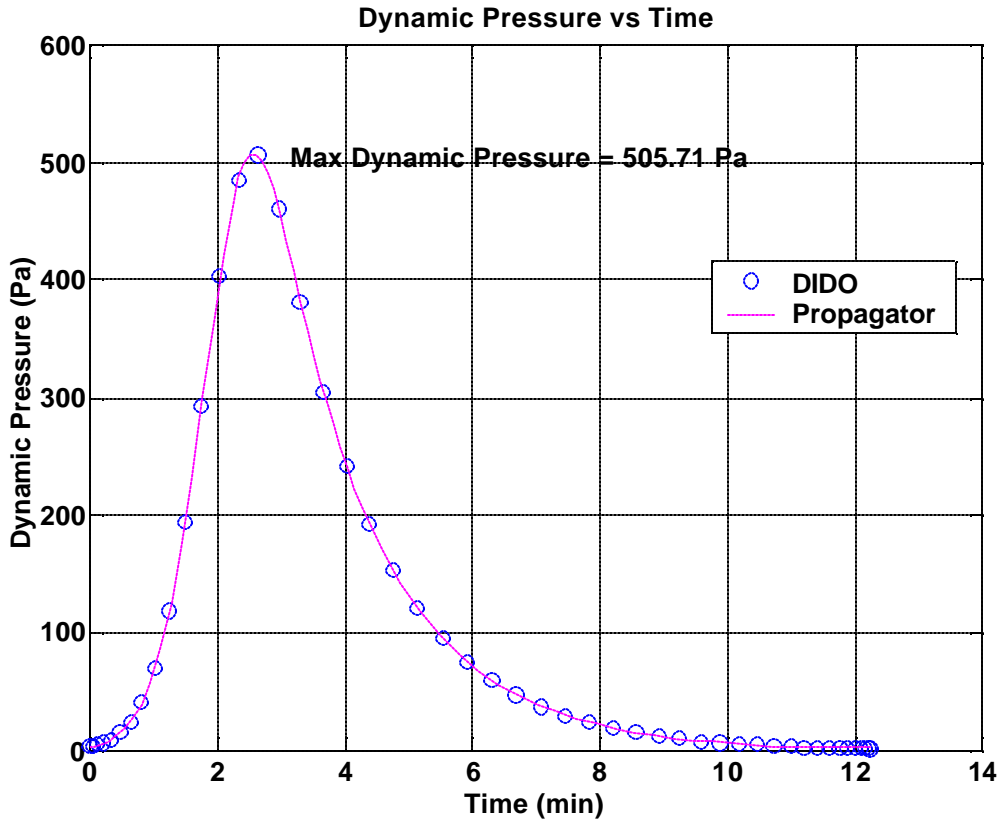
Figure 28: Dynamic Pressure (Zero Arrival V-inf)

Finally, selected orbit elements are plotted versus time in Figure 29. One can see that the non-dimensional specific energy drops from zero energy (recall that the vehicle begins with zero arrival V-infinity) and that the eccentricity begins at a parabolic value of one before decaying to a near-circular value of 0.04 at atmospheric exit. The apoapsis begins at positive infinity (as it is singular for a parabola) and decays to a non-dimensional value corresponding to 300.0 km.
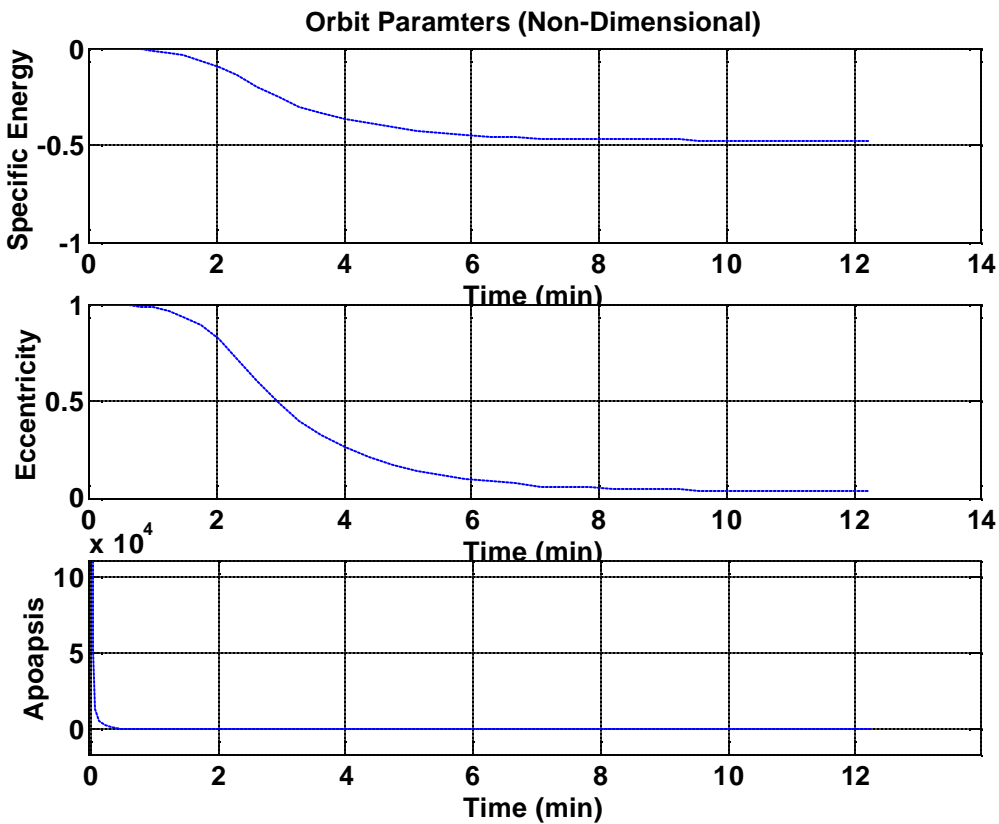
Figure 29: Selected Orbit Parameters (Zero Arrival V-inf)

C. MINIMUM AEROCAPTURE MASS AT MARS WITH EXCESS ARRIVAL V-INFINITY

This case considered a vehicle arriving at a rotating Mars with an excess velocity with minimum total aerocapture mass as the performance index. In this case, the initial arrival velocity is 5.2 km/s. This roughly equates to the arrival velocity expected from an impulsive Hohman transfer between Earth and Mars.

The solution given below was obtained using the solution from Section B above and bootstrapping up by increments of 10 nodes until a satisfactory solution was obtained with 90 nodes. The cost breakdown for this solution is given in Table 6. Although this trajectory only requires one kilogram more of propellant, the required heat shield mass is slightly more than double the amount required for the zero arrival V-infinity solution. As

shall be seen, this is due to the significantly higher thermal loads placed on the vehicle during the atmospheric pass.

Propellant mass	11.81 kg
Front-shield mass	16.94 kg
Total	28.75 kg

Table 6: Cost Function Breakdown (Excess Arrival V-inf)

For this case, the cost savings when compared to a pure-propulsive capture are even more significant with the pure-propulsive capture requiring a whopping 386.4 kg. Figure 30 shows the altitude, latitude and longitude histories during the atmospheric portion of the trajectory. Note once again the strong agreement between the DIDO state history and the propagated solution. The minimum altitude of 58.5 km occurs 94.63 sec (1.58 min) into the 601.02 sec (10.02 min) trajectory. Again the optimal solution begins near zero latitude and tracks easterly with the rotating atmosphere.
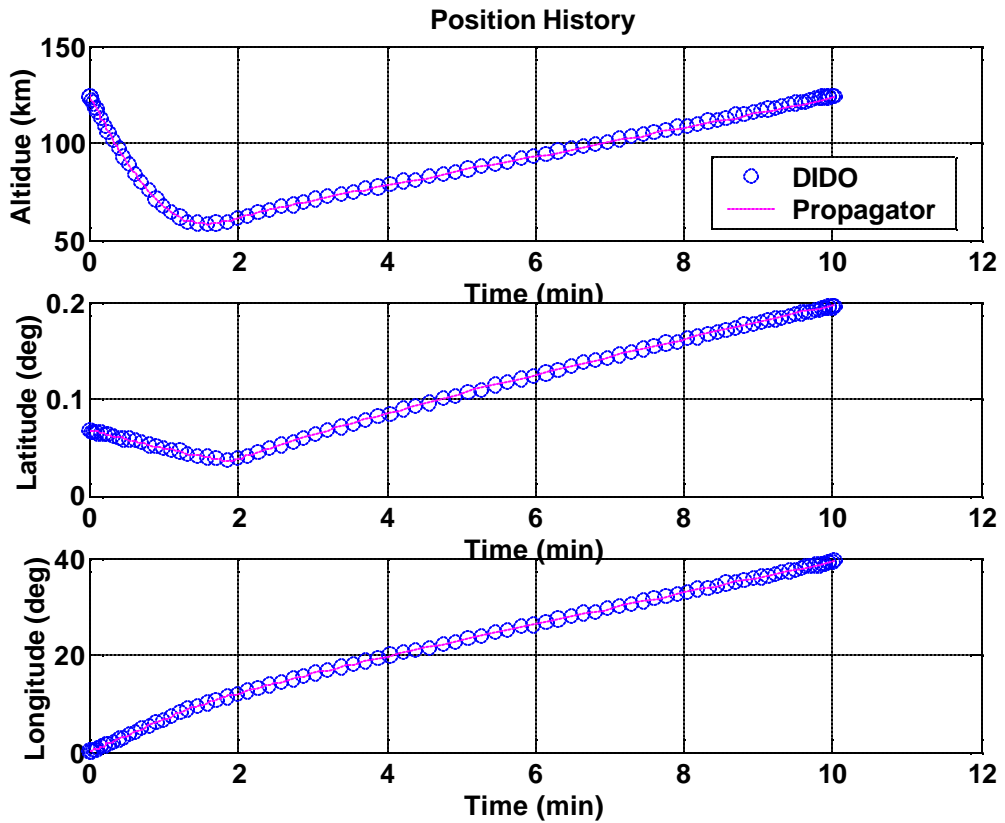
Figure 30: Position History (Excess Arrival V-inf)

Figure 31 shows the continued propagation beyond the atmospheric exit point. In this case the propagated apoapsis reaches only 277.28 km, 22.72 km short of the targeted 300 km altitude. This error is likely due altitude error at atmospheric interface (discussed shortly) magnified with time.
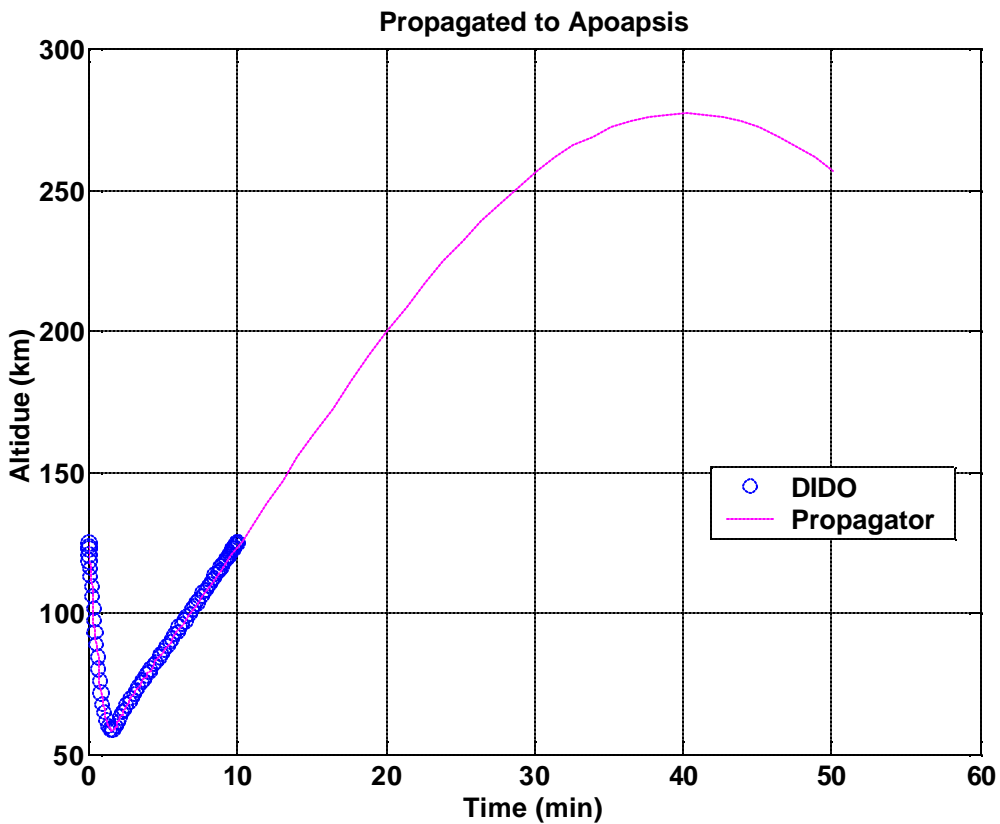
Figure 31: Propagating to Apoapsis (Excess Arrival V-inf)

Figure 32 gives the velocity state histories with an inertial entry velocity of 7178.8 km/s and initial inertial flight path angle of -10.47 deg. The exit velocity is 3517.1 km/s for a significant delta-V of 3661.8 m/s.
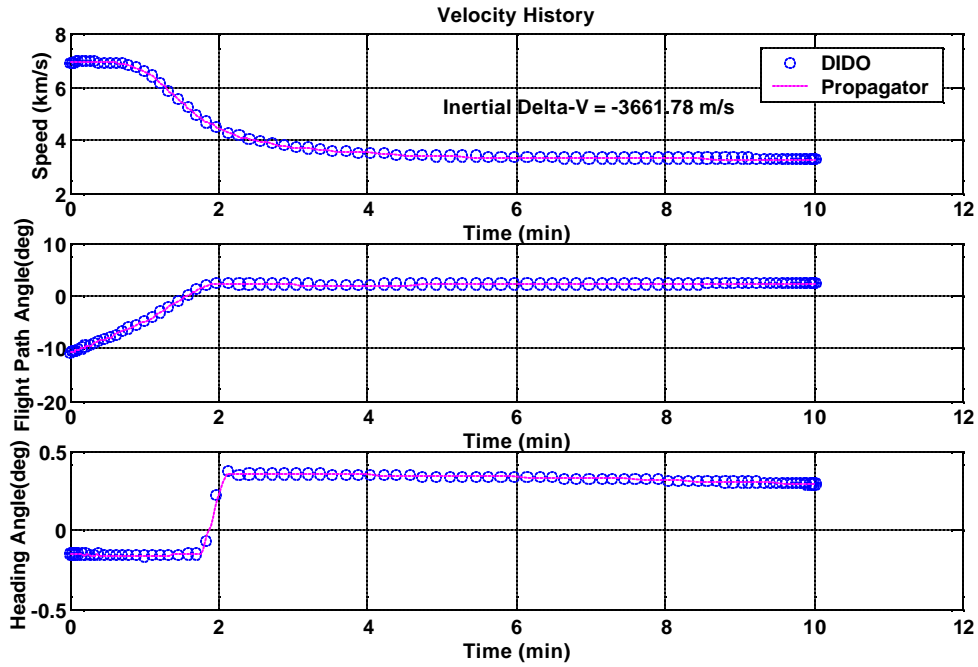
Figure 32: Velocity History (Excess Arrival V-inf)

As shown in Figure 33, this solution's altitude trajectory begins with a steeper flight path angle and penetrates deeper into the atmosphere than the slower, zero arrival V-infinity solution. Note that although it penetrates deeper, the time of passage is significantly shorter. As we shall soon see, this contributes to a larger, but narrower heating-rate pulse which helps to reduce the total heat load.
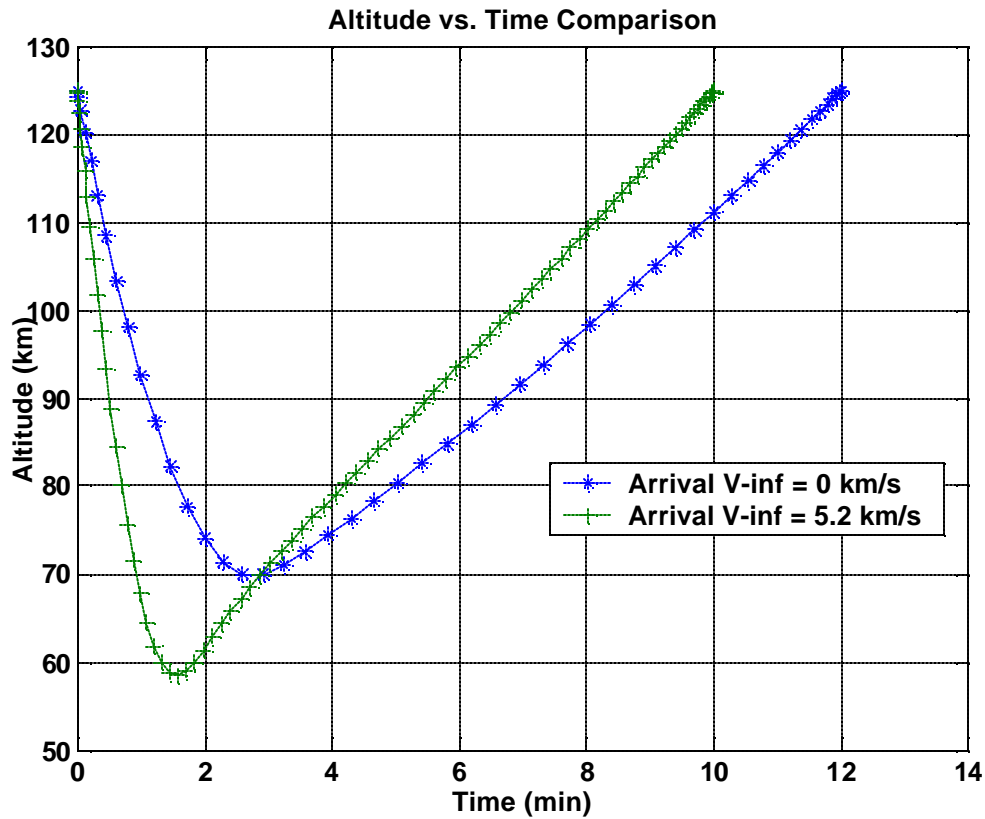
Figure 33: Altitude Profile Comparison (Excess Arrival V-inf)

The accuracy and feasibility of the solution is shown in the following table. The error between the propagated solution and the DIDO solution is small enough to declare convergence. Note that although the final flight path angle has a large percentage error, the absolute error is less that 0.1 deg. Because the final value of the flight path is itself small, this makes the error appear large.

State	DIDO value	Propagator value	Absolute Error	Percent Error
H_f	125 km	123.67 km	-1.3323 km	1.0773 %
q_f	39.42 deg	39.39 deg	-0.0301 deg	0.0763 %
f_f	0.20 deg	0.20 deg	0.0011 deg	0.0763 %
v_f	3268.11 m/s	3262.32 m/s	-5.7845 m/s	0.1773 %
y_f	-0.53 deg	-0.53 deg	0.0001 deg	0.0270 %
g_f	2.35 deg	2.25 deg	-0.0989 deg	4.3985 %

Table 7: Propagated Accuracy (Excess Arrival V-inf)

The bank control history is given in Figure 34. The "bank-bang" nature of the control can be seen as the vehicle begins the trajectory lift-up before abruptly switching to lift-down at approximately 1.8 minutes. Again, the DIDO solution can be seen flipping back and forth between +180 and -180 which are of course equivalent. Both the switch as well as the agreement between the DIDO controls and the CMT controls is more prevalent in this case, likely do to the significantly larger number of nodes in the solution. Once again this satisfies the first order necessary conditions for optimality. Again the switch occurs after (but closer to) minimum altitude passage by approximately 13 seconds. The optimality of the solution is further supported by the constancy of the first integral in Figure 35 (that is to say the flatness of the Hamiltonian to the 10^{-2}).
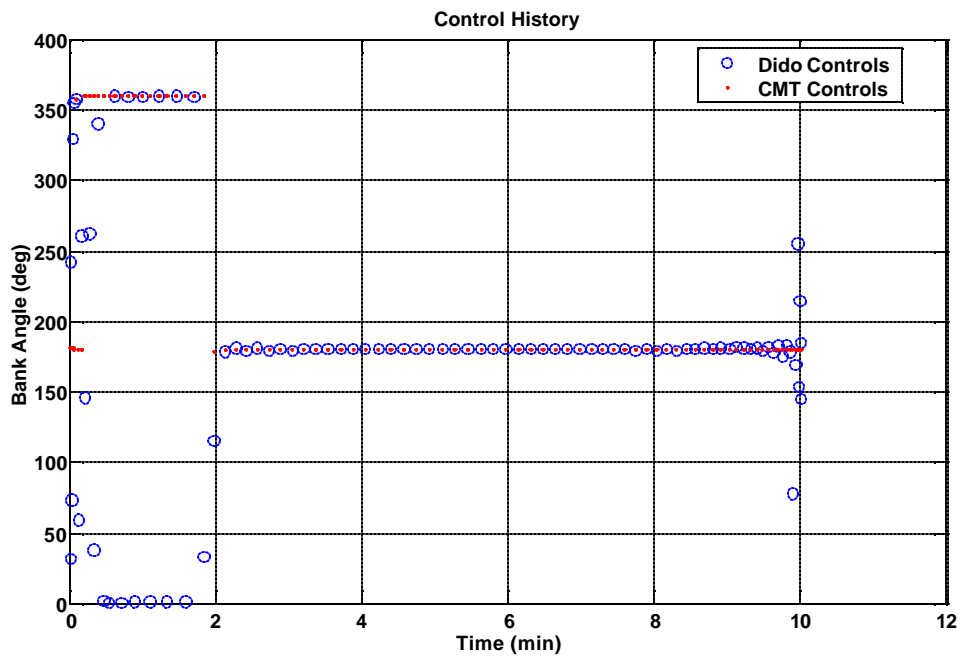
Figure 34: DIDO and CMT Control History (Excess Arrival V-inf)
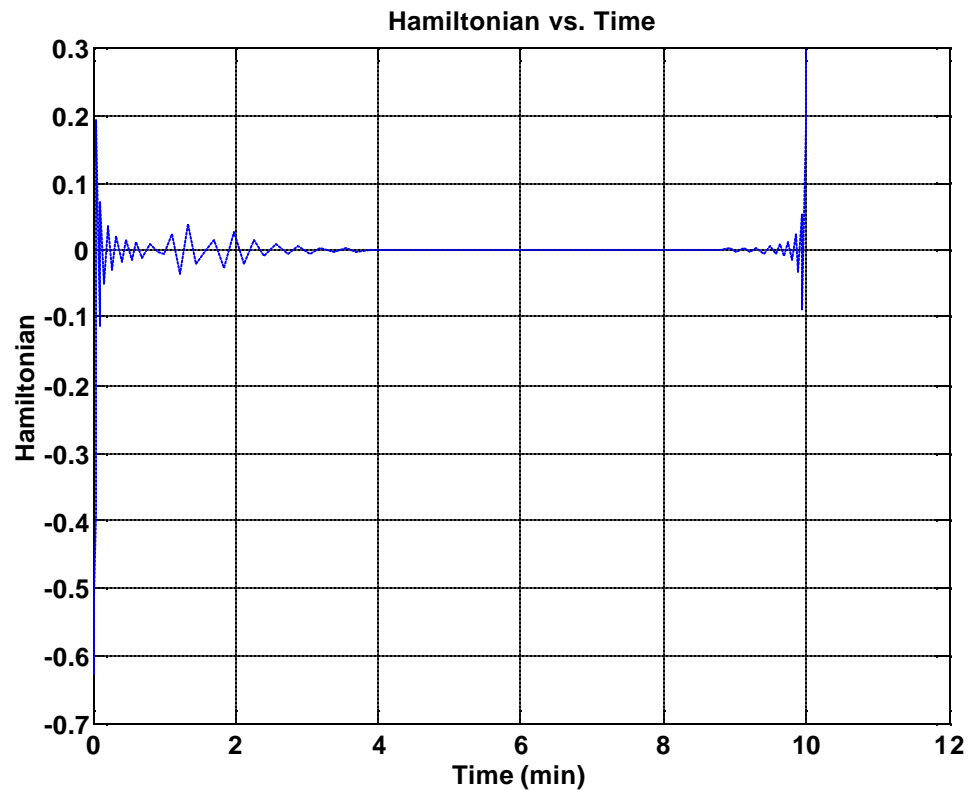
Figure 35: Hamiltonian (Excess Arrival V-inf)

84

The heating rate at the stagnation point is given in the following figure. The peak heating rate of 35.02 W/cm^2 occurs at time 72.76 sec (1.21 min) and the total heat load is 3388.37 J/cm^2 – almost double the value for the earlier non-rotating case. As mentioned previously, the duration of the heat pulse is quite short, less than a minute as measured at the half-maximum point. This contrasts with the non-rotating case where the half-maximum pulse width was approximately three minutes in duration.
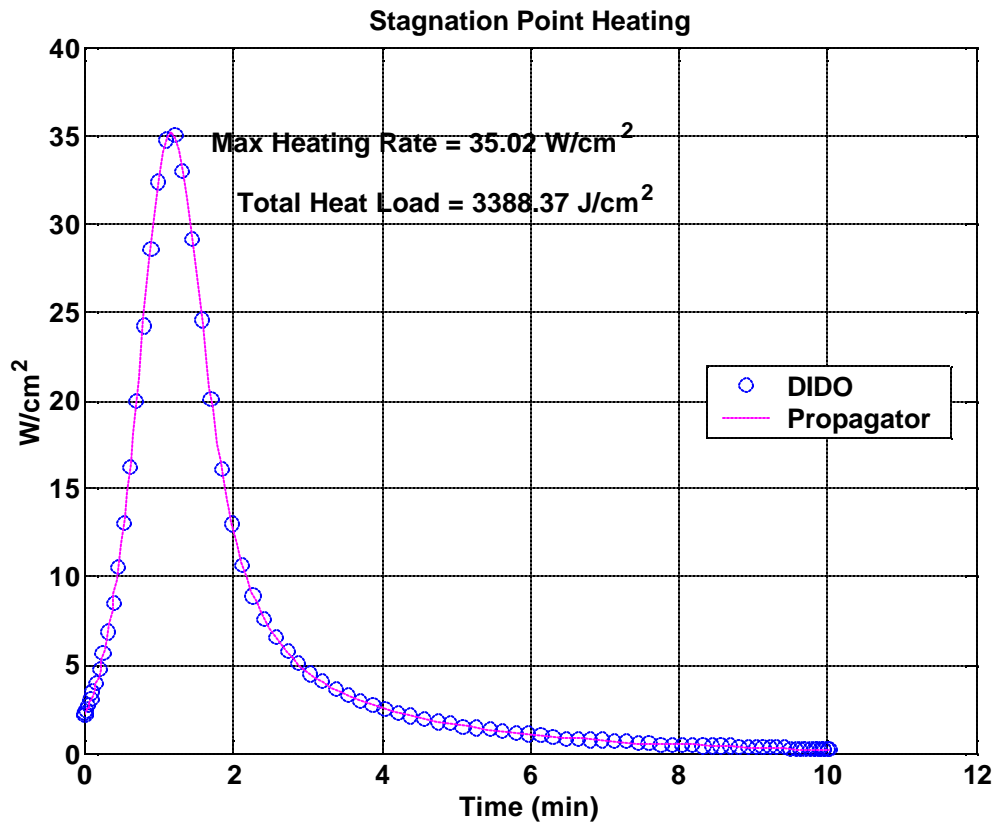
Figure 36: Stagnation Point Heating Rate (Excess Arrival V-inf)

The body accelerations are significantly stronger than those experienced in the previous case [Ref. Figure 37]. The tangential acceleration peaks at -4.5 g's while the normal accelerations peak at 0.82 g's. The total acceleration peaks at 4.57 g's at time 79.78 sec (1.33 min) [Figure 38]. Again, this corresponds exactly to the dynamic pressure peak of 2703.70 Pa [Figure 39].
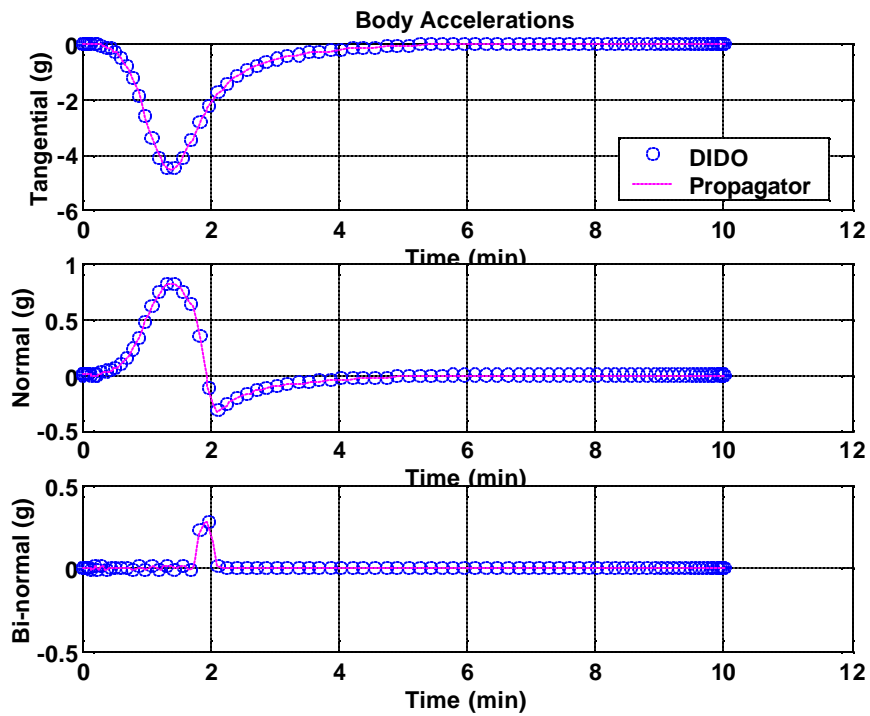
Figure 37: Body Accelerations (Excess Arrival V-inf)
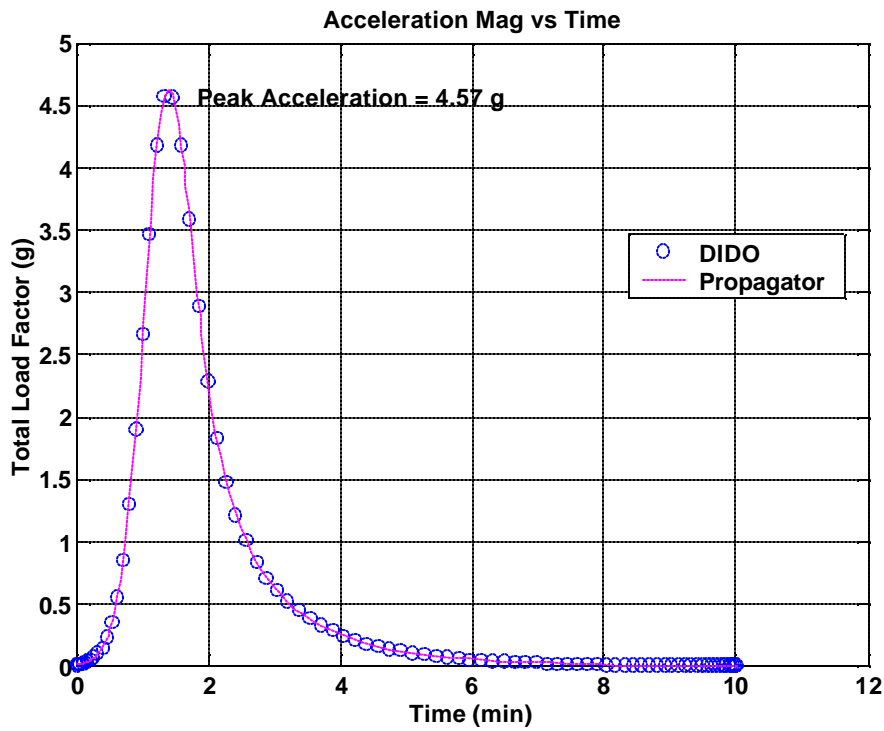
Figure 38: Total Acceleration (Excess Arrival V-inf)
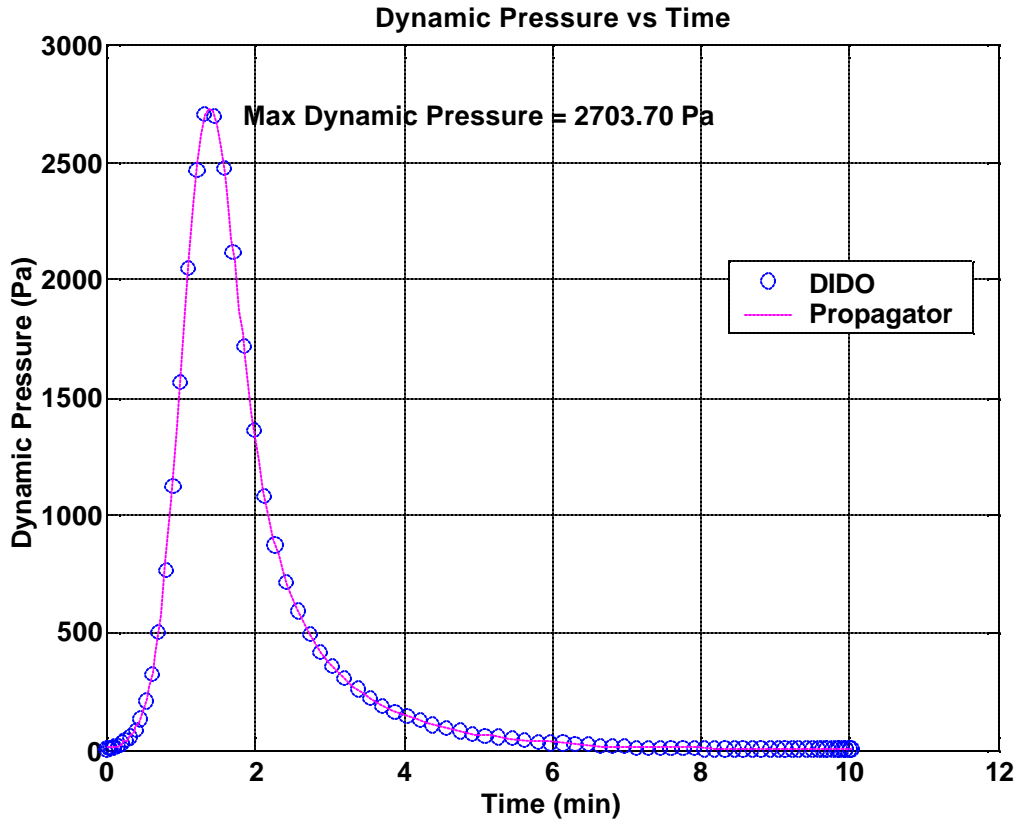
Figure 39: Dynamic Pressure (Excess Arrival V-inf)

The orbit parameters in the following figure are slightly more interesting than in the previous case. With this solution, the non-dimensional energy can be seen to begin well above zero, with capture occurring at 110.50 sec (1.84 min). The eccentricity decays from a hyperbolic 3.16 to a near-circular 0.04. Also the fact that apoapsis is undefined for parabolic trajectories is demonstrated as the apoapsis departs toward negative infinity to the left of the singularity before rapidly falling off from positive infinity immediately following the capture.

Orbit Paramters (Non-Dimensional)
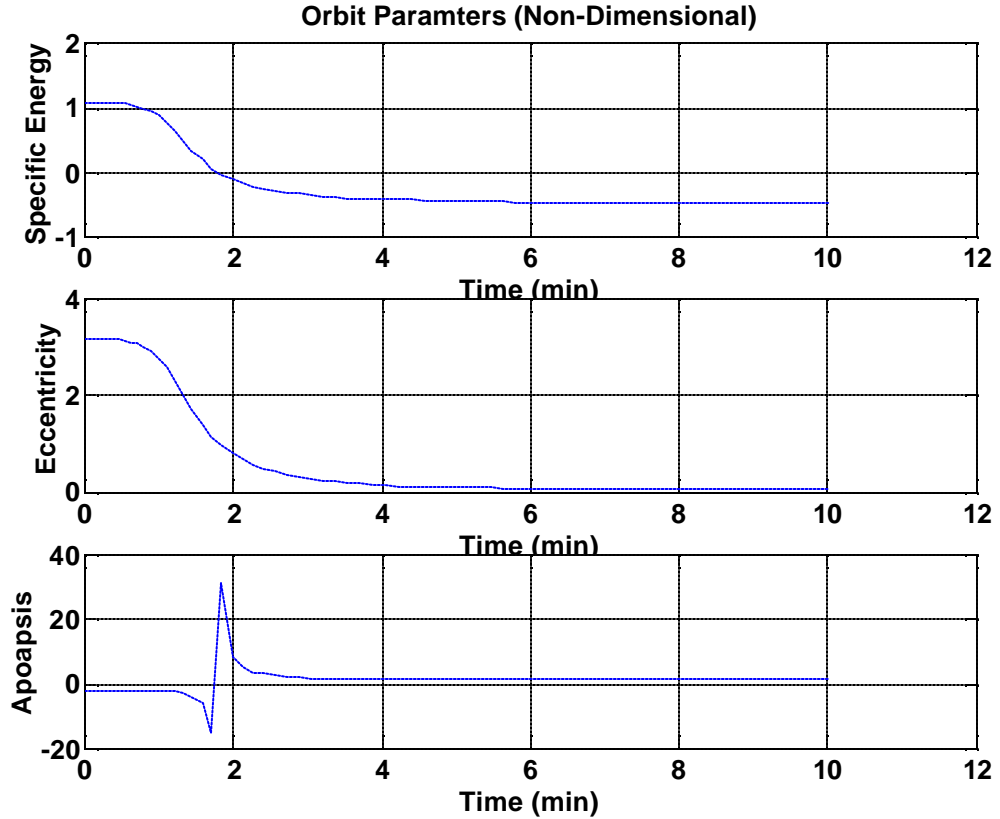
Figure 40: Selected Orbit Parameters (Excess Arrival V-inf)

D. MINIMUM AEROCAPTURE MASS AT NEPTUNE WITH EXCESS ARRIVAL V-INFINITY

The next case considered a minimum total aerocapture mass at Neptune with excess arrival V-infinity. The arrival V-infinity at Neptune was 9.42 km/s, significantly higher than that of Mars. A higher altitude of 1000 km was targeted for the final circular orbit and the atmospheric interface was defined as an altitude of 800 km.

The problem was solved by first solving the zero excess arrival trajectory for a non-rotating atmosphere. This solution was used to bootstrap the excess arrival velocity which was in-turn used to bootstrap the case of a rotating atmosphere. 90 nodes were deemed sufficient to provide an accurate, optimal solution. Table 8 gives the cost function breakdown for this solution. The total required aerocapture mass is 328 kg of which 48.4 kg is propellant mass and 279.5 kg is heat shield mass. While significantly

higher than the aerocapture mass required at Mars, the total capture mass is 200 kg less than the 528.7 kg of propellant required for a purely propulsive capture maneuver. Again, the accuracy of the heat shield mass predictions is limited to the model used, which assumes heat shield mass scales linearly with heat load.

Propellant mass	48.4 kg
Front-shield mass	279.5 kg
Total	328.0 kg

Table 8: Cost Function Breakdown (Neptune Excess V-inf)

Figure 41 shows the position history of the spacecraft during the atmospheric portion of the trajectory. Note the excellent agreement between DIDO solution (circles) and the propagated solution (solid line). The trajectory begins and ends at 800 km of altitude (the defined atmospheric interface). The total pass requires 22.64 minutes with a minimum altitude of 256.5 km occurring 4.16 minutes into the trajectory. Again the solver chooses an initial latitude of nearly 0 degrees (equatorial) with an easterly track.
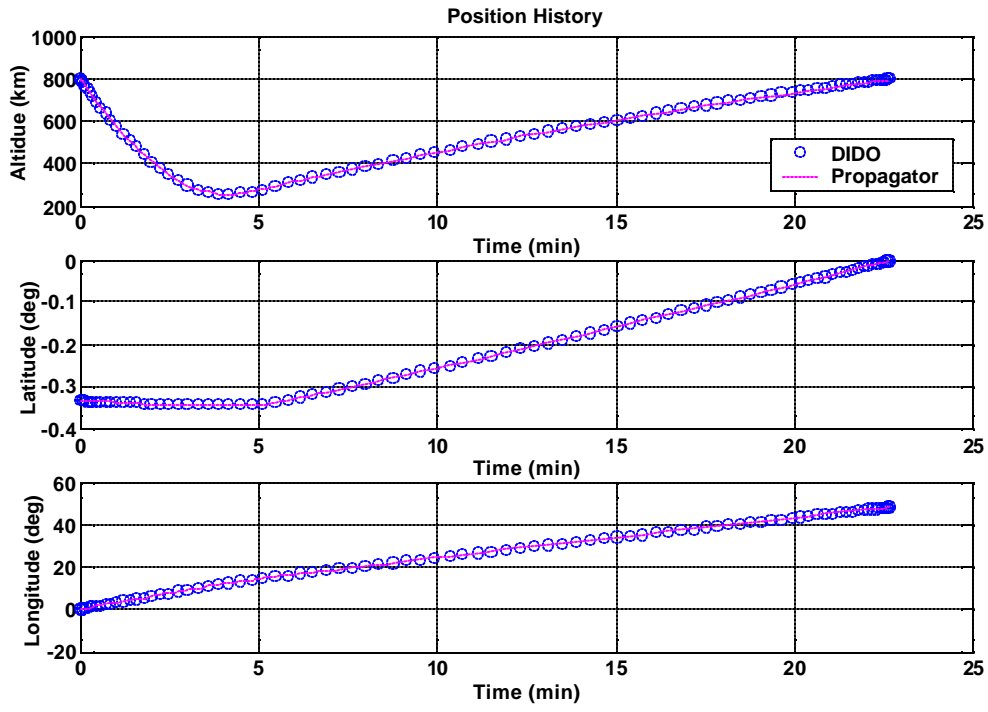
Figure 41: Position History (Neptune Excess V-inf)

Figure 42 shows the result of propagating the DIDO solution beyond the atmospheric limit of the solution. The propagated apoapsis of 976.12 km is within 23.9 km of the targeted 1000 km apoapsis altitude.
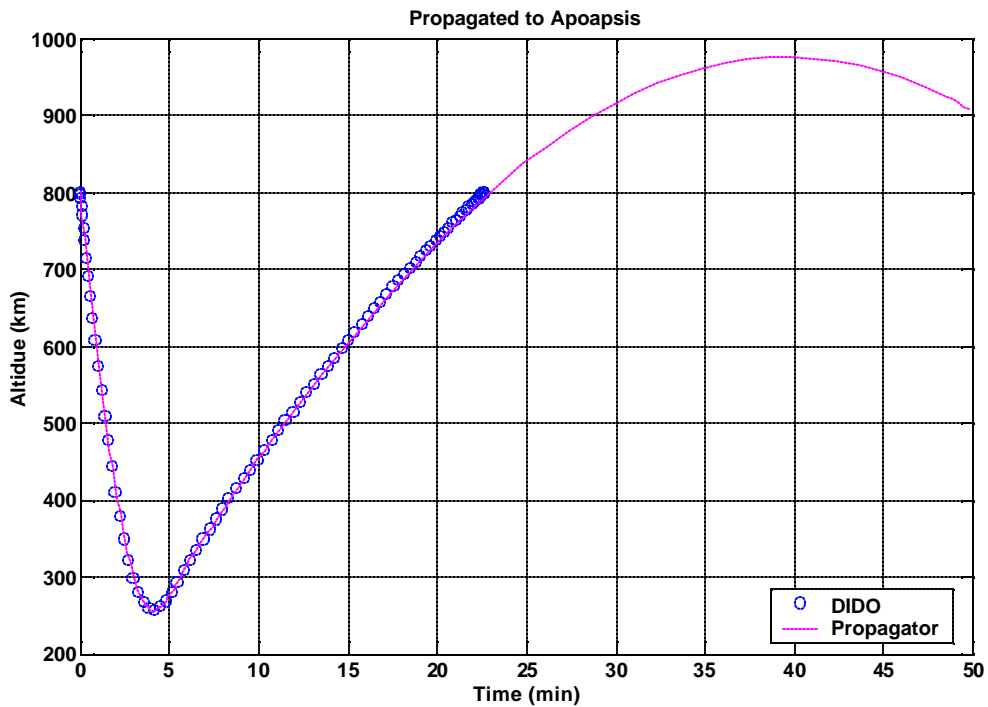
Figure 42: Propagated to Apoapsis (Neptune Excess V-inf)

Figure 43 gives the velocity state histories for the Neptune solution. The trajectory begins at a staggering inertial atmospheric entry speed of nearly 25000 m/s, a flight path angle of -9.35 degrees, and heading -0.1 degrees (due east). Inertial atmospheric exit occurs at 16144 m/s for an aerocapture delta-V of 8844 m/s.
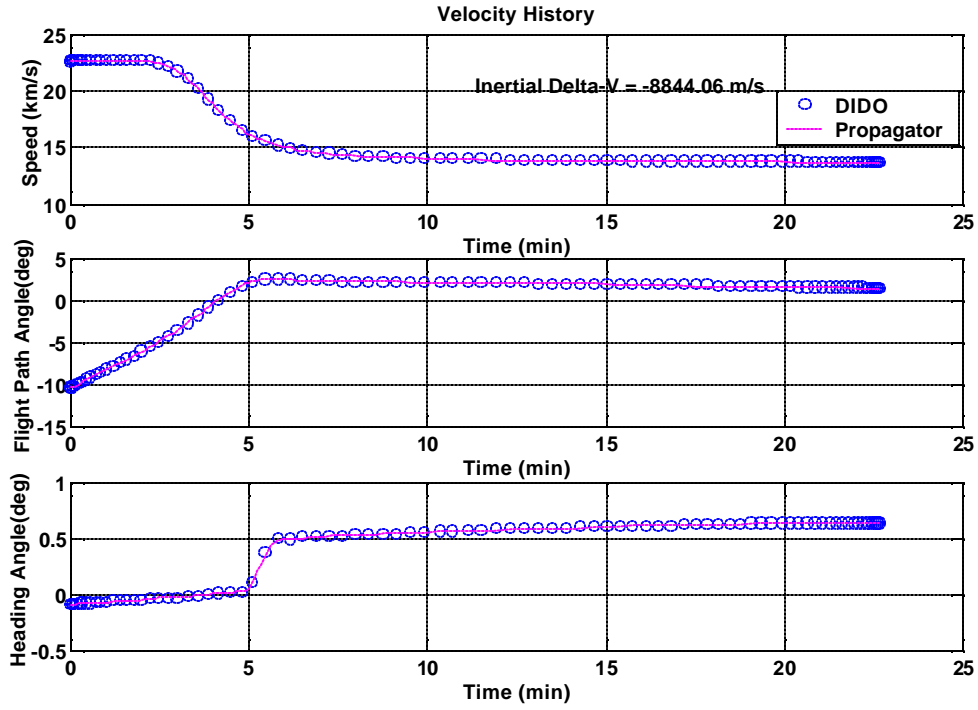
Figure 43: Velocity History (Neptune Excess V-inf)

The accuracy of the solution is presented in Table 9 which compares the DIDO and propagated terminal state values. Note that the "large" percentage errors in latitude and flight path angle are due to the small absolute value of the state.

State	DIDO value	Propagator value	Absolute Error	Percent Error
H_f	800 km	793.07 km	-6.9257 km	0.8733 %
$\boldsymbol{q}_f$	48.32 deg	48.31 deg	-0.0116 deg	0.0241 %
$\boldsymbol{f}_f$	-0.00 deg	-0.00 deg	-0.0007 deg	19.5726 %
v_f	13736.80 m/s	13732.23 m/s	-4.5689 m/s	0.0333 %
$\boldsymbol{y}_f$	0.64 deg	0.64 deg	-0.0007 deg	0.1067 %
$\boldsymbol{g}_f$	1.51 deg	1.46 deg	-0.0495 deg	3.3939 %

Table 9: Propagated Accuracy (Neptune Excess V-inf)

The control history for the trajectory is presented in Figure 44. The DIDO solution for the first minute and last nine minutes appears somewhat erratic. Investigating this further, the covectors associated with the controls over these time intervals are of very small value, indicating a lack of sensitivity of the performance index to the bank angle in these regions. This corresponds with the physical explanation of reduced control effectiveness in the thinner upper limits of the atmosphere. In the thicker, lower atmosphere, the bank angle trajectory assumes the previously seen, lift-up/lift-down "bang-bang" type control with the switch occurring at approximately 5.5 minutes, slightly after the minimum altitude point. The DIDO controls (circles) and the CMT derived controls (dots) are again in excellent agreement.
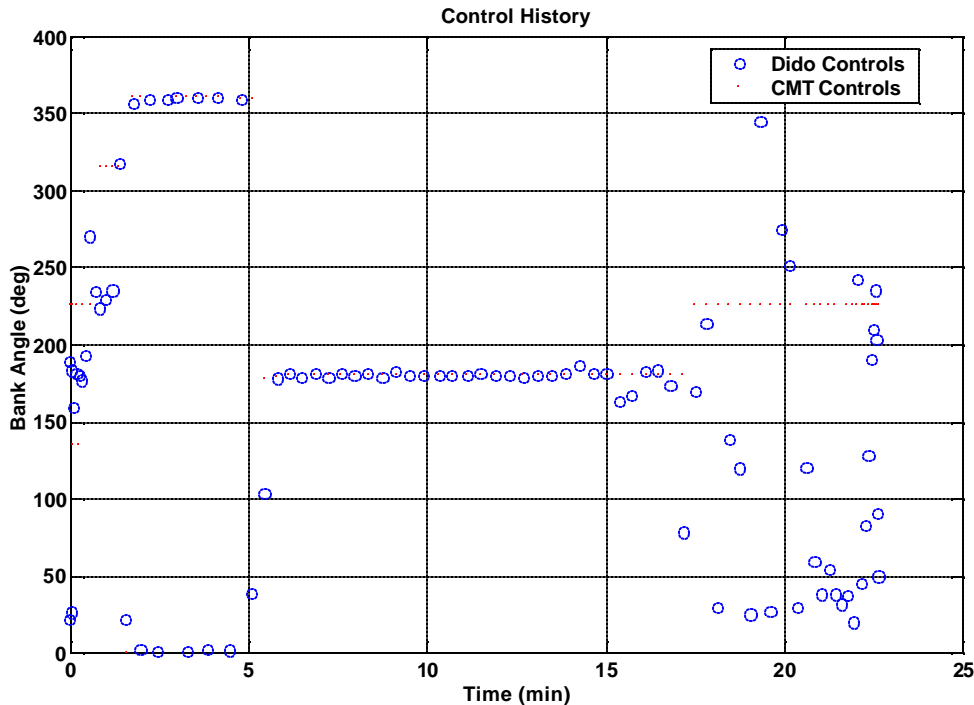
Figure 44: DIDO and CMT Control History (Neptune Excess V-inf)

The thicker atmosphere and significantly atmospheric velocities contribute to extreme stagnation point heating for this trajectory. The maximum heating rate of 264.59 W/cm^2 occurs just prior to the minimum altitude point (Figure 45). The long time

duration of the pass results in a total heat load of 55,904 J/cm^2 driving up the mass requirements for the TPS.
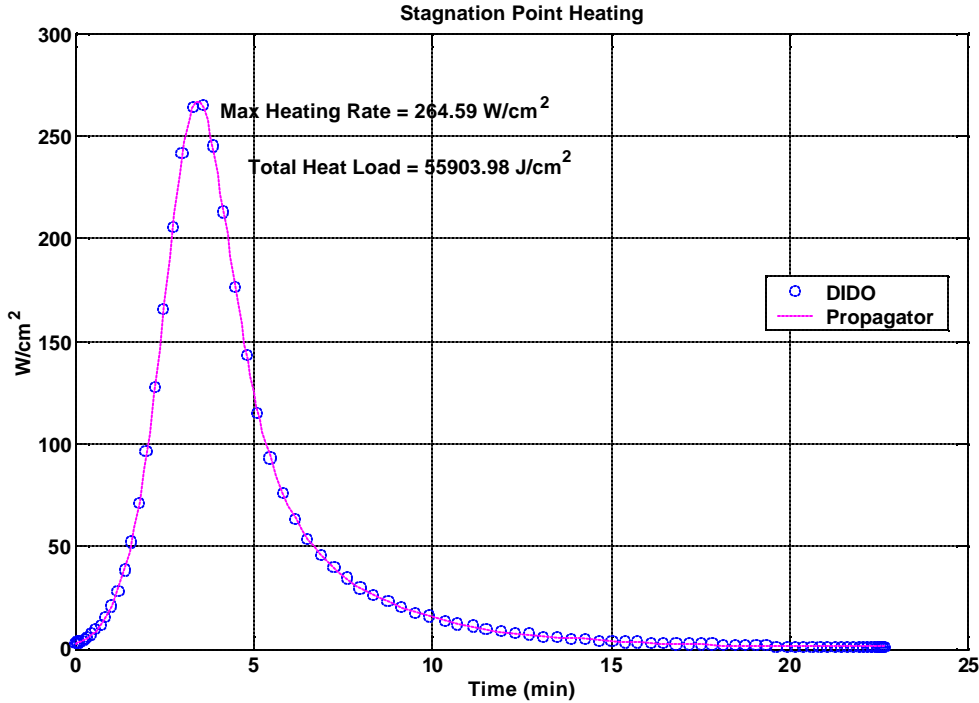
Figure 45: Stagnation Point Heating Rate (Neptune Excess V-inf)

Thermal protection is not the only engineering challenge presented by aerocapture at Neptune. The large aerodynamic forces lead to a peak total acceleration of 5.83 g (Figure 46). These high loads more akin to those experienced by fighter aircraft would require additional structural mass, further reducing available payload mass. This additional mass cost is not included in the modeling of this work.
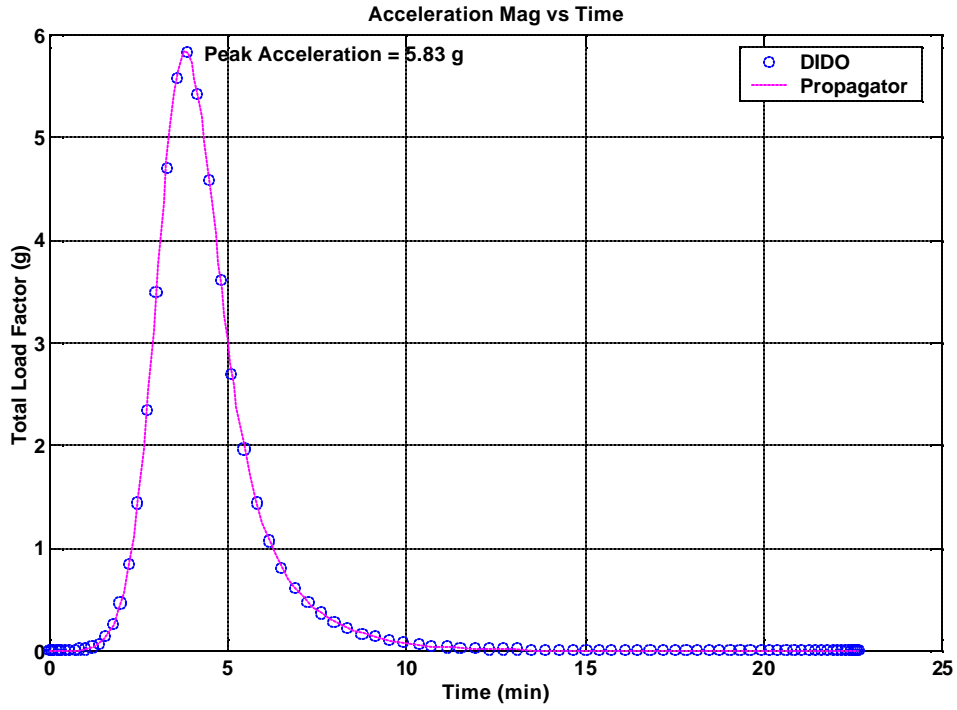
Figure 46: Total Acceleration (Neptune Excess V-inf)

E. MINIMUM AEROCAPTURE MASS AT MARS SUBJECT TO G-LIMITS

The previous results at Neptune demonstrate the potential for high g-loads during aerocapture maneuvers. Rather than increasing the structural integrity of the spacecraft to survive the loads, another option is to simply constrain the g-limit to some smaller, more manageable value. The following solution shows partial results for the problem described by VIII.C (Minimum total aerocapture mass at Mars with excess arrival velocity) except that the tangential acceleration has been limited to 3 g. A 120 node solution was obtained by bootstrapping from the unconstrained solution results. The trajectories were similar with the constrained trajectory being slightly shallower (initial flight path angle of -9.73 degrees compared with -10.47) and longer in duration (total pass time of 11.4 minutes compared with 10.02 minutes). The position state histories are presented in Figure 47. The minimum altitude varies by only 3.5 km but occurs almost 30 seconds later than the unconstrained case.
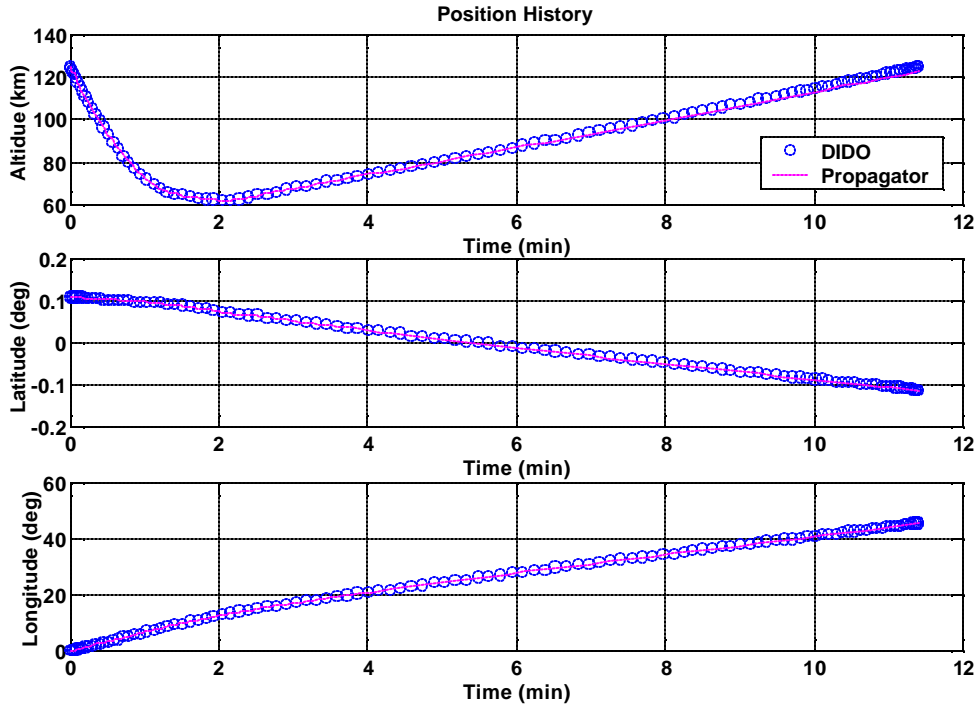
Figure 47: Position History (G-limited)

The velocity histories are nearly identical, with a delta-V within 4 m/s of the unconstrained case. The only notable differences are some slight perturbations in the flight path angle and heading angle between times 1.5 minutes and 2.5 minutes during which time the spacecraft performs a bank maneuver to reduce the loads on the vehicle. A plot of bank angle versus time (Figure 49) shows this maneuver in greater detail. As before, the bank angle begins lift-up until approximately 1.4 minutes into the trajectory. At that time the vehicle banks instantaneously to lift-down for 30 seconds before switching back to lift-up for another 20 seconds. Finally, the bank angle switches lift-down for the remainder of the trajectory.
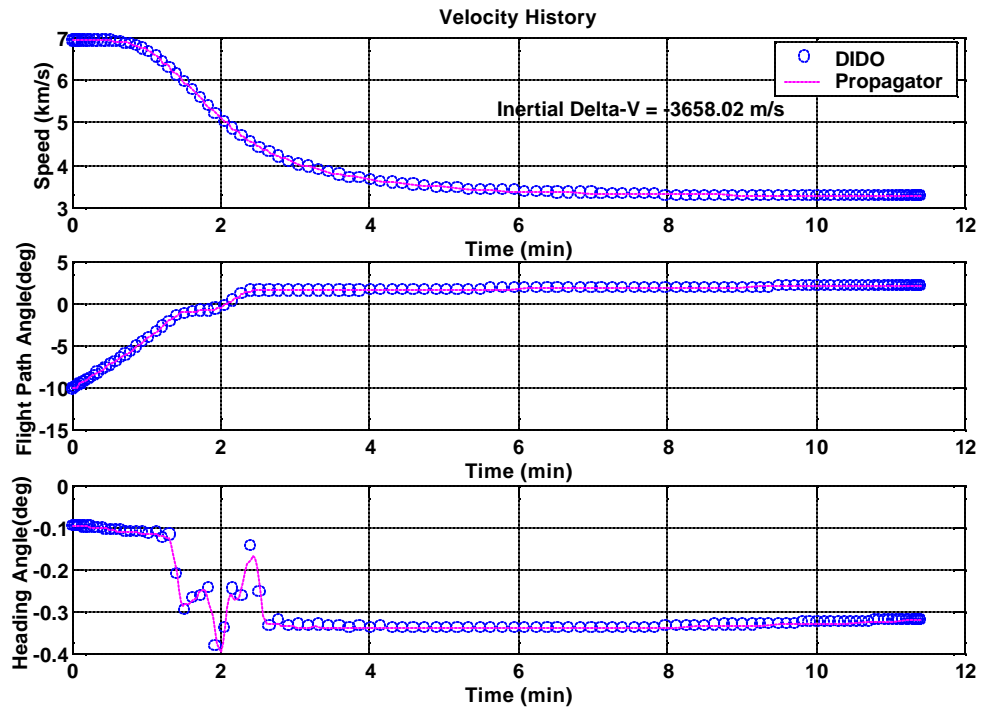
Figure 48: Velocity History (G-limited)
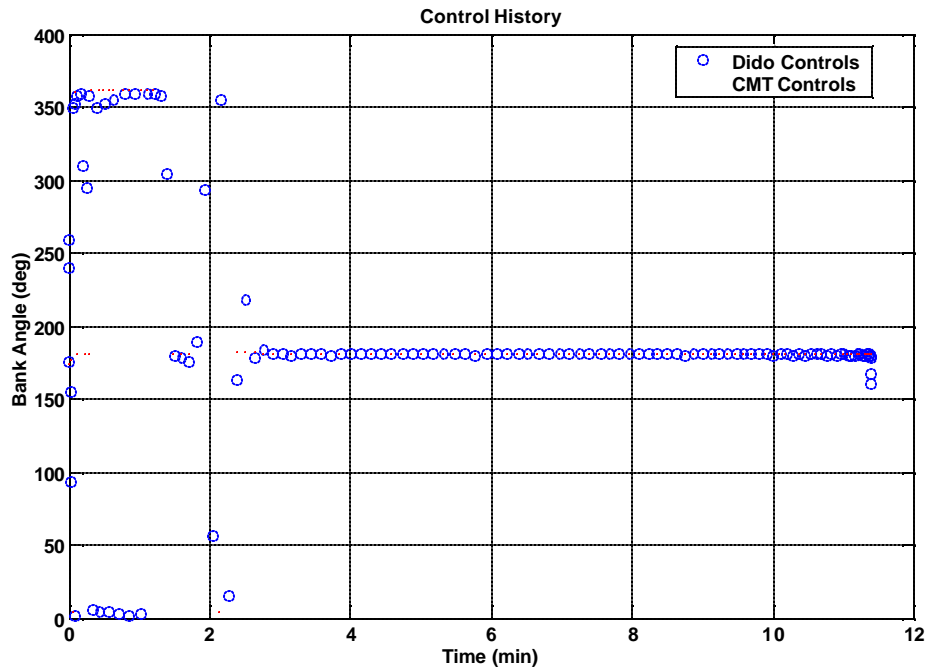
Figure 49: Control History (G-limited)

The first bank angle reversal is clearly reducing the tangential loads on the vehicle, as shown in the following plots of body accelerations. The first lift-down segment corresponds exactly to the time interval for which tangential acceleration is nearly constant at the constrained 3-g limit. This maneuver shows corresponding switches in the normal and bi-normal accelerations, coincident with the bank angle maneuvers. The second bank angle correction is more intriguing as it occurs after the tangential loads are decreasing in magnitude. This maneuver seems to be adding a slight increase in flight path angle to offset the period in which the flight path angle was relatively constant while lift-down (Figure 48).
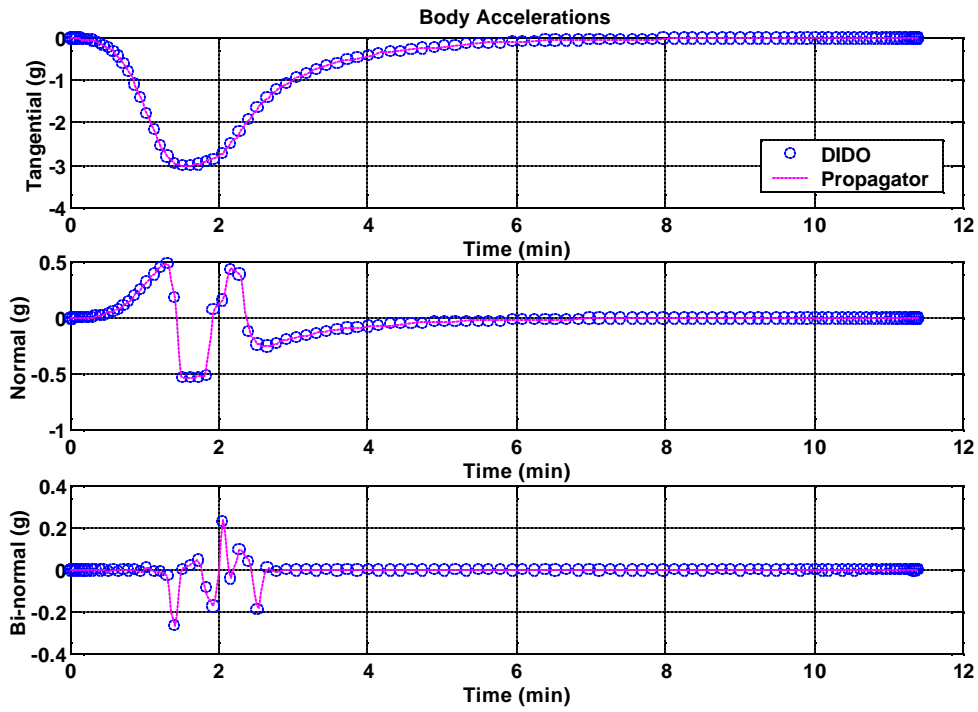
Figure 50: Acceleration Histories (G-limited)

The activation of the g-limit constraint can be further verified by examination of the covector associated with the constraint that is provided by DIDO. Figure 51 clearly shows that the constraint becomes active over the time period of the first bank reversal maneuver.
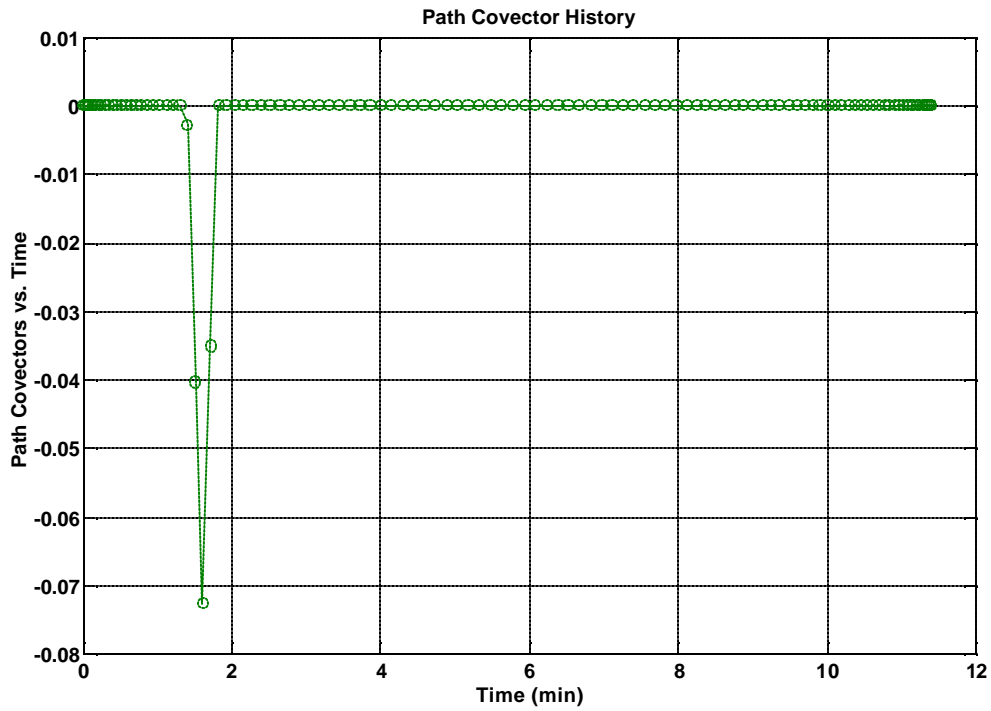
Figure 51: G-limit Constraint Covector History

The heating rate is less than the unconstrained case, peaking at 30.39 J/cm^2 (unconstrained value of 35.02 J/cm^2) but the total heat load is higher at 3814.6 W/cm^2 (unconstrained value of 3388.4 W/cm^2). This is consistent with shallower trajectories which tend to have longer but smaller heat pulses. This higher heat load contributes to a slightly higher performance index as total heat load is mapped to heat shield mass in our model. The total aerocapture mass increases from 28.75 kg to 30.2 kg (Table 10).

Propellant mass	11.13 kg
Front-shield mass	19.07 kg
Total	30.20 kg

Table 10: Cost Function Breakdown (G-limited)

F. MAXIMUM AEROCAPTURE CORRIDOR SUBJECT TO HEATING RATE CONSTRAINT

One of the difficulties with implementation of the aerocapture concept is the precision with which the spacecraft must guided to atmospheric interface. Aerocapture corridors are typically quite narrow, measuring only a couple degrees. The upper limit (that is to say shallowest angle) is normally defined as the shallowest initial flight path angle for which a <u>lift-down</u> bank angle profile will successfully meet the terminal conditions [Ref 9]. Similarly the lower limit is defined as the initial flight path angle for which a <u>lift-up</u> bank angle profile will meet the terminal conditions. Some preliminary work was done in investigating whether an optimal bank angle strategy can increase the aerocapture corridor width.

The maximum aerocapture corridor problem was solved by separately solving two related problems: maximum initial flight path angle and minimum initial flight path angle; respectively:

$$J = -g_0 \tag{183}$$

$$J = g_0 \tag{184}$$

The difference between the minimum and maximum initial flight path angle is then the maximum corridor width. In addition, both solutions were subject to heating-rate constraints. Note that it is important that the initial conditions for each problem be the same so that the resultant trajectories can be fairly compared. In fact, if this is not done, the optimal solution for the two problems differ in initial heading by 180 degrees! Instead the minimum initial flight path angle solution was generated first, and its initial condition was used to constrain the initial maximum flight path angle case. Moreover, with no constraint on the final orbit inclination, the optimal solutions placed the vehicle in an equatorial orbit - not very desirable from a scientific point of view. However, for the equatorial case, the corridor-defining optimal bank profiles were constant lift-up or constant lift-down as per the assumption in the definition. This turned out to <u>not</u> be the case for trajectories with final inclinations other than zero.

Additional solutions were generated with a constraint on the final orbit inclination of the vehicle. Recalling that upper-case Greek letters represent the components of the velocity vector resolved in the inertial frame, the inclination of the vehicle is related to the aircraft states by:

$$\cos i = \cos \Phi_f \cos \Psi_f \qquad (185)$$

The maximum heat rate was set at 50 W/cm^2 and the targeted inclination was arbitrarily chosen to be 70 degrees such that

$$\cos(70\text{deg}) \le \cos \Phi_f \cos \Psi_f \le \cos(70\text{deg}) \qquad (186)$$

Relevant parameters for the two trajectories that bound the maximum corridor are presented in Table 11.

	Minimum Initial FPA	Maximum Initial FPA
Initial Flight Path Angle	-10.83 deg	-8.66 deg
Initial V-infinity	5200 m/s	5200 m/s
Initial Latitude	17.6 deg	17.6 deg
Initial Heading	-73.4 deg	-73.46 deg
Delta-V	3743.5 m/s	3662.4 m/s
Total Pass Time	5.87 min	11.82 min
Minimum Altitude	56.32 km	66.52 km
Max Dynamic Pressure	3298.44 Pa	1354.9 Pa
Max Total Acceleration	5.57 g	2.29 g
Max Heating Rate	39.76 W/cm^2	27.67 W/cm^2
Heat Load	3138.83 J/c^2	4612.22 J/cm^2
Front-shield Mass	15.69 kg	23.06 kg
Post-Aerocapture Propellant	26.41 kg	11.91 kg
Total Aerocapture Mass	42.1 kg	34.97 kg

Table 11: Max Corridor Boundary Comparison

Figure 52 is a plot of the position state histories for the two trajectories (circles represent the maximum flight path angle entry while the plus symbols represent the minimum flight path angle entry). The trajectories begin at atmospheric interface at the optimal latitude of 17.6 degrees.   The minimum flight path angle trajectory is steep (-10.83 deg), with only 5.87 minutes of total pass time compared with 11.82 minutes for the shallow maximum flight path angle case (-8.66 deg). The steeper trajectory naturally penetrates deeper into the atmosphere to an altitude of 56.32 km as compared with 66.52 for the shallower trajectory.
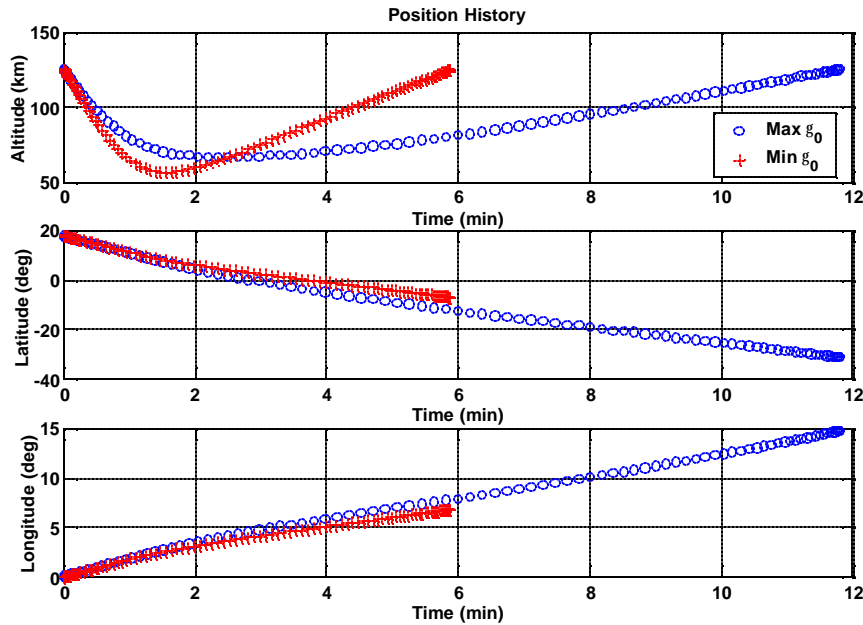
Figure 52: Max Corridor Position Histories

The velocity histories are given in Figure 53. The total delta-V for the two trajectories are nearly equal at about 3703 m/s +/- 40 m/s.
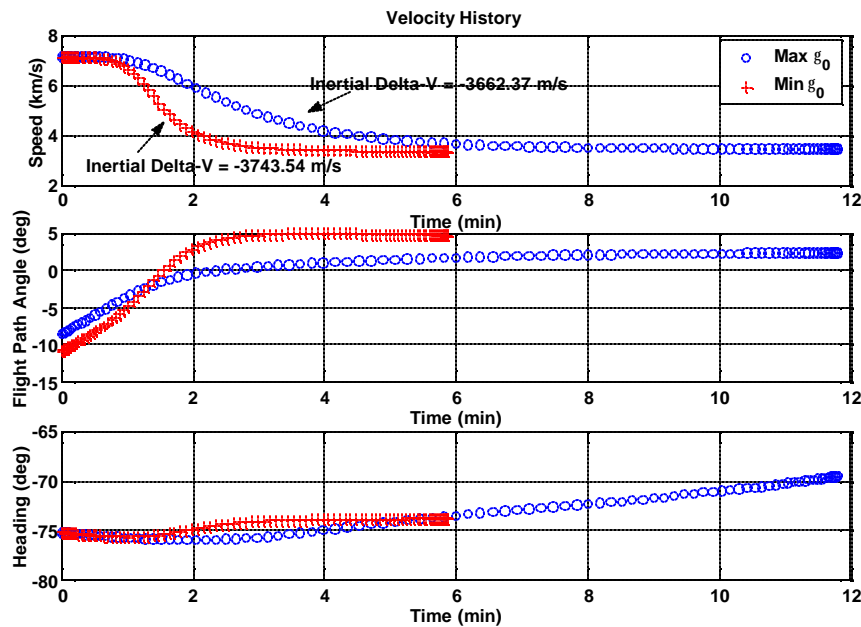
Figure 53: Max Corridor Velocity Histories

The control histories for the trajectories are given in the following figure. CMT control histories were plotted in lieu of the DIDO solutions as they better demonstrated the arctangent characteristic of the bank angle schedule. Clearly the optimal bank angle profiles are not simply lift-up or lift-down as was the case for equatorial target orbits. The steep flight path begins lift-up and modulates to approximately 60 degrees during the ascent. In a like manner, the shallower entry begins lift-down and modulates to approximately 94 deg during the ascent. In neither case does the lift vector cross the horizontal plane; instead the lift vector seems to be used to control depth of penetration prior to the minimum altitude before switching to control heading (and hence target inclination) for the ascent.
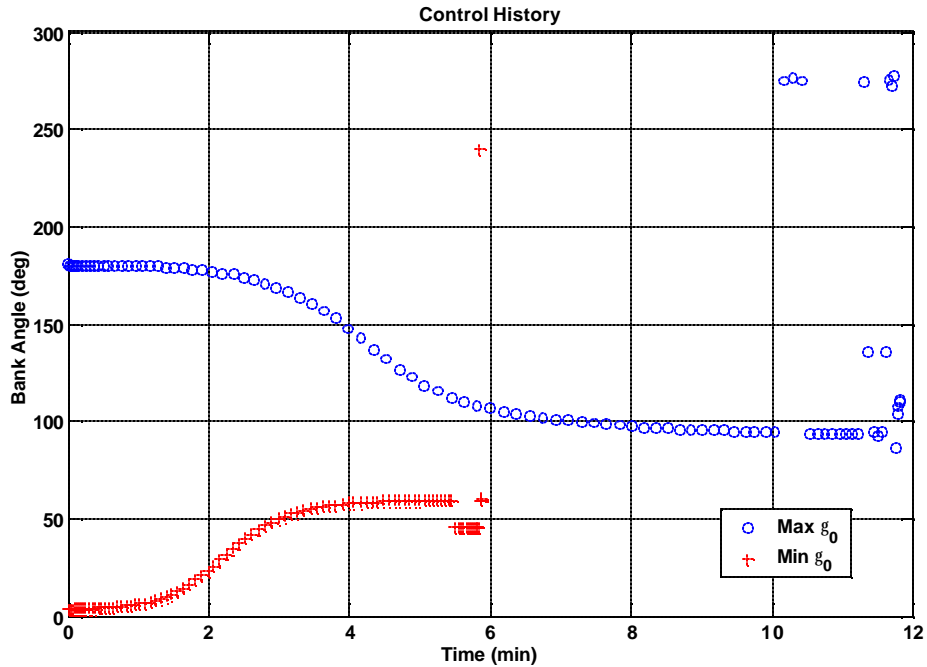
Figure 54: Max Corridor Control Histories

As expected, the peak heating rate for the steep entry is significantly higher than the shallow entry (39.76 W/cm^2 as compared to 27.67 W/cm^2) although the shallower trajectory has the higher heat load (4,612 J/cm^2 compared with 3,138 J/cm^2) (Figure 55). Note that the peak heating rate was below the constraint value of 50 W/cm^2
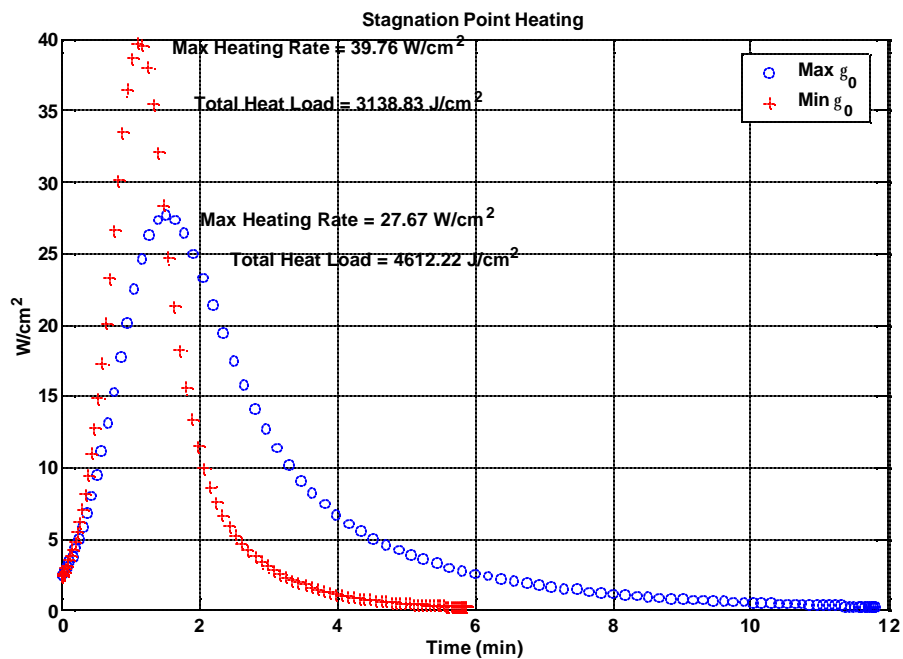
Figure 55: Max Corridor Heating Rates
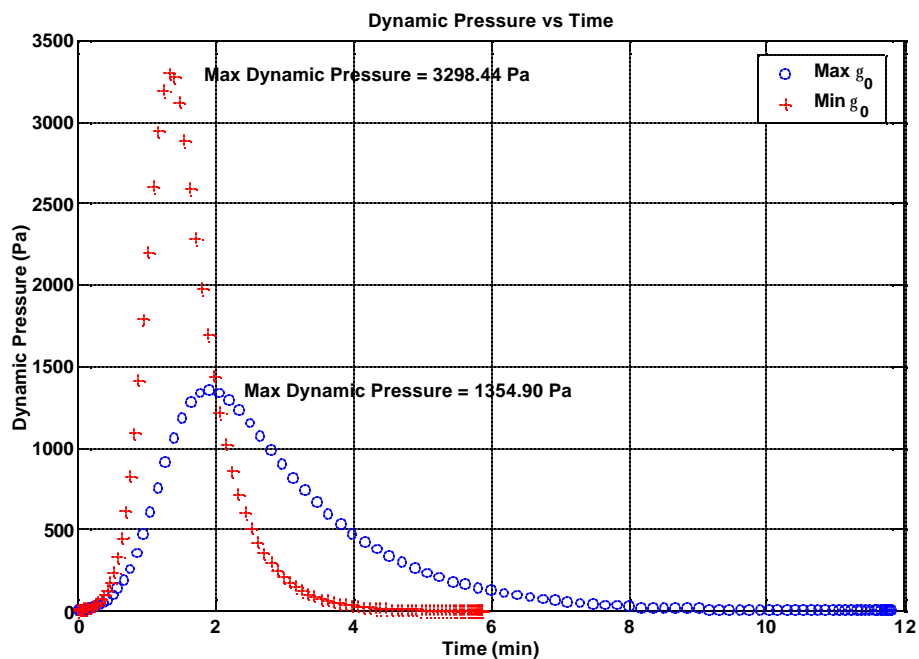
Figure 56: Max Corridor Dynamic Pressures

105

The peak dynamic pressure (Figure 56) of the steep trajectory is more than double that of the shallow trajectory (3,298 Pa compared with 1,355 Pa) which leads to a similar disparity in peak total accelerations (Figure 57). The steep entry encounters a crushing 5.57 g peak acceleration whereas the shallow entry peaks at a more manageable 2.29 g. Figure 58 resolves the aerodynamic accelerations into flight-path related components.
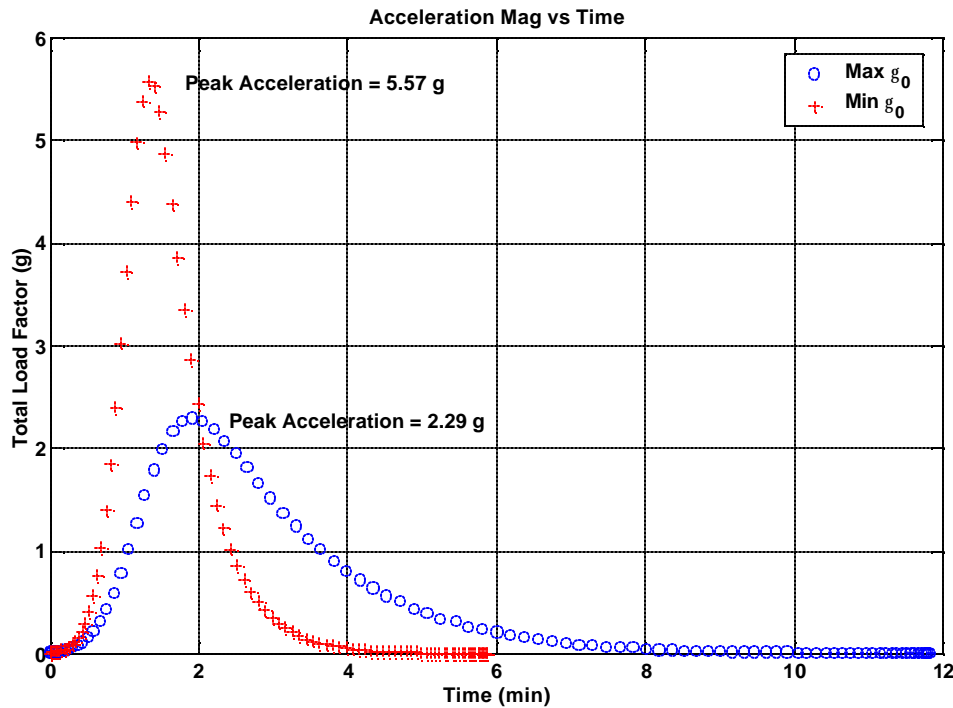
Figure 57: Max Corridor Total Accelerations
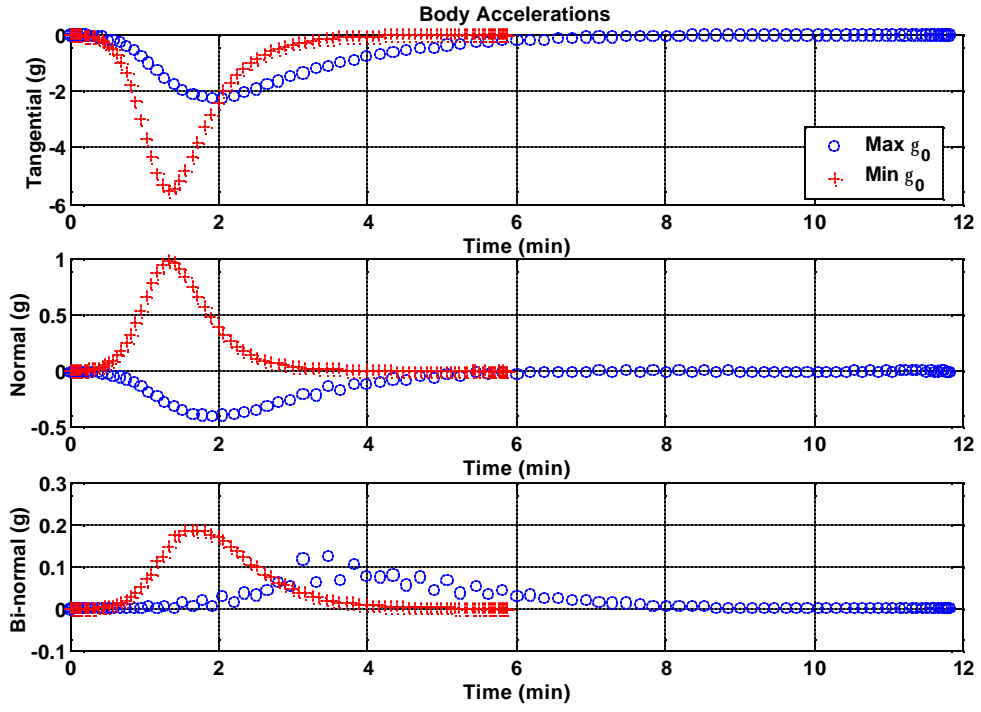
Figure 58: Max Corridor Acceleration Components

The significant differences in characteristics of the trajectories which define the boundaries of the maximum aerocapture corridor illustrate the difficulties imposed upon the design team. To utilize the entire available corridor, the vehicle's structure must be sized to the more dynamic, steep boundary trajectory while the TPS mass must be sized for the larger heat loads of the shallow entry. Additionally, the TPS material selection will be dependent on the maximum heating rate of the steep trajectory.

THIS PAGE INTENTIONALLY LEFT BLANK

IX. FORMULATING THE COMBINED LOW THRUST AND AEROCAPTURE PROBLEM

Previous chapters detail the problem formulation for both low thrust and aerocapture trajectories taken separately. The attention is now turned to the problem of solving for the low thrust trajectory that terminates with an aerocapture maneuver. One approach for generating *feasible* integrated trajectories is to optimize the low thrust trajectory using its final state to derive the initial state for an optimal aerocapture pass. However, this formulation is <u>not</u> optimizing the problem from end to end. To find the true integrated optimal solution, we must <u>simultaneously</u> solve both trajectories.

A. JUNCTION CONDITIONS

Recall that a direct, discreet solution method reduces an optimal control problem to a series of dynamic constraints sampled at various nodes (times). Thus, the state history for a low thrust problem can be expressed as a matrix such as

$$
\begin{bmatrix}
r(t_0) & r(t_1) & \cdots & r(t_j) \\
q(t_0) & q(t_1) & \cdots & q(t_j) \\
v_r(t_0) & v_r(t_1) & \cdots & v_r(t_j) \\
v_t(t_0) & v_t(t_1) & \cdots & v_t(t_j) \\
m(t_0) & m(t_1) & \cdots & m(t_j)
\end{bmatrix}
\tag{187}
$$

Where the columns represent the values of the states at each node time and were j is the index corresponding to the final node of the low thrust solution. Similarly for aerocapture

$$
\begin{bmatrix}
r(t_0) & r(t_1) & \cdots & r(t_k) \\
q(t_0) & q(t_1) & \cdots & q(t_k) \\
f(t_0) & f(t_1) & \cdots & f(t_k) \\
v(t_0) & v(t_1) & \cdots & v(t_k) \\
y(t_0) & y(t_1) & \cdots & y(t_k) \\
g(t_0) & g(t_1) & \cdots & g(t_k)
\end{bmatrix}
\tag{188}
$$

where k represents the final node index of the trajectory.

If these two state history matrices were of the same dimension, they could be augmented forming a combined state history for the entire problem. However, note that the low thrust state history matrix has one less row (state) than the aerocapture matrix. This can be resolved by simply adding a "dummy variable" to the last row of the matrix.

$$
\begin{bmatrix}
r(t_0) & r(t_1) & \cdots & r(t_j) \\
q(t_0) & q(t_1) & \cdots & q(t_j) \\
v_r(t_0) & v_r(t_1) & \cdots & v_r(t_j) \\
v_t(t_0) & v_t(t_1) & \cdots & v_t(t_j) \\
m(t_0) & m(t_1) & \cdots & m(t_j) \\
X & X & \cdots & X
\end{bmatrix}
\tag{189}
$$

Our combined state history matrix now takes the desired form of a 6 by $(j+k)$ matrix with the final column of the low thrust trajectory occurring at index j and the first column of the aerocapture trajectory beginning with column $j+1$.

$$
\begin{bmatrix}
r(t_0) & r(t_1) & \cdots & r(t_j) & r(t_{j+1}) & \cdots & r(t_{j+k}) \\
q(t_0) & q(t_1) & \cdots & q(t_j) & q(t_{j+1}) & \cdots & q(t_{j+k}) \\
v_r(t_0) & v_r(t_1) & \cdots & v_r(t_j) & f(t_{j+1}) & \cdots & f(t_{j+k}) \\
v_t(t_0) & v_t(t_1) & \cdots & v_t(t_j) & v(t_{j+1}) & \cdots & v(t_{j+k}) \\
m(t_0) & m(t_1) & \cdots & m(t_j) & y(t_{j+1}) & \cdots & y(t_{j+k}) \\
X & X & \cdots & X & g(t_{j+1}) & \cdots & g(t_{j+k})
\end{bmatrix}
\tag{190}
$$

However, we now must somehow match the physical meaning of the end of the low thrust trajectory with that of the beginning of the aerocapture trajectory. As formulated, the states take on very different meanings in the two portions of the problem. For example, the 5th row of the low thrust portion represents the vehicle's mass while in the aerocapture portion that same row represents heading angle. Thus we need some junction conditions to relate the variables on the two sides of the problem.

110

First, recall from previous chapters that the initial final radius of the low thrust portion and the initial radius of the aerocapture problem are fixed. That is

$$r\left(t_{j}\right)=r_{planet} \tag{191}$$

$$r\left(t_{j+1}\right)=r_{atmos\ limit} \tag{192}$$

Final velocities for the low thrust portion are left unconstrained to allow for non-rendezvous (excess arrival V-infinity) trajectories to be generated. The vehicle mass at the end of the low thrust portion remains subject to the physical limitation that

$$m_{dry}\le m\left(t_{j}\right)\le m\left(t_{0}\right) \tag{193}$$

Although mass is not a state for the aerocapture segment, its value is needed for the dynamics calculations. Assuming that there is no post low thrust staging this yields

$$m_{aerocapture}=m\left(t_{j}\right) \tag{194}$$

Since vehicle mass at arrival is on the same order as the initial vehicle mass at launch, there conveniently is no need rescale the problem as the normalizing units of mass may be chosen to be the same for both trajectory segments.

Recall that for convenience the initial longitude of the aerocapture trajectory was set to zero so

$$q\left(t_{j+1}\right)=0 \tag{195}$$

Similarly the initial velocity states of the aerocapture problem can be related in some manner to the terminal conditions of the low thrust problem.

$$v_{j+1}=f\left(v_{r}\left(t_{j}\right),v_{t}\left(t_{j}\right),r\left(t_{j+1}\right),f\left(t_{j+1}\right),g\left(t_{j+1}\right)\right) \tag{196}$$

$$y_{j+1}=f\left(v_{r}\left(t_{j}\right),v_{t}\left(t_{j}\right),r\left(t_{j+1}\right),f\left(t_{j+1}\right),g\left(t_{j+1}\right)\right) \tag{197}$$

$$g_{j+1}=f\left(v_{r}\left(t_{j}\right),v_{t}\left(t_{j}\right),r\left(t_{j+1}\right),f\left(t_{j+1}\right),g\left(t_{j+1}\right)\right) \tag{198}$$

111

To see exactly how these are related, the V-infinity of arrival for the aerocapture problem must be found. The heliocentric inertial velocity of the vehicle is give by the vector equation

$$\left\{\vec{V}_{vehicle}\right\}_{sun} = \left\{\vec{V}_{planet}\right\}_{sun} + \left\{\vec{V}_{vehicle}\right\}_{planet} \tag{199}$$

which can be rearranged to find the inertial velocity of the vehicle relative to the planer

$$\left\{\vec{V}_{vehicle}\right\}_{planet} = \left\{\vec{V}_{vehicle}\right\}_{sun} - \left\{\vec{V}_{planet}\right\}_{sun} \tag{200}$$

With respect to the variables used in the low thrust portion, the velocity vector of the vehicle with respect to the sun is

$$\left\{\vec{V}_{vehicle}\right\}_{sun} = \begin{bmatrix} v_r \\ v_t \end{bmatrix} \tag{201}$$

and the circular velocity of the planet is given by

$$\left\{\vec{V}_{planet}\right\}_{sun} = \begin{bmatrix} 0 \\ \sqrt{\dfrac{m_{sun}}{r_{planet}}} \end{bmatrix} \tag{202}$$

Thus the velocity of the vehicle relative to the planet can be expressed as

$$\left\{\vec{V}_{vehicle}\right\}_{planet} = \begin{bmatrix} v_r \\ v_t - \sqrt{\dfrac{m_{sun}}{r_{planet}}} \end{bmatrix} \tag{203}$$

The magnitude of this vector is

$$\left\|\left\{\vec{V}_{vehicle}\right\}_{planet}\right\| = V_{\infty_{arrival}} = \sqrt{v_r^{\,2} + \left(v_t^{\,2} - \sqrt{\dfrac{m_{sun}}{r_{planet}}}\right)} \tag{204}$$

The square root term leads to possibility of a singularity so it is more convenient to use the square of the V-infinity at arrival given as

$$\left\|V_{\infty_{arrival}}\right\|^2 = v_r\left(t_j\right)^2 + \left(v_t\left(t_j\right)^2 - \sqrt{\dfrac{m_{sun}}{r\left(t_j\right)}}\right) \tag{205}$$

112

At this point, the inertial arrival velocity magnitude in the planet frame at the beginning of the aerocapture trajectory is known. Given the small size of the target planet relative to the scale of the heliocentric trajectory, small course corrections far from the target planet allow for any point on the B-plane to be targeted (the B-plane is a reference plane used for interplanetary targeting). This means that the initial latitude, longitude, velocity, heading and flight path angle sates for the aerocapture problem is are essentially free, provided they all take values that are consistent with the arrival V-infinity.

Using vis-viva, the magnitude of the velocity vector at the atmospheric interface (where we begin the aerocapture trajectory) is related to the arrival V-infinity.

$$\frac{V_{\infty_{arrival}}^2 - V_{atm-in}^2}{2} + \frac{m}{r_{atm}} = 0 \tag{206}$$

Again referring to Appendix A, the velocity components in a rotating REN frame may be related to the arrival V-infinity, thus we can now relate the V-infinity as calculated from the final states of the low thrust trajectory to the initial states of the aerocapture trajectory as

$$\left\| V_{\infty_{arrival}}\left(t_j\right) \right\|^2 = v\left(t_{j+1}\right)^2 + r\left(t_{j+1}\right)^2 \Omega^2 \cos^2 f\left(t_{j+1}\right) \cdots \\ + 2r\left(t_{j+1}\right) v\left(t_{j+1}\right) \Omega \cos f\left(t_{j+1}\right) \cos y\left(t_{j+1}\right) cos g\left(t_{j+1}\right) \tag{207}$$

Substituting Eqn. (205) into the above equation yields the following important junction condition

$$v_r\left(t_j\right)^2 + \left(v_t\left(t_j\right)^2 - \sqrt{\frac{m_{sun}}{r\left(t_j\right)}}\right) = v\left(t_{j+1}\right)^2 + r\left(t_{j+1}\right)^2 \Omega^2 \cos^2 f\left(t_{j+1}\right) \cdots \\ + 2r\left(t_{j+1}\right) v\left(t_{j+1}\right) \Omega \cos f\left(t_{j+1}\right) \cos y\left(t_{j+1}\right) cos g\left(t_{j+1}\right) \tag{208}$$

However, recall that not only were the states different between the two formulations, but they were scaled markedly different as well. This can be resolved through the addition of a constant conversion factor

113

$$\left[\overline{v}_r\left(t_j\right)^2+\left(\overline{v}_t\left(t_j\right)^2-\sqrt{\frac{\boldsymbol{m}_{sun}}{\overline{r}\left(t_j\right)}}\right)\right]\left(\frac{U_{dist\_lowthrust}}{U_{dist\_aerocapture}}\right)^2=\overline{v}\left(t_{j+1}\right)^2+\overline{r}\left(t_{j+1}\right)^2\overline{\Omega}^2\cos^2\overline{\boldsymbol{f}}\left(t_{j+1}\right)\cdots$$
$$+2\overline{r}\left(t_{j+1}\right)\overline{v}\left(t_{j+1}\right)\overline{\Omega}\cos\overline{\boldsymbol{f}}\left(t_{j+1}\right)\cos\overline{\boldsymbol{y}}\left(t_{j+1}\right)\cos\overline{\boldsymbol{g}}\left(t_{j+1}\right)$$
(209)

Eqns. (191)-(193), (195), and (209) complete the junction conditions for the combined problem.

B.   COST FUNCTIONS

1.   Minimum Total Propellant

A relatively simple to implement performance index for the combined problem is to minimize the total propellant required for the mission. This can be accomplished despite the propellants being of different types with different I_{sp}. This combined propellant cost can be expressed in Mayer form as

$$J=-\left(m_{proplowthrust}+m_{prop\,circ}\right)$$
(210)

where $m_{proplowthrust}$ is the propellant mass consumed during the low thrust portion of the trajectory as given by

$$m_{proplowthrust}=m\left(t_j\right)-m\left(t_0\right)$$
(211)

and $m_{propcirc}$ is the mass of propellant needed to circularize the post-aerocapture transfer orbit.

2.   Maximum Scientific Mass

The total maximum scientific mass at arrival can found by taking the total propellant cost above and adding to it the estimated mass of the heat shield. Using the same mapping between heat load and front-shield mass used in chapters VII and VIII this can be expressed as a Bolza cost as follows

$$J = -\left(m_0 - m_{proplowthrust} - m_{propcirc}\right) + k \int_{t_{j+1}}^{t_k} \dot{q} \; d\boldsymbol{t} \tag{212}$$

THIS PAGE INTENTIONALLY LEFT BLANK

X. SOLUTIONS TO THE COMBINED LOW THRUST AND AEROCAPTURE PROBLEM

A. MINIMUM TOTAL FUEL SOLUTION

The minimum total fuel solution was obtained using 40 nodes of resolution for each segment of the trajectory. Obtaining feasible trajectories proved rather difficult. Increasing the thrust capacity of the low thrust vehicle helped to obtain solutions at the expense of realism. In addition, the rotation of the target planet was set to zero to simplify the solution and reduce computation time. This was accomplished by simply assuming that the vehicle employed 10 NSTAR engines. As show in Figure 59 (where again the circles are the DIDO solution and the solid line is the propagated trajectory) the trajectory begins with zero C_3 and a 700 kg vehicle and arrives at 1.52 AU 291 days after launch. In the process, 61.58 kg of propellant are consumed for an arrival mass at Mars of 638.42 kg. The close agreement between the DIDO solution and the propagated solution verify the feasibility of the solution.
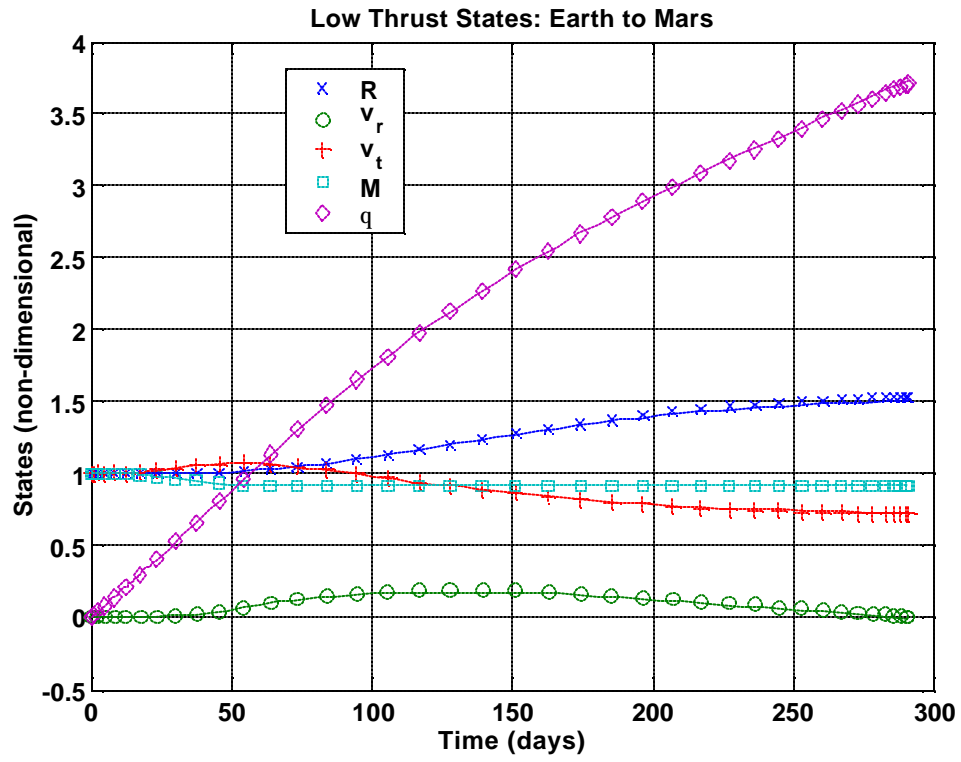
Figure 59: Low Thrust State Histories (Min Total Fuel)

The heliocentric trajectory is shown in Figure 60. An initial burn of approximately 48 days increases the semi-major axis of the transfer orbit until the aphelion intersects Mars's orbit. The small deviations between the DIDO and propagated solutions are more visible in this presentation.
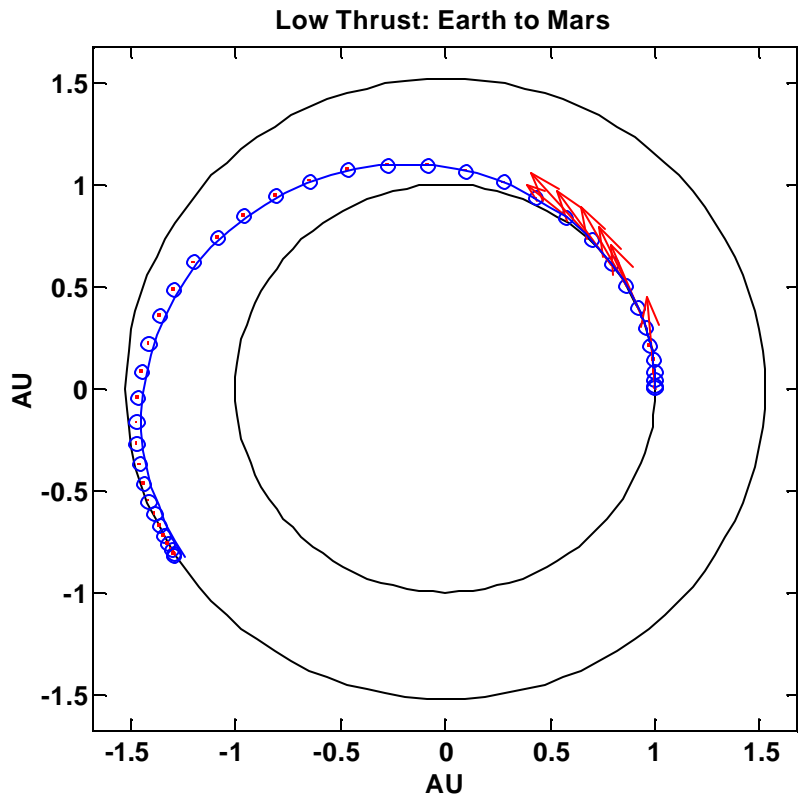
Figure 60: Heliocentric Low Thrust Trajectory (Min Total Fuel)

The vehicle arrives at Mars with an inertial arrival V-infinity of 2626.2 m/s and a relatively shallow flight path angle of -7.62 degrees. Note that this is a relatively shallow flight path angle but the correspondingly small arrival V-infinity ensures that the vehicle will not "skip" off the atmosphere. Figure 61 and Figure 62 depict the vehicles states for the aerocapture portion of the trajectory. A minimum altitude of 70 km is reached 3 minutes into the 13.65 minute trajectory. The pass yields a total delta-V of 2078 m/s. Again the DIDO solution and the propagated solution are in excellent agreement. The transfer orbit is highly circular with an eccentricity of only 0.03. This contributes to the low propellant mass required to circularize of only 12.1 kg.
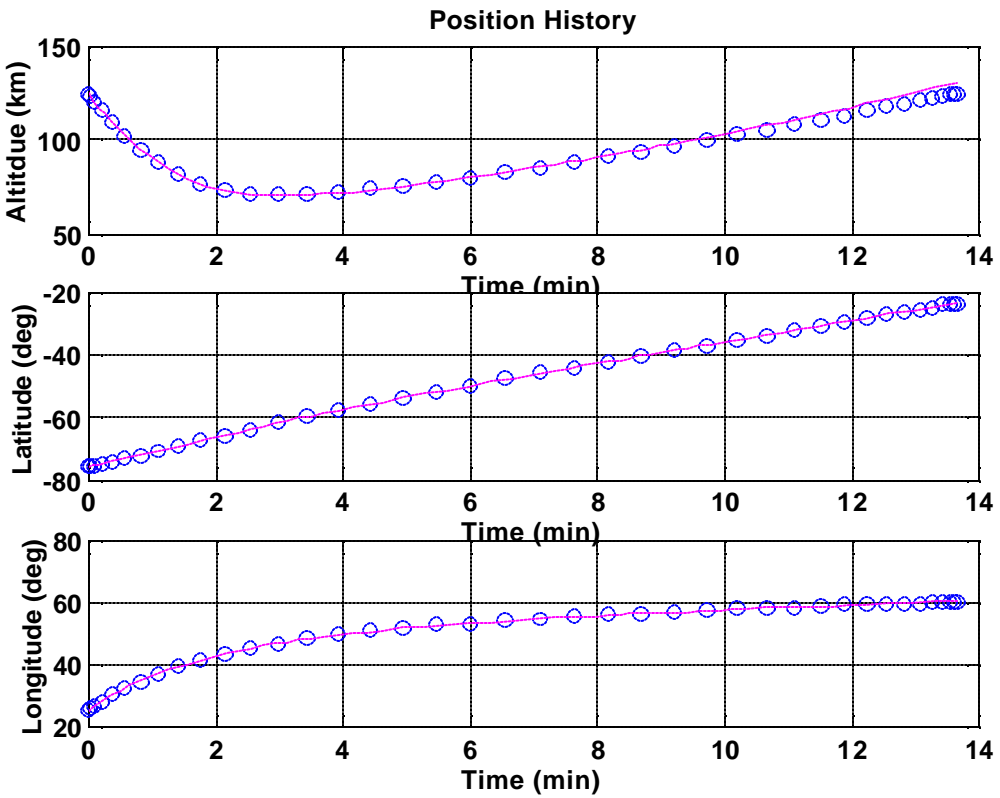
Figure 61: Aerocapture Position States (Min Total Fuel)
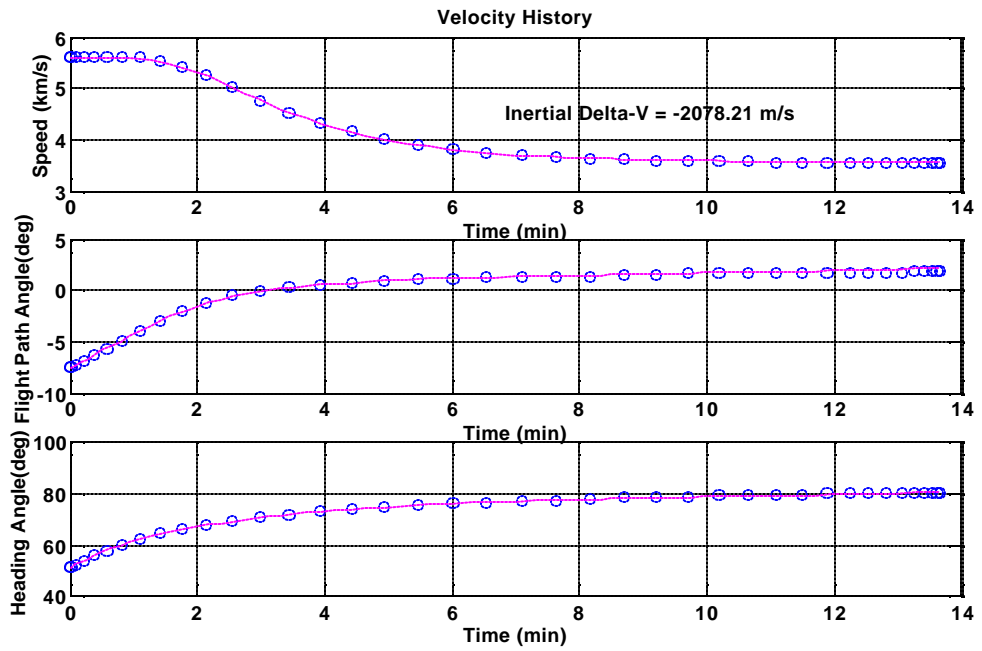
Figure 62: Aerocapture Velocity States (Min Total Fuel)

The bank angle history is given in Figure 63. Unfortunately, current versions of DIDO do not return the covectors for problems with internal knots such as this one making verification difficult. For this reason, the CMT controls can not be shown for comparison. Similarly the Hamiltonian is not available for verification of the first integral.
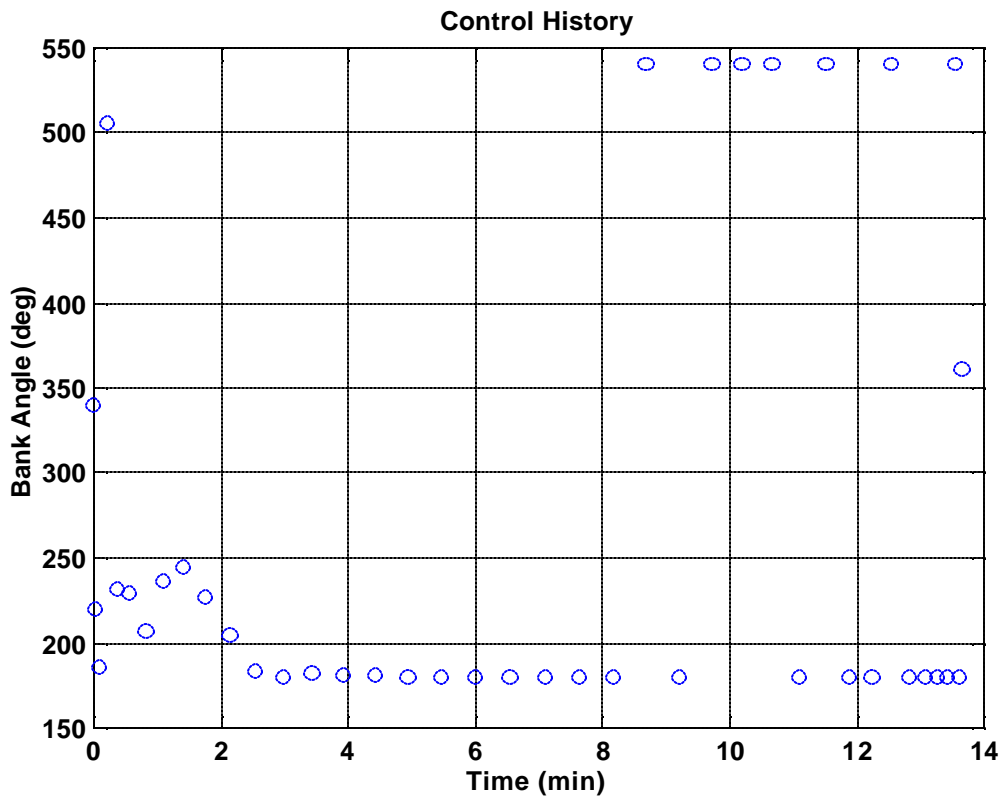
Control History

Figure 63: Aerocapture Control History (Min Total Fuel)

Figure 64 gives the heating rate over the trajectory. The peak heating rate of 12.2 W/cm^2 occurs 2.14 minutes into the trajectory and the total heat load is 3054.3 J/cm^2. Using 50 kg of TPS mass per 10,000 J/cm^2 of heat load, this corresponds to approximately 15.3 kg of front-shield mass.
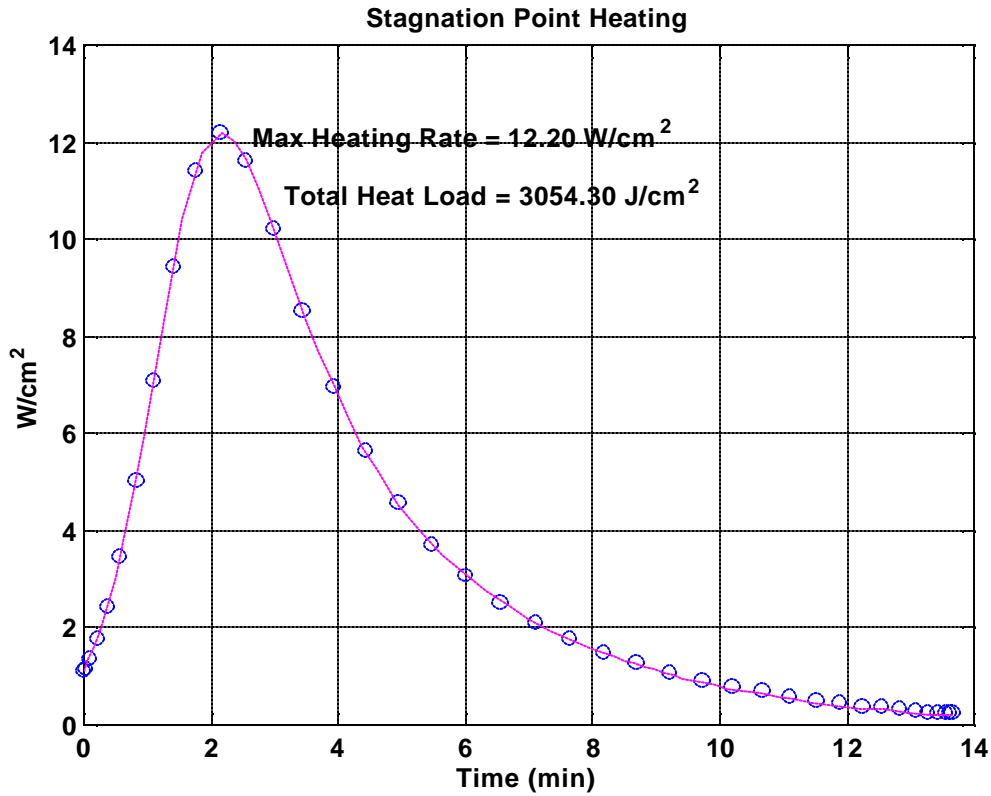
Figure 64: Aerocapture Heating Rate (Min Total Fuel)

Unfortunately, DIDO does not currently return covectors for problems with interior knots such as this mixed-dynamics problem. Without the covectors or Hamiltonian, verification of the optimality of the solution is more difficult. In principle, the interior event conditions of the mixed-dynamic problem could be used to formulate two optimization problems, essentially breaking the problem back into its parts. Each optimal control problem could then be solved, and the covectors and Hamiltonians exploited to determine optimality. The optimality of the combined problem could then be declared if each individual problem was optimal on its own and each solution state and control history matched that of the combined solution. This verification was not performed in this work due to lack of time.

B.   MAXIMUM SCIENTIFIC MASS

The maximum scientific mass cost function added further difficulties in obtaining a solution. Simply changing the cost function yielded infeasible solutions. Unlike the minimum total fuel case, increasing the vehicle thrust did not resolve this issue. To obtain a solution, a hypothetical target planet with the properties of Mars was placed at 5.2 AU. Like the minimum total fuel case, the problem was solved for a non-rotating target atmosphere. Even with these changes, solutions for high numbers of nodes became numerically unstable and yielded infeasible solutions. The solution presented below was obtained using 120 nodes for the low thrust segment and 50 nodes for the aerocapture segment. The state histories for this solution are given in Figure 65. The vehicle begins with a zero C_3 and initial mass of 660 kg and arrives at Mars with 487 kg consuming 173 kg of propellant. The total trip time is 1187.4 days. The DIDO low thrust state histories are in excellent agreement with the propagated states.
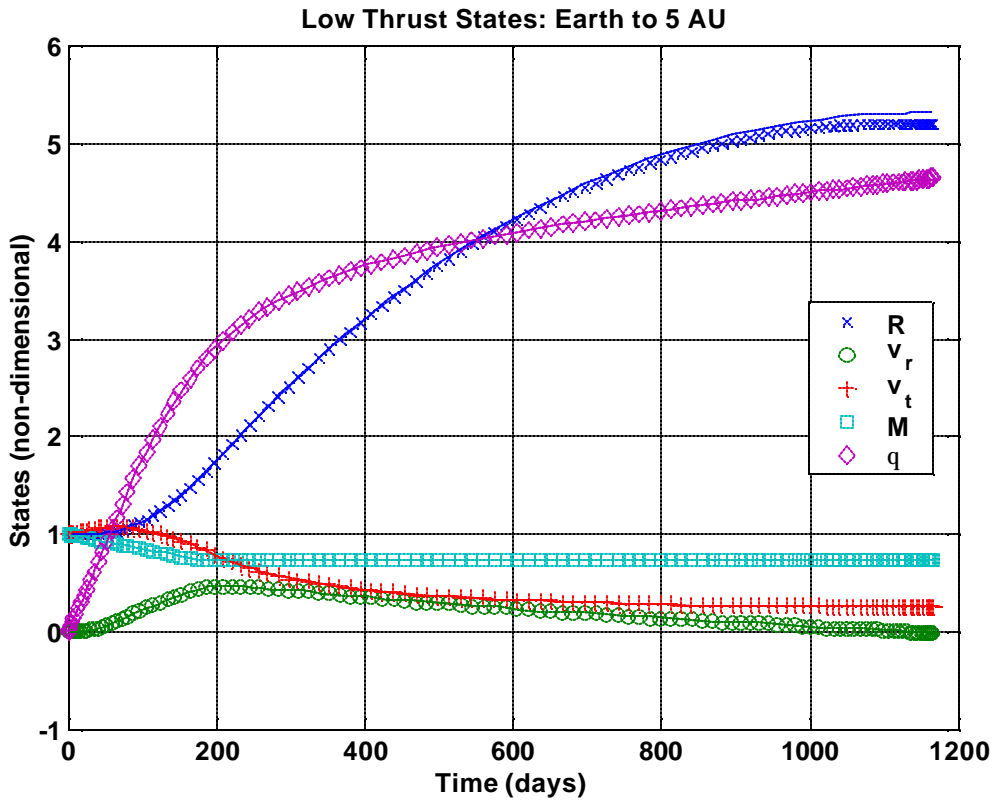
Figure 65: Low Thrust State Histories (Maximum Scientific Mass)

Figure 66 shows the heliocentric trajectory for the low thrust portion. Again, the vehicle conducts a long continuous burn for 175 days before shutting off and coasting with just enough energy to reach 5.2 AU.
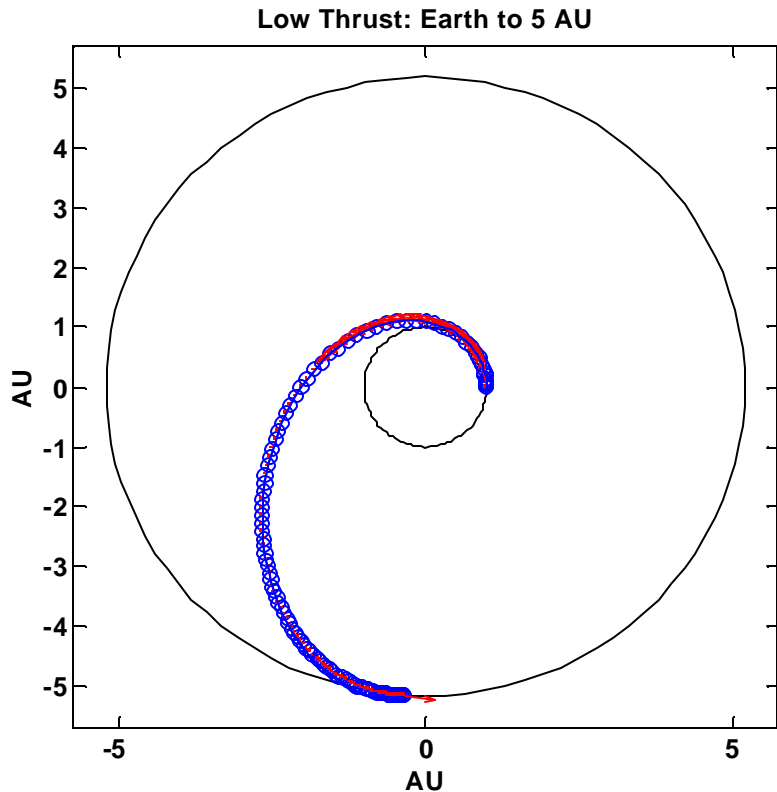
Figure 66: Heliocentric Low Thrust Transfer Orbit (Max Scientific Mass)

Figure 67 shows the control histories for the low thrust segment of the mission. The lower plot shows the normalized thrust history with distinct thrust switch at approximately 175 days. The thrust angle is approximately zero during the thrusting portion of the trajectory. The remainder of the thrust angle history may be disregarded as it is of course meaningless when thrust magnitude is zero.
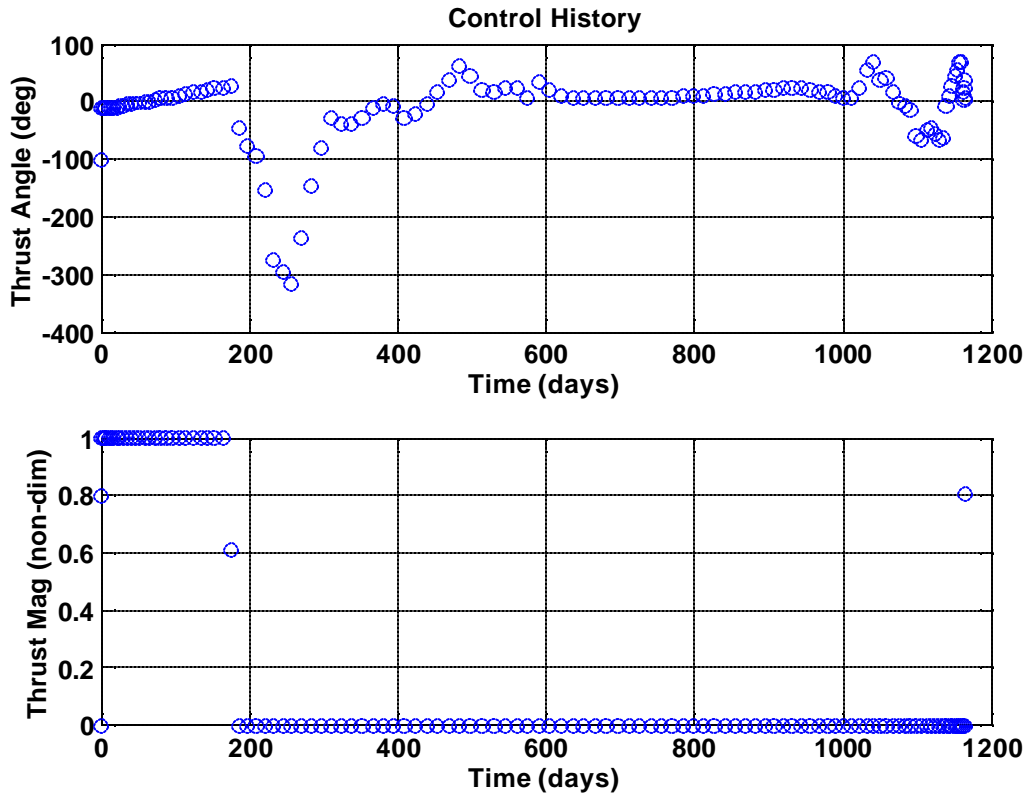
Figure 67: Low Thrust Control Histories (Max Scientific Mass)

The aerocapture state histories are show in Figure 68 and Figure 69. The trajectory begins with an inertial V-infinity at arrival of 5211 m/s and a flight path angle of arrival of -10.1 degrees. The fact that the initial V-infinity is not zero demonstrates that the global solution is minimizing low thrust propellant at the expense of more efficient thermal energy dissipation during the aerocapture segment. The initial heading of -95.6 degrees is due to the non-rotating atmosphere which causes the cost function to be invariant with latitude and heading angle. The inertial delta-V for the pass is 3668 m/s and terminates in an orbit with an eccentricity of 0.04.   Capture occurs at 1.87 minutes. Unlike the low thrust trajectories, the DIDO solutions do not correspond as well with the propagated states, particularly with the radius state. It is likely that increasing the number of nodes for this segment would lead to better convergence between the DIDO and propagated solutions.

125
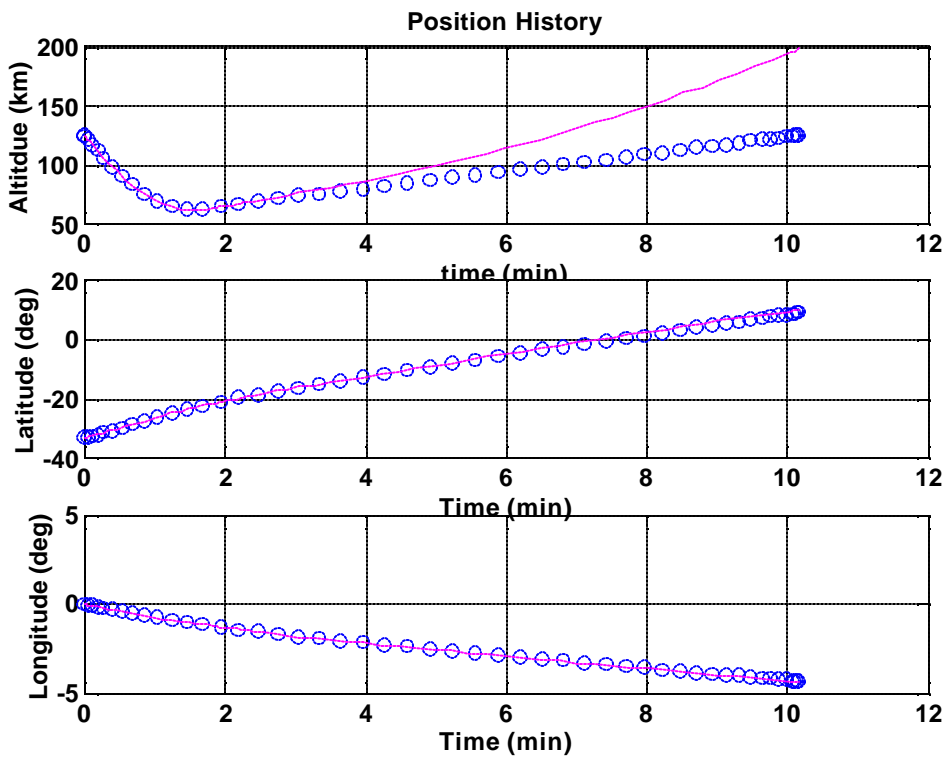
Figure 68: Aerocapture Position States (Max Scientific Mass)
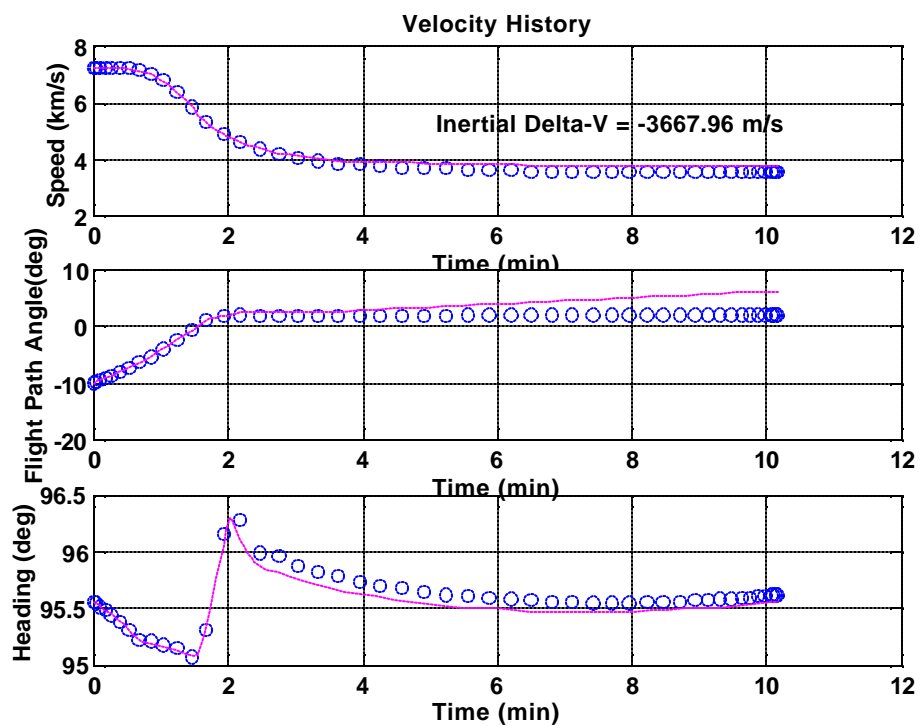
Figure 69: Aerocapture Velocity States (Max Scientific Mass)

The bank angle control history is shown in Figure 70 below. As in the pure aerocapture optimizations investigated earlier, the bank angle begins approximately lift up before switching at approximately 1.9 minutes to lift down. Again, the chatter in the early history of the control is due to the lack of aerodynamic control authority high in the atmosphere and would be expected to be smoothed with higher-node solutions.
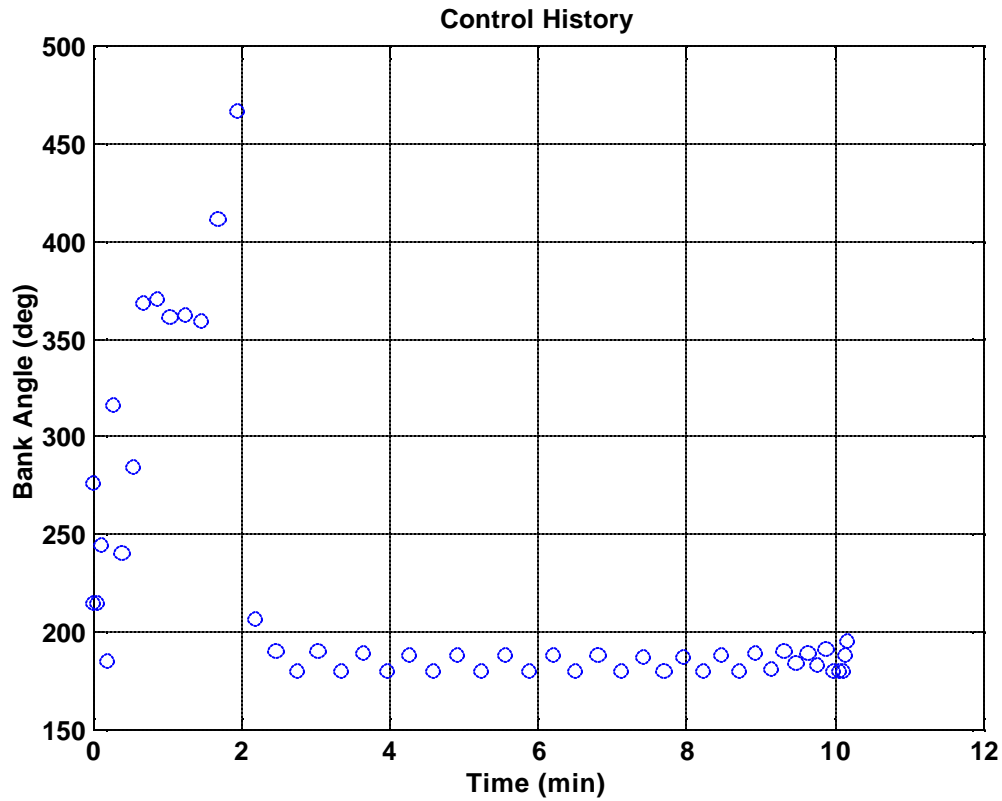
Figure 70: Bank Angle History (Max Scientific Mass)

Figure 71 shows the heating rate history during the atmospheric pass. The maximum stagnation point heating of 34.2 W/cm^2 occurs at 1.24 minutes and the total heat load is 3586.59 J/cm^2. Using the TPS mass model discussed previously, this corresponds to a front-shield mass of 17.93 kg. Combined with the 9.83 kg of propellant required to circularize the orbit, the total aerocapture mass is 27.7 kg. This compares with 331 kg that would be required for a pure propulsive capture at the target planet.
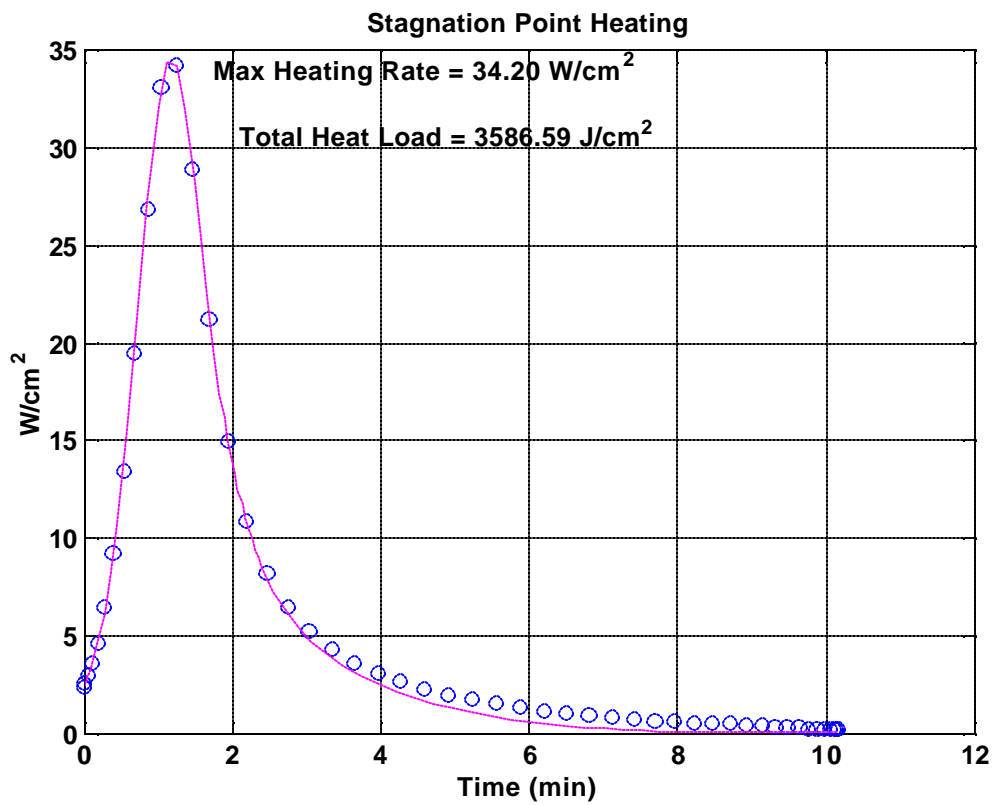
Figure 71: Aerocapture Heating Rate (Max Scientific Mass)

XI. CONCLUSIONS

The suitability of the direct pseudospectral method for solving highly non-linear astrodynamic problems has been explored. For low thrust problems, the method has been shown to produce excellent results, particularly for minimum time problems. However unknown factors cause low thrust minimum fuel solutions to be more difficult to consistently obtain. The method was particularly successful in solving optimal aerocapture trajectories over a range of conditions.

The suitability of the direct method for simultaneously solving a combined low thrust trajectory with terminal aerocapture was also explored. Although the fidelity of the models was reduced to obtain feasible solutions, the proof-of-concept is considered a success as it successfully found feasible solutions for the combined trajectories. This concept of simultaneously optimizing trajectory segments with vastly different dynamics has the potential to identify previously unexplored trajectory combinations and further research in this area is strongly suggested.

THIS PAGE INTENTIONALLY LEFT BLANK

XII. FUTURE WORK

Due to the proof-of-concept nature of this work, there are numerous areas for which future work is encouraged. For low thrust problems, launch vehicle optimization can be added allowing for design trades between initial mass and initial C_3. More realistic trajectories may be obtained by exploring 3-DOF as well as non-circular target orbits. Additionally, adding the gravitational effects of additional bodies may allow for the exploitation of gravity assists and further mass savings. Finally, the difficulties with obtaining certain low thrust minimum fuel trajectories should be further investigated.

For aerocapture, a more accurate TPS mass model should be developed such that both the heat load and the peak heating rate are taken into account. Furthermore, the benefits of angle of attack modulation during aerocapture as well as thrusting arcs may yield new families of trajectories and should be explored. Additionally, other cost functions such as minimum altitude may be useful for such missions as sample return.

Finally, this initial work solving mixed dynamic optimization problems may be expanded in many areas. To obtain any solutions at all, the fidelity was considerably reduced. Hopefully many of the problems with the combined trajectories will be rectified when the difficulties with the minimum fuel trajectories discussed above are resolved. Lastly, with future versions of DIDO, users should be able to recover the covectors for problems with interior knots, allowing for the verification of the DIDO trajectories.

THIS PAGE INTENTIONALLY LEFT BLANK

APPENDIX A: USEFUL TRANSFORMATIONS

A. COORDINATE TRANSFORMATIONS

The following transformations are useful for moving between various aerocapture frames.

1. Spherical to Inertial

First rotate about $\hat{K}$ by $\boldsymbol{q}$, then $\hat{Y}'$ by $-\boldsymbol{f}$.

$$\begin{bmatrix} \hat{e}_r \\ \hat{e}_q \\ \hat{e}_f \end{bmatrix} = \begin{bmatrix} \cos\boldsymbol{f} & 0 & -\sin\boldsymbol{f} \\ 0 & 1 & 0 \\ \sin\boldsymbol{f} & 0 & \cos\boldsymbol{f} \end{bmatrix} \begin{bmatrix} \cos\boldsymbol{q} & \sin\boldsymbol{q} & 0 \\ -\sin\boldsymbol{q} & \cos\boldsymbol{q} & 0 \\ 0 & 0 & 1 \end{bmatrix} \begin{bmatrix} \hat{I} \\ \hat{J} \\ \hat{K} \end{bmatrix} \tag{213}$$

which simplifies to

$$\begin{bmatrix} \hat{e}_r \\ \hat{e}_q \\ \hat{e}_f \end{bmatrix} = \begin{bmatrix} \cos\boldsymbol{q}\cos\boldsymbol{f} & \sin\boldsymbol{q}\cos\boldsymbol{f} & \sin\boldsymbol{f} \\ -\sin\boldsymbol{q} & \cos\boldsymbol{q} & 0 \\ -\cos\boldsymbol{q}\sin\boldsymbol{f} & -\sin\boldsymbol{q}\sin\boldsymbol{f} & \cos\boldsymbol{f} \end{bmatrix} \begin{bmatrix} \hat{I} \\ \hat{J} \\ \hat{K} \end{bmatrix} \tag{214}$$

2. REN Frame to Frenet Frame

First rotate about $\hat{r}$ by $\boldsymbol{y}$, then rotate about $\hat{f}'$ by $-\boldsymbol{g}$.

$$\begin{bmatrix} \hat{e}_n \\ \hat{e}_s \\ \hat{e}_w \end{bmatrix} = \begin{bmatrix} \cos\boldsymbol{g} & -\sin\boldsymbol{g} & 0 \\ \sin\boldsymbol{g} & \cos\boldsymbol{g} & 0 \\ 0 & 0 & 1 \end{bmatrix} \begin{bmatrix} 1 & 0 & 0 \\ 0 & \cos\boldsymbol{y} & \sin\boldsymbol{y} \\ 0 & -\sin\boldsymbol{y} & \cos\boldsymbol{y} \end{bmatrix} \begin{bmatrix} \hat{e}_r \\ \hat{e}_q \\ \hat{e}_f \end{bmatrix} \tag{215}$$

which simplifies to

$$\begin{bmatrix} \hat{e}_n \\ \hat{e}_s \\ \hat{e}_w \end{bmatrix} = \begin{bmatrix} \cos\boldsymbol{g} & -\sin\boldsymbol{g}\cos\boldsymbol{y} & -\sin\boldsymbol{g}\sin\boldsymbol{y} \\ \sin\boldsymbol{g} & \cos\boldsymbol{g}\cos\boldsymbol{y} & \cos\boldsymbol{g}\sin\boldsymbol{y} \\ 0 & -\sin\boldsymbol{y} & \cos\boldsymbol{y} \end{bmatrix} \begin{bmatrix} \hat{e}_r \\ \hat{e}_q \\ \hat{e}_f \end{bmatrix} \tag{216}$$

which can be inverted to

$$\begin{bmatrix} \hat{e}_r \\ \hat{e}_q \\ \hat{e}_f \end{bmatrix} = \begin{bmatrix} \cos\boldsymbol{g} & \sin\boldsymbol{g} & 0 \\ -\sin\boldsymbol{g}\cos\boldsymbol{y} & \cos\boldsymbol{g}\cos\boldsymbol{y} & -\sin\boldsymbol{y} \\ -\sin\boldsymbol{g}\sin\boldsymbol{y} & \cos\boldsymbol{g}\sin\boldsymbol{y} & \cos\boldsymbol{y} \end{bmatrix} \begin{bmatrix} \hat{e}_n \\ \hat{e}_s \\ \hat{e}_w \end{bmatrix} \tag{217}$$

which can be inverted to

$$\begin{bmatrix} \hat{I} \\ \hat{J} \\ \hat{K} \end{bmatrix} = \begin{bmatrix} \cos q \cos f & -\sin q & -\cos q \sin f \\ \sin q \cos f & \cos q & -\sin q \sin f \\ \sin f & 0 & \cos f \end{bmatrix} \begin{bmatrix} \hat{e}_r \\ \hat{e}_q \\ \hat{e}_f \end{bmatrix} \tag{218}$$

3.   PCF to PCI Velocity

Recall that $\mathbf{V}_{PCI}$ is the inertial velocity vector and $\mathbf{V}_{PCF}$ is the velocity vector in the rotating frame. The transport theorem states

$$\mathbf{V}_{PCI} = \mathbf{V}_{PCF} + {}^{PCI}?^{PCF} \times \mathbf{r} \tag{219}$$

But the angular rate of the rotating frame is given by

$${}^{PCI}?^{PCF} = \Omega \hat{K} = \sin f \, \hat{e}_r + \cos f \, \hat{e}_f \tag{220}$$

The positions vector in spherical coordinates is simply

$$\{\mathbf{r}\}_{rqf} = r \, \hat{e}_r \tag{221}$$

The can be transformed from REN to spherical by

$$\{\mathbf{V}_{PCF}\}_{rqf} = \begin{bmatrix} \cos g & \sin g & 0 \\ -\sin g \cos y & \cos g \cos y & -\sin y \\ -\sin g \sin y & \cos g \sin y & \cos y \end{bmatrix} \begin{bmatrix} 0 \\ v \\ 0 \end{bmatrix} \tag{222}$$

which gives

$$\{\mathbf{V}_{PCF}\}_{rqf} = v \sin g \, \hat{e}_r + v \cos g \cos y \, \hat{e}_q + v \cos g \sin y \, \hat{e}_f \tag{223}$$

so substituting into Eqn. (219) results in

$$\{\mathbf{V}_{PCI}\}_{rqf} = \begin{bmatrix} v \sin g \\ v \cos g \cos y \\ v \cos g \sin y \end{bmatrix} + \begin{vmatrix} \hat{e}_r & \hat{e}_q & \hat{e}_f \\ \Omega \sin f & 0 & \Omega \cos f \\ r & 0 & 0 \end{vmatrix} \tag{224}$$

which simplifies to

$$\{\mathbf{V}_{PCI}\}_{rqf} = v \sin g \, \hat{e}_r + (v \cos g \cos y + r\Omega \cos f)\hat{e}_q + v \cos g \sin y \, \hat{e}_f \tag{225}$$

134

This gives the spherical inertial velocity components V_r, V_q, and V_f in terms of the velocity vector in the rotating REN frame.

$$\{V_r\}_{PCI} = v\sin\boldsymbol{g}$$
$$\{V_q\}_{PCI} = v\cos\boldsymbol{g}\cos\boldsymbol{y} + r\Omega\cos\boldsymbol{f} \qquad (226)$$
$$\{V_f\}_{PCI} = v\cos\boldsymbol{g}\sin\boldsymbol{y}$$

We can now obtain the velocity components in the inertial REN frame by squaring both sides of Eqn. (225) to get

$$\|V_{PCI}\|^2 = v^2 + r^2\Omega^2\cos^2\boldsymbol{f} + 2rv\Omega\cos\boldsymbol{f}\cos\boldsymbol{y}\,cos\boldsymbol{g} \qquad (227)$$

so the inertial speed in the REN frame is

$$V_{PCI} = \sqrt{v^2 + r^2\Omega^2\cos^2\boldsymbol{f} + 2\,rv\Omega\cos\boldsymbol{f}\cos\boldsymbol{y}\,cos\boldsymbol{g}} \qquad (228)$$

Recalling Figure 3

$$\Psi \equiv \mathrm{atan}\left(\frac{V_f}{V_q}\right) \qquad (229)$$

and

$$\Gamma \equiv \mathrm{atan}\left(\frac{V_r}{\sqrt{V_q^2 + V_f^2}}\right) \qquad (230)$$

Substituting Eqns. (226) into (229) and (230) we get

$$\Psi = \mathrm{atan}\left(\frac{v\cos\boldsymbol{g}\sin\boldsymbol{y}}{v\cos\boldsymbol{g}\cos\boldsymbol{y} + r\Omega\cos\boldsymbol{f}}\right) \qquad (231)$$

and

$$\Gamma = \mathrm{atan}\left(\frac{v\sin\boldsymbol{g}}{\sqrt{\cos^2\boldsymbol{g}\left(v^2 + \Omega^2 r^2\right) + 2vr\Omega\cos\boldsymbol{g}\cos\boldsymbol{y}\cos\boldsymbol{f}}}\right) \qquad (232)$$

135

Thus Eqns (228), (231), and (232) give us the <u>inertial</u> velocity components resolved in the REN frame as functions of the position and velocity components as measured in the <u>rotating</u> REN frame.

APPENDIX B: MINIMUM AEROCAPTURE MASS AT MARS
FROM ZERO ARRIVAL V-INFINITY DATA

```
Data Summary:


Inertial Velocity Components:


Arrival V infinity (m/s):        0.00


Atmospheric Entry:

Speed (m/s):                     4949.30

Heading (deg):                   -0.09

Flight Path Angle (deg):         -7.44


Atmospheric Exit:

Speed (m/s):                     3523.53

Heading (deg):                   0.08

Flight Path Angle (deg):         1.87

Delta-V (m/s):                   1425.77


Rotating Velocity Components:

Atmospheric Entry:

Speed (m/s):                     4702.36

Heading (deg):                   -0.09

Flight Path Angle (deg):         -7.83


Atmospheric Exit:

Speed (m/s):                     3274.53

Heading (deg):                   0.09

Flight Path Angle (deg):         2.02

Delta-V (m/s):                   1427.83


Trajectory Analysis:
```

```
Total Pass Time:              734.40 sec (12.24 min)

Minimum Altitude (km):        70.14

Time to Min Alt:              158.94 sec (2.65 min)

Max Dynamic Pressure (Pa):    505.71

Time of Max Dynamic Pressure: 158.94 sec (2.65 min)

Max Acceleration: (g)         0.85

Time of Max Acceleration:     158.94 sec (2.65 min)

Max Heating Rate: (W/cm^2)    7.44

Time of Max Heating Rate:     140.18 sec (2.34 min)

Heat Load: (J/cm^2)           1700.38


Final Orbit Parameters:

Semi-major Axis (km):         3563.65

Periapsis (km):               3437.39

Apoapsis (km):                3689.92

Apoapsis Altitude (km):       300.00

Eccentricity:                 0.04


Capture Time:                 0.00 sec (0.00 min)


Total Aerocapture Mass (kg):                             19.14

Propellant Mass to Circularize After Aerocapture (kg):  10.63

Estimated Front-shield mass (kg):                       8.50


Pure Propulsive insertion:

Isp = 330.000000

Propellant Mass (kg): 201.442991
```

APPENDIX C: MINIMUM AEROCAPTURE MASS AT MARS FROM EXCESS ARRIVAL V-INFINITY DATA

Data Summary:

Inertial Velocity Components:

Arrival V infinity (m/s):   5200.00

Atmospheric Entry:

Speed (m/s):   7178.83

Heading (deg):   -0.15

Flight Path Angle (deg):   -10.47

Atmospheric Exit:

Speed (m/s):   3517.05

Heading (deg):   0.27

Flight Path Angle (deg):   2.18

Delta-V (m/s):   3661.78

Rotating Velocity Components:

Atmospheric Entry:

Speed (m/s):   6933.98

Heading (deg):   -0.15

Flight Path Angle (deg):   -10.85

Atmospheric Exit:

Speed (m/s):   3268.11

Heading (deg):   0.29

Flight Path Angle (deg):   2.35

Delta-V (m/s):   3665.88

Trajectory Analysis:

```
Total Pass Time:              601.02 sec (10.02 min)

Minimum Altitude (km):        58.51

Time to Min Alt:              94.63 sec (1.58 min)

Max Dynamic Pressure (Pa):    2703.70

Time of Max Dynamic Pressure: 79.78 sec (1.33 min)

Max Acceleration: (g)         4.57

Time of Max Acceleration:     79.78 sec (1.33 min)

Max Heating Rate: (W/cm^2)    35.02

Time of Max Heating Rate:     72.76 sec (1.21 min)

Heat Load: (J/cm^2)           3388.37


Final Orbit Parameters:

Semi-major Axis (km):         3550.25

Periapsis (km):               3410.57

Apoapsis (km):                3689.92

Apoapsis Altitude (km):       300.00

Eccentricity:                 0.04


Capture Time:                 110.50 sec (1.84 min)


Total Aerocapture Mass (kg):                          28.75

Propellant Mass to Circularize After Aerocapture (kg): 11.81

Estimated Front-shield mass (kg):                     16.94


Pure Propulsive insertion:

Isp = 330.000000

Propellant Mass (kg): 386.401888
```

APPENDIX D: MINIMUM AEROCAPTURE MASS AT MARS FROM EXCESS ARRIVAL V-INFINITY DATA

```
Data Summary:


Inertial Velocity Components:


Arrival V infinity (m/s):        9419.99


Atmospheric Entry:

Speed (m/s):                     24987.43

Heading (deg):                   -0.08

Flight Path Angle (deg):         -9.35


Atmospheric Exit:

Speed (m/s):                     16143.37

Heading (deg):                   0.54

Flight Path Angle (deg):         1.28

Delta-V (m/s):                   8844.06


Rotating Velocity Components:

Atmospheric Entry:

Speed (m/s):                     22615.43

Heading (deg):                   -0.08

Flight Path Angle (deg):         -10.34


Atmospheric Exit:

Speed (m/s):                     13736.80

Heading (deg):                   0.64

Flight Path Angle (deg):         1.51

Delta-V (m/s):                   8878.62


Trajectory Analysis:
```

```
Total Pass Time:            1358.47 sec (22.64 min)

Minimum Altitude (km):      256.46

Time to Min Alt:            249.75 sec (4.16 min)

Max Dynamic Pressure (Pa):  3451.29

Time of Max Dynamic Pressure:  231.55 sec (3.86 min)

Max Acceleration: (g)       5.83

Time of Max Acceleration:   231.55 sec (3.86 min)

Max Heating Rate: (W/cm^2)  264.59

Time of Max Heating Rate:   213.90 sec (3.56 min)

Heat Load: (J/cm^2)         55903.98


Final Orbit Parameters:

Semi-major Axis (km):       24757.55

Periapsis (km):             23891.11

Apoapsis (km):              25624.00

Apoapsis Altitude (km):     1000.00

Eccentricity:               0.03


Capture Time:               213.90 sec (3.56 min)


Total Aerocapture Mass (kg):                        327.98

Propellant Mass to Circularize After Aerocapture (kg):  48.40

Estimated Front-shield mass (kg):                   279.52


Pure Propulsive insertion:

Isp = 330.000000

Propellant Mass (kg): 528.735021
```

APPENDIX D: MINIMUM AEROCAPTURE MASS AT MARS WITH G-LIMITS

```
Data Summary:


Inertial Velocity Components:


Arrival V infinity (m/s):       5199.99


Atmospheric Entry:

Speed (m/s):                    7178.82

Heading (deg):                  -0.09

Flight Path Angle (deg):        -9.73


Atmospheric Exit:

Speed (m/s):                    3520.80

Heading (deg):                  -0.29

Flight Path Angle (deg):        2.01

Delta-V (m/s):                  3658.02


Rotating Velocity Components:

Atmospheric Entry:

Speed (m/s):                    6933.39

Heading (deg):                  -0.09

Flight Path Angle (deg):        -10.07


Atmospheric Exit:

Speed (m/s):                    3271.83

Heading (deg):                  -0.32

Flight Path Angle (deg):        2.16

Delta-V (m/s):                  3661.56


Trajectory Analysis:

Total Pass Time:                684.58 sec (11.41 min)
```

```
Minimum Altitude (km):          61.98

Time to Min Alt:                122.65 sec (2.04 min)

Max Dynamic Pressure (Pa):      1803.97

Time of Max Dynamic Pressure:   96.30 sec (1.61 min)

Max Acceleration: (g)           3.05

Time of Max Acceleration:       96.30 sec (1.61 min)

Max Heating Rate: (W/cm^2)      30.39

Time of Max Heating Rate:       78.32 sec (1.31 min)

Heat Load: (J/cm^2)             3814.61


Final Orbit Parameters:

Semi-major Axis (km):           3557.99

Periapsis (km):                 3426.09

Apoapsis (km):                  3689.90

Apoapsis Altitude (km):         299.98

Eccentricity:                   0.04


Capture Time:                   136.75 sec (2.28 min)


Total Aerocapture Mass (kg):                            30.20

Propellant Mass to Circularize After Aerocapture (kg): 11.13

Estimated Front-shield mass (kg):                      19.07


Pure Propulsive insertion:

Isp = 330.000000

Propellant Mass (kg): 386.401510
```

144

APPENDIX E: MAXIMUM INITIAL FLIGHT PATH ANGLE FOR AEROCAPTURE AT MARS

Data Summary:

Inertial Velocity Components:

Arrival V infinity (m/s):   5200.00

Atmospheric Entry:

Speed (m/s):   7178.83

Heading (deg):   -73.46

Flight Path Angle (deg):   -8.65

Atmospheric Exit:

Speed (m/s):   3516.46

Heading (deg):   -66.33

Flight Path Angle (deg):   2.21

Delta-V (m/s):   3662.37

Rotating Velocity Components:

Atmospheric Entry:

Speed (m/s):   7115.54

Heading (deg):   -75.32

Flight Path Angle (deg):   -8.73

Atmospheric Exit:

Speed (m/s):   3436.81

Heading (deg):   -69.58

Flight Path Angle (deg):   2.26

Delta-V (m/s):   3678.72

Trajectory Analysis:

Total Pass Time: 708.99 sec (11.82 min)

```
Minimum Altitude (km):          66.52

Time to Min Alt:                149.76 sec (2.50 min)

Max Dynamic Pressure (Pa):      1354.90

Time of Max Dynamic Pressure:   114.93 sec (1.92 min)

Max Acceleration: (g)           2.29

Time of Max Acceleration:       114.93 sec (1.92 min)

Max Heating Rate: (W/cm^2)      27.67

Time of Max Heating Rate:       91.29 sec (1.52 min)

Heat Load: (J/cm^2)             4612.22


Final Orbit Parameters:

Semi-major Axis (km):           3549.02

Periapsis (km):                 3408.13

Apoapsis (km):                  3689.92

Apoapsis Altitude (km):         300.00

Eccentricity:                   0.04


Capture Time:                   178.05 sec (2.97 min)

Final Inclination:              70.00 deg


Total Aerocapture Mass (kg):                            34.97

Propellant Mass to Circularize After Aerocapture (kg): 11.91

Estimated Front-shield mass (kg):                      23.06


Pure Propulsive insertion:

Isp = 330.000000

Propellant Mass (kg): 386.401888
```

APPENDIX F: MINIMUM INITIAL FLIGHT PATH ANGLE FOR AEROCAPTURE AT MARS

```
Data Summary:


Inertial Velocity Components:


Arrival V infinity (m/s):        5200.00


Atmospheric Entry:

Speed (m/s):                     7178.83

Heading (deg):                   -73.40

Flight Path Angle (deg):         -10.83


Atmospheric Exit:

Speed (m/s):                     3435.29

Heading (deg):                   -69.85

Flight Path Angle (deg):         4.60

Delta-V (m/s):                   3743.54


Rotating Velocity Components:

Atmospheric Entry:

Speed (m/s):                     7115.88

Heading (deg):                   -75.27

Flight Path Angle (deg):         -10.93


Atmospheric Exit:

Speed (m/s):                     3358.39

Heading (deg):                   -73.83

Flight Path Angle (deg):         4.71

Delta-V (m/s):                   3757.48


Trajectory Analysis:

Total Pass Time:                 352.25 sec (5.87 min)
```

```
Minimum Altitude (km):          56.32

Time to Min Alt:                93.33 sec (1.56 min)

Max Dynamic Pressure (Pa):      3298.44

Time of Max Dynamic Pressure:   78.99 sec (1.32 min)

Max Acceleration: (g)           5.57

Time of Max Acceleration:       78.99 sec (1.32 min)

Max Heating Rate: (W/cm^2)      39.76

Time of Max Heating Rate:       65.53 sec (1.09 min)

Heat Load: (J/cm^2)             3138.83


Final Orbit Parameters:

Semi-major Axis (km):           3391.27

Periapsis (km):                 3092.61

Apoapsis (km):                  3689.92

Apoapsis Altitude (km):         300.00

Eccentricity:                   0.09


Capture Time:                   98.27 sec (1.64 min)

Final Inclination:              70.00 deg


Total Aerocapture Mass (kg):                            42.1

Propellant Mass to Circularize After Aerocapture (kg):  26.41

Estimated Front-shield mass (kg):                       15.69


Pure Propulsive insertion:

Isp = 330.000000

Propellant Mass (kg): 386.401889
```

LIST OF REFERENCES

1. Bryson, Arthur E., Ho, Yu-Chi, *Applied Optimal Control: Optimization, Estimation, and Control*, Hemisphere Publishing, 1975.

2. Prussing, John E., and Conway, Bruce A., *Orbital Maneuvers*, Oxford University Press, New York, New York, 1993.

3. Sergeyevsky, Andrey B., Snyder, Gerald C., Cunniff, Ross A., *Interplanetary Mission Design Handbook, Volume I, Part 2*, Jet Propulsion Laboratory, Pasadena, California, 1983.

4. Brophy, John R., and others, "Ion Propulsion System (NSTAR) Technology Performance Report"

5. Betts, John T., *Practical Methods for Optimal Control Using Nonlinear Programming*, pp. 35-36, Siam, 2001.

6. Ross, I. Michael, *AA4850 Class Notes*, Monterey, Spring 2001.

7. Vallado, David A., *Fundamental of Astrodynamics and Applications*, Second Edition, Microcosm Press, El Segundo, California, 2001.

8. Ross, I. Michael, 3-DOF Model: Canonical EOMs Notes, Monterey, February 1998.

9. Leszczynski, Z., *Modeling, Simulation and Visualization of Aerocapture*, Master's Thesis, Naval Postgraduate School, Monterey, California, September 1999.

10. Bryson, A. E., Mikami, K., Battle, C. T., "Optimal Lateral Turns for a Re-Entry Glider," *Aerospace Engineering*, Vol.21, No.3, March 1962.

11. Anderson, John D., *Introduction to Flight*, McGraw Hill, Boston, Massachusetts, 2000, pp. 557-558.

12. Conversations and email between Gary Allen (NASA Ames Research Center) and the author, March 2002.

13. Emails between Jeff Hall (JPL) and the author, August-December 2002.

14. Conversations between Prof. I. Michael Ross and the author, May 2002.

15. Wetzel, Todd A., and Moerder, Daniel D., "Vehicle/Trajectory Optimization for Aerocapture at Mars," *Journal of the Astronautical Sciences*, Vol .42, No.1, pp. 71-89, January-March 1994.

16. Wertz, James R., and Larson, Wiley, J., *Space Mission Analysis and Design*, 3rd ed., Microcosm Press, 1999.

17. Hall, Jeffery L., and Le, Andrew K., "Aerocapture Trajectories for Spacecraft with Large, Towed Ballutes," paper presented at the AAS/AIAA Space Flight Mechanics Meeting, Santa Barbara, California, 11-15 February 2001.

18. Ross, I. M. and Fahroo, F., "User's Manual for DIDO 2002: A MATLAB Application Package for Dynamic Optimization," *NPS Technical Report*, AA-02-002, Department of Aeronautics and Astronautics, Naval Postgraduate School, Monterey, California, June 2002.

19. Pontryagin, L. S., Boltyanskii, V. G., Gamkrelidze, R. V., and Mischenko, E. F., *The Mathematical Theory of Optimal Processes*, Wiley-Interscience, New York, New York, 1962.

20. Strizzi, Jon D., *Pseudospectral Methods for Rapid Computation of Optimal Controls,* P.h.D. Dissertation, Naval Postgraduate School, Monterey, California, December 2002.

21. Josselyn, Scott B., and Ross, I. Michael, "A Rapid Verification Method for the Trajectory Optimization of Reentry Vehicles," *Journal of Guidance, Navigation and Control*, to appear.

22. Ross, I. M. and Fahroo, F, "A Pseudospectral Transformation of the Covectors of Optimal Control Systems," *Proceedings of the first IFAC Symposium on Systems Structure and Control*, Prague, The Czech Republic, August 2001.

23. Ross, I. M. and Fahroo, F, "Convergence of Pseudospectral Approximations for Optimal Control Problems," *Proceedings of the 2001 IEEE Conference on Decision and Control*, Orlando, Florida, December 2001.

24. Ro, Theodore U., and Queen, Eric M., "Study of Martian Aerocapture Terminal Point Guidance," *AIAA, Atmospheric Flight Mechanics Conference and Exhibit*, Boston, Massachusetts, August 10-12, 1998.

25. Wercinski, P.F. and others, "Trajectory, aerothermal conditions, and thermal protection system mass for the MARS 2001 aerocapture mission," *AIAA, Aerospace Sciences Meeting and Exhibit,* Reno, Nevada. January 6-9, 1997.

INITIAL DISTRIBUTION LIST

1.   Defense Technical Information Center
      Ft. Belvoir, Virginia

2.   Dudley Knox Library
      Naval Postgraduate School
      Monterey, California

3.   Department Chairman, Code AA
      Department of Aeronautics and Astronautics
      Naval Postgraduate School
      Monterey, California

4.   Department of Aeronautics and Astronautics
      ATTN: Professor I. Michael Ross, Code AA/RO
      Naval Postgraduate School
      Monterey, California

5.   Mr. Steve E. Matousek
      NASA Jet Propulsion Laboratory, CODE 264-426
      Pasadena, California

6.   LT Scott B. Josselyn, USN
      Mission Viejo, California